# Feature Selection and Non-Euclidean Dimensionality Reduction: Application to Electrocardiology

by

Dae Yon Jung

A dissertation submitted in partial fulfillment
of the requirements for the degree of
Doctor of Philosophy
(Electrical Engineering: Systems)
in The University of Michigan
2015

Doctoral Committee:

Professor Alfred O. Hero III, Chair
Assistant Professor Laura K. Balzano
Associate Professor Frank M. Bogun
Assistant Professor Honglak Lee
Associate Professor Clayton D. Scott

For the Lord and my family,

who give me eternal support.

# ACKNOWLEDGEMENTS

Studying and researching at the university in this city of Ann Arbor have been the greatest opportunity in my life. This work would not have been possible by myself. Through this acknowledgement, I hope to express my appreciation to the support of my advisor, committee members, parents, colleagues, and friends.

I would like to thank my advisor, Professor Alfred Hero, who has given me the right guidance throughout my doctoral program. I have a sincere appreciation to his patience for waiting my work with faith. I have truly enjoyed working with and getting advice from this brilliant scholar, and everything I have learned from him will be with me forever.

I also thank my committee members, Dr. Frank Bogun, Professor Honglak Lee, Professor Clayton Scott, and Professor Laura Balzano, for their invaluable input and suggestions in this thesis. In particular, I am grateful to Dr. Frank Bogun for his guide and suggestions over the three year period of collaboration. Every knowledge of cardiology is provided from and verified by him. I would also like to thank Professor Honglak Lee. Collaborating with Professor Lee in the early stage of my doctorate was a great, helpful experience.

I would like to show my gratitude to Shelly Feldkamp, Becky Turanksi, Rachel Antoun, Steven Pejuan, Beth Lawson, and Karen Liska for all of their help regarding the administrative matters.

As a member of Hero Group, it was fortunate to have many fellow labmates. I have more appreciation toward the members who have graduated already and left

Ann Arbor. Their presence have helped me become a member of the group and the department.

My life in Ann Arbor was not only about pursuing a doctorate, but also about being a part of the communities. I have enormous thanks to all the members of Korean Student Association-Graduate (KSAG), Korean EECS (KEECS), and Korean Presbyterian Church of Ann Arbor (KPCAA). They always have encouraged and supported me to maintain my life.

I have found it never enough to express my thankful mind to my father, my mother, and my sister, for their never-ending love. I want to tell them from the bottom of my heart that without you, this dissertation would never have been possible.

Finally, I thank the Lord for providing me a purpose in life. Meeting, knowing, and believing God have been one of the greatest experiences that I had in Ann Arbor.

# TABLE OF CONTENTS

# LIST OF FIGURES

**Figure**

# LIST OF TABLES

**Table**

# ABSTRACT

Feature Selection and Non-Euclidean Dimensionality Reduction: Application to Electrocardiology

by

Dae Yon Jung

Chair: Alfred O. Hero III

Heart disease has been the leading cause of human death for decades. To improve treatment of heart disease, algorithms to perform reliable computer diagnosis using electrocardiogram (ECG) data have become an area of active research. This thesis utilizes well-established methods from cluster analysis, classification, and localization to cluster and classify ECG data, and aims to help clinicians diagnose and treat heart diseases. The power of these methods is enhanced by state-of-the-art feature selection and dimensionality reduction. The specific contributions of this thesis are as follows. First, a unique combination of ECG feature selection and mixture model clustering is introduced to classify the sites of origin of ventricular tachycardias. Second, we apply a restricted Boltzmann machine (RBM) to learn sparse representations of ECG signals and to build an enriched classifier from patient data. Third, a novel manifold learning algorithm is introduced, called Quaternion Laplacian Information Maps (QLIM), and is applied to visualize high-dimensional ECG signals. These methods are applied to design of an automated supervised classification algorithm to help a physician identify the origin of ventricular arrhythmias (VA) directed from a patient's ECG data. The

algorithm is trained on a large database of ECGs and catheter positions collected during the electrophysiology (EP) pace-mapping procedures. The proposed algorithm is demonstrated to have a correct classification rate of over 80% for the difficult task of classifying VAs having epicardial or endocardial origins.

# CHAPTER I

# Introduction

## 1.1 Motivation

Heart disease is a leading cause of human death [1, 2]. The high mortality rate of heart disease is predicted to continue at least until 2020 throughout the world [3]. This high mortality has generated significant demands for improving diagnosis, prediction, and treatment of heart disease. The electrocardiogram (ECG) is widely used to identify pathological conditions, and there is a hope that ECG analysis will be able to help diagnose the presence of heart disease [4, 5] and predict future events including myocardial infraction [6] and arrhythmias [7, 8, 9]. The ECG provides a recording of a heart's electrical activity, but is usually not sufficient, when used alone, to diagnose heart disease. For accurate diagnoses, pace-map data is collected during a heart catheterization procedure in the electrophysiology (EP) lab. In this invasive procedure, pace-map data is collected by the clinician in order to associate abnormal ECGs with specific locations on the heart wall using the catheter to stimulate and/or ablate locations on the myocardium.

This thesis is motivated by the prospect that the ECGs during ventricular arrhythmias alone contains sufficient information to localize, at least coarsely, the origin of ventricular arrhythmias without pace-map data. This could lead to improve diagnostic accuracies, reduce medical costs, and facilitate and shorten pace-mapping

procedures. For example, the origin of ventricular tachycardia (VT), a fast-beating arrhythmia that can potentially develop into life-threatening ventricular fibrillation, can be identified by analyzing ECG data collected from multiple pace-map locations. Identifying the precise locations or regions in the heart from which the VT arises helps clinicians to treat patients with appropriate heart surgeries, defibrillator implantation and radiofrequency ablation, and medications. Despite its obvious benefits to clinicians and patients alike, pace-map ECG analyses are challenging because they use complete signals of 12-lead ECGs from multiple patients. This use of ECG data is different from the well-established analyses for rhythm recognition or arrhythmia prediction, where the analyses can be performed on ambulatory ECGs, which consist of fewer leads, from fewer numbers of patients [6, 7, 8, 9].

The objective of this thesis is to design automated algorithms for localizing the origin of arrhythmias based on the ECG. To this aim we introduce novel approaches that are based on machine learning methods of cluster analysis, classification, and localization. There are several challenges that this thesis addresses.

1. High variance data: ECG signals from different patients have various ranges of peak amplitudes, signal durations, and morphology changes that can depend on the patient's gender, heart size, heart disease history, etc.

2. High dimensional data: ECG signals are collected over time from 12 leads based on 10 electrodes attached to a patient's body, and the hundreds of time samples in each signal leads to very high dimensional data.

3. Large range of ECG features: Many different types of features have been proposed for ECG analysis, including onset, amplitude, slope, template matching, and wavelet coefficients. The performance of an automated classification algorithm is highly dependent on the choice of ECG features.

These problems can lead to bias and overfitting during the training phase of machine

learning methods.

In order to overcome the problems while identifying VT origins using ECG data, a new ECG feature, which fulfills the intended purpose, is required. In this thesis, the improvement of ECG analysis is achieved by dimensionality reduction of the original ECG data and selection and extraction of the most relevant ECG features. This permits the classification and localization of VT origins to be accurately and reliably performed with reduced overfitting error or bias.

## 1.2 Background and Contributions

### 1.2.1 Electrocardiogram

The ECG is a recording of the cardiac electrical activity. The first ECG apparatus is invented by Willem Einthoven in 1903 for which he won the Nobel Prize in 1924 [10].

The ECG is measured from ten electrodes placed on the outside of the body, four from the limbs and six from the chest. A complete ECG has 12 different leads, which are signals of varying electrical potentials. The leads are named as follows: I, II, III, aVL, aVR, aVF, V1, V2, V3, V4, V5, and V6. Leads I, II, and III measure the differences in potentials among the two arms and the left leg. Leads aVL, aVR, and aVF are called augmented leads and are derived from leads I, II, and III versus the Wilson central terminal electrode, which is an average of the potentials from the two arms and the left leg. Together the leads I, II, II, aVL, aVR, and aVF constitute the limb leads and can be used to determine frontal electrical axis of the heart. Leads V1 through V6 are the precordial leads. They are located over the patient's chest: V1 and V2 are located in the fourth intercostal space on both sides of the sternum, and V3 through V6 are located in the fifth intercostal space along the left lateral chest. The six precordial electrodes record the electrical activity between the electrodes placed on the chest and the Wilson center terminal electrode.

A single beat of an ECG signal is composed of "waves" that are produced at different phases of depolarization and repolarization in the heart muscle [11]. It starts with a P-wave (atrial depolarization) and moves on to QRS-wave (ventricular depolarization), which is referred to as the "QRS complex." QRS complex is followed by the T-wave that corresponds to the repolarization phase. A U-wave can be present in some patients at the end. A standard ECG signal can be represented as in Figure 1.1a. A real-time ECG would not necessarily have all six wave components, and each wave would not necessarily have the same shape shown in Figure 1.1b. These wave variations are associated with different heart characteristics and conditions. The variations, moreover, enable electrophysiologists and signal analysts to use the ECG for diagnosis, prediction, and treatment of heart disease.

### 1.2.2 Ventricular Tachycardia and Pace-mapping

#### 1.2.2.1 Ventricular Tachycardia

Tachycardia is an arrhythmia with a heart rate over 100 beats per minute, and ventricular tachycardia (VT) is a tachycardia originating from a ventricle. Ventricular tachycardia can result in a low blood pressure that ultimately can cause a faint or syncope of the individual. Ventricular tachycardia can degenerate into ventricular fibrillation (V-fib) resulting in cardiac arrest and death unless ventricular fibrillation is promptly terminated [12].

VT most often occurs in patients with structural heart disease; i.e. they had a prior myocardial infarction or have non-ischemic cardiomyopathy. Both conditions have scar as the common denominator that constitutes the pathological substrate for VT. However, people without structural heart diseases in the absence of scar can also have arrhythmias. The most common arrhythmia in humans are premature ventricular complexes (PVC). They consist of a single ectopic ventricular beat, and most often PVCs occur in the absence of structural heart disease. Some patients can

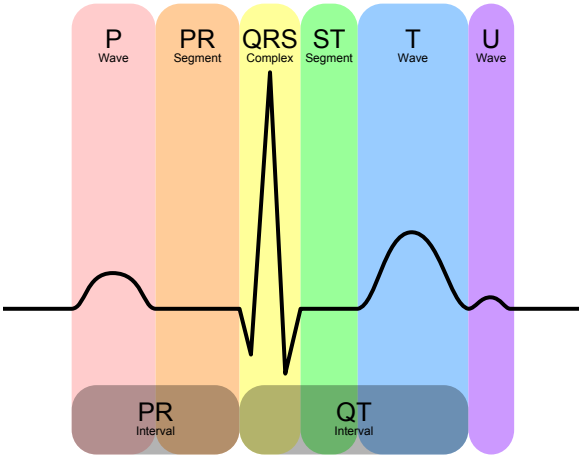


(a) A Schematic Representation of a Normal ECG Signal. Reprinted from Electrocardiography, In *Wikipedia,n.d.*, Retrieved April 14, 2015, from http://en.wikipedia.org/wiki/Electrocardiography. Reprinted with permission.

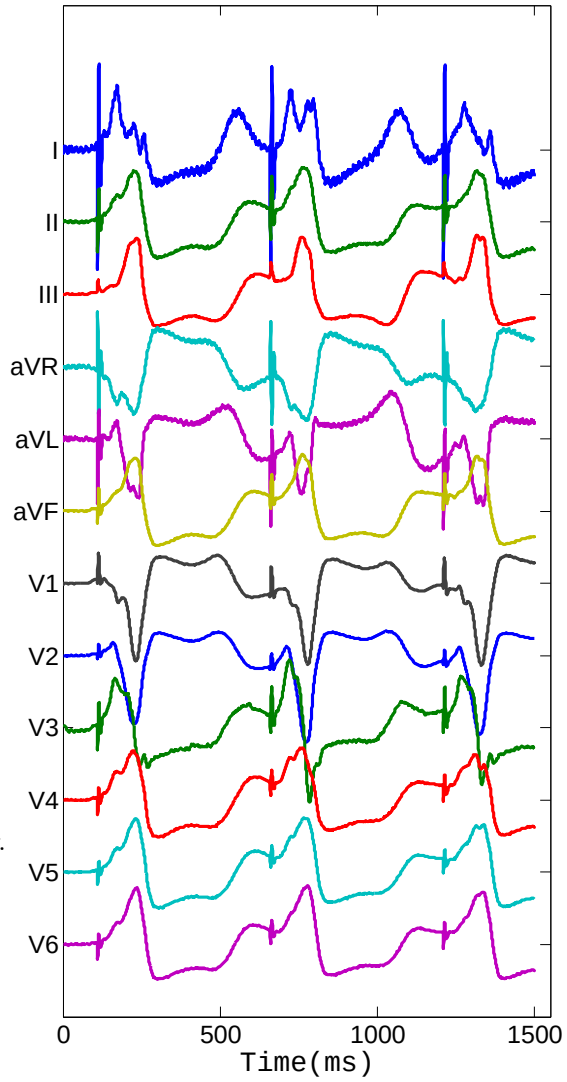


(b) A Real Time ECG Signal. The pacing is performed in the ventricle.

Figure 1.1: ECG Signals

also have VT without structural heart disease. In the absence of structural heart disease, ventricular arrhythmias, especially PVCs, are usually benign [13].

#### 1.2.2.2 VT Treatments and Cardiac Ablation

Two treatment options are available for VTs: medical therapy with antiarrhythmic medications to suppress VT or catheter ablation where VT is eliminated with local delivery of radiofrequency energy. VT is acutely terminated either by over-

driven pacing via a catheter or a defibrillator or by synchronized cardioversion via an external or internal defibrillator. Whereas overdrive pacing even if delivered via an implantable cardioverter defibrillator (ICD) is usually painless, terminating VT with a shock results in substantial discomfort to patients and has been reported to increase mortality rates [14]. Because suppression of VT with medication is often ineffective and can result in non-tolerated side effects, alternative therapy options have been developed. Catheter ablation using radiofrequency energy has been used to treat VT and has resulted in improvement of symptoms, reduction in morbidity, and improvement in survival in patients with prior myocardial infarctions [15, 16, 17].

Cardiac ablation for the VT treatment is performed using a radiofrequency (RF) catheter. A cardiac catheter is inserted into the heart and placed at a location on the ventricular heart wall that is suspected to be the origin of VT. Ablation of the tissues around the VT origin will stop the polarization that causes a different beat from the other parts of a heart. For the ablation procedure, a catheter is placed inside of the heart through blood vessels, e.g. the femoral vein or the femoral artery. The outside of the heart can be reached either by accessing the pericadial space (space surrounding the heart) with a puncture below the chest bone or by accessing the outside of the heart via open heart surgery. The tissue generating the VT, often scar tissues, is localized with mapping procedure by using pace-mapping. Once the origin of the VT has been identified, radiofrequency energy is delivered, and the arrhythmogenic substrate is destroyed. The success of RF catheter ablations in different types of heart disease has been demonstrated by many studies [18, 19, 20, 21, 22].

### 1.2.3 Signal Analysis and Machine learning in Electrocardiology

#### 1.2.3.1 Previous Work by Others

Since the invention of ECG, clinicians and researchers attempted to utilize ECG data beyond monitoring patients' current heart conditions. Through ECG signal

analysis, researchers have reportedly been able to classify abnormal heart rhythms (beats), stratify patient population, predict future cardiac events, and thereby determine patient prognoses. Over many years, ECG signal analysis has been standardized into two steps: (1) extracting an ECG feature and (2) constructing or selecting a classification model or an estimation model. These two steps differentiate the approaches. ECG feature extraction and feature selection are critical rate limiting steps.

In the 1960s, an initial study of ECG analysis with feature selection began. Blackburn et al. [23] extracted eight different visual criteria from 12-lead ECGs. At this time, since they used the term "code" instead of "feature", Blackburn et al. named this group of features the Minnesota Code. Using the Minnesota Code, they classified the patient population and abnormal rhythms by hand. After all the work with the Minnesota Code, Blackburn published a summary review paper stating that even though ECG is an objective record and gives valid information about arrhythmias and heart disease, human annotation and measurement errors produced features that were difficult for clinical experts to interpret [24]. Therefore, at the end of the paper, Blackburn insisted on the need for computer processing for making ECG analysis clinically useful.

In one of the first computerized analyses, Cox et al. [25] introduced amplitude-zone-time epoch coding (AZTEC), a smoothing of ECG signals for rhythm analysis. As a smoothing transformation, AZTEC simplifies the signal and reduces the signal noise. Due to the simplification and noise reduction, Cox et al. states that AZTEC would be an appropriate feature (termed as pre-processing) of ECG for a real-time analysis; in fact, AZTEC was later used in QRS complex detection and abnormal rhythm classification by Birman [26].

After the use of computer in signal analysis was popularized, ECG feature extractions using various types of transforms were introduced. In particular, in the paper by Gritzali [27], a wavelet transform was used to represent the ECG signal as a linear

superposition of orthogonal waveforms. The ECG feature from the wavelet transform was defined as the set of wavelet coefficients extracted from the ECG signal. Wavelet features were considered advantageous because (1) they are extracted from the full duration signal, (2) they are applied independently to multi-lead ECGs, (3) they reduce the dimension of the feature, and 4) they provide better signal approximation as compared to previous ECG features [27].

Subsequently, a combination of feature extraction using wavelet transform and classification using support vector machine (SVM) enjoyed the increasing popularity. Zhao et al. [28] combined wavelets and SVMs to achieve over 99% classification accuracy with 6 heart rhythm classes. Song et al. [29] reduced the feature dimension to only 4 linear combinations of wavelet coefficients by using linear discriminant analysis (LDA). The rhythm classification accuracy was over 99% for this method as well.

A modification in the SVM classifier was proposed in the paper by Übeyli [30]. Using the wavelet transform features for the ECG signals, Übeyli classified heart rhythms using SVM with error correcting output code (ECOC). Applying error correcting output codes, inspired from digital communication theory, automatically corrects possible erroneous classification by assigning a hamming code to each class. Übeyli compared the classification results from SVM with ECOC to the results from a multi-layer perceptron.

Lastly, Martis et al. [31] presented a comprehensive study in classifying heart rhythms using wavelet ECG features from nine different wavelet bases and three different classifiers (Gaussian mixture model, artificial neural network, and SVM). According to this paper, differences in the wavelet bases do not cause large differences in the classification accuracy, but the SVM classifier gives outstanding classification results compared to the other two classifiers.

Recently, a new ECG feature was introduced by Chia et al. [9] in an application of atrial fibrillation prediction. They used two methods, independent component anal-

ysis (ICA) and silence-energy minimization, to extract a novel ECG feature. Based on a priori knowledge about the average atrial activation time period, Chia et al. extract independent components from the ECG signals. Also, based on the knowledge that different ECG components originate from different phases of the electrical cardiac activation, the ECG was separated into atrial beats and ventricular beats using silence-energy minimization. These two feature extractions were designed for atrial fibrillation prediction, which is different from the objective of this thesis that deals with VT.

#### 1.2.3.2 Contribution of the Thesis

Most of the previous work in signal analysis and machine learning in electrocardiology has been developed to classify and predict heart rhythms. However, as stated in Section 1.1, the objective of this thesis is to identify the locations of VT origins. To do this, we use machine learning methods of cluster analysis, classification, and dimensionality reduction.

Before classifying VT and pace-map origins from ECG signals, the thesis reports on results of clustering patient groups and selecting ECG variables to design an effective ECG feature. The patient groups are clustered using spectral clustering method applied to cross-validated samples of patient-pairwise SVM classification performance used as an inter-patient distance metric. ECG signals along with their class labels are examined with sparse linear discriminant analysis (sLDA) [32]. This analysis found that the slopes in particular leads and time segments of the QRS complex are distinct for VTs and pace-maps originating from different locations in the heart and allow to separate into different classes, and based on the results, a novel ECG slope feature is designed. To the best of our knowledge, these two approaches are the first in using spectral clustering and sparse LDA for patient stratification and ECG feature selection, respectively.

For classifying and localizing the origin of VTs, the SVM is used as a baseline classification method throughout the thesis. Both linear and kernelized SVM are used, and all classifications are cross-validated with leave-one-patient-out, leaving out one patient's VTs and pace-maps as testing samples and using all the other patients' signals in training. This leave-one-patient-out cross-validation provides meaningful results because the inter-patient variation is large.

To produce accurate estimates of VT origin coordinates, the likelihood function between ECG signals and their corresponding myocardial coordinates is constructed with mixture models. The Von Mises-Fisher mixture model [33] is applied for coordinate estimation, and Gaussian mixtures are used for region estimation. The likelihood functions learned with Gaussian mixtures are utilized in classification of regions through likelihood-ratios test. This is the first time that the mixture models have been applied to pace-map location estimation and classification.

A novel manifold learning algorithm was developed to perform non-Euclidean dimensionality reduction on ECG data. This dimensionality reduction method, called Quaternion Laplacian Information Maps (QLIM), is an extension of Spherical Laplacian Information Maps (SLIM) and applied to visualize the ECG signal distributions.

Finally, we propose a new type of pace-map classifier that is implemented using a restricted Boltzmann machine (RBM). While the performance of the RBM is not as good as the mixture of Gaussian model that we introduced earlier in the thesis, the RBM provides a new methodological framework for the ECG classification. RBMs, and, more generally, deep learning architectures, require many training samples and we believe that the proposed RBM classifier can approach or exceed the performance once a larger training set of patient ECGs becomes available.

A summary of the contributions of this thesis is as follows:

- This thesis develops a machine learning algorithm that analyzes and clusters 12-lead ECG signals with the novel objective of localizing the myocardial origin

of VTs from pace-map data.

- The thesis proposes a new ECG feature and a classifier based on the mixture model to classify VT origins from ECGs.
- The thesis evaluates the use of restricted Boltzmann machines in ECG analysis.
- The thesis presents a novel manifold learning method called QLIM in order to reduce the dimensionality of ECG signals while preserving VT and pace-map origin information.
- The thesis introduces and analyzes ventricular arrhythmia ECG signals with intramural origins.
- The ECG analyses in this thesis use the VT and pace-map ECG dataset provided from the University of Michigan Cardiovascular Center. There are 3,277 12-lead pace-map ECGs and 51 VT ECGs collected from 43 patients. This corpus represents the largest pace-map dataset published to date, permitting the application of the machine learning methods proposed in this thesis.

## 1.3 Outline of the Thesis

Chapter II reviews the process of automated ECG analysis for localizing and classifying the origin of pace-maps and VTs. The ECG dataset is analyzed with sparse linear discriminant analysis to create new ECG features based on their regional differences of VT origins. A joint distribution of ECG signals and corresponding coordinates of the origins are obtained using mixture models. Using this model, both estimation of the origin coordinates and classification of the origins' regional categories can be performed. However, this thesis only presents experiments for the region classification due to the low spatial resolution of the available pace-map data.

In Chapter III, the restricted Boltzmann machine is applied to ECG analysis. First, the equivalence between Gaussian mixture model and Gaussian-softmax RBM is proven. Using the connection between the means of Gaussian mixtures and the columns of the weight matrix in RBM, the joint distribution of ECG signals and regional labels are described with Gaussian RBMs. Since the advantage of discriminative RBMs is its capability of learning an expressive relationship between ECG signals and labels, a classifier of the origin of pace-maps is modeled and tested.

Chapter IV introduces the new method of manifold learning. Quaternion Laplacian Information Maps, abbreviated as QLIM, is a manifold learning methodology that contributes to non-Euclidean dimensionality reduction and clustering. Unlike the previous methods of manifold learning, QLIM focuses on embedding into quaternion space. QLIM is demonstrated on both the ECG dataset and a turntable image dataset, acquired in the Vision Lab from the department of electrical engineering and computer science, with rotational variations.

In Chapter V, we consider classification of an unconventional ventricular arrhythmia (VA) with the site of origin located in the middle of the heart wall. These VAs, called intramural VAs, are associated with differently shaped ECG signals as compared to non-intramural VAs. By averaging the pace-map ECGs from different aspects of the myocardium (i.e. epicardium or endocardium) close to the target intramural VA, we obtain a signal that is highly correlated to the ECG of that target VA. The Pearson correlation coefficient and root mean square error are used to numerically measure the similarity among the pace-map ECGs, the combination signals, and the target VA ECGs.

## 1.4 Publications

The publications that have come out of research presented in this thesis are as follows.

**Journals**

[1] Mario Njeim*, **Dae Yon Jung***, Miki Yokokawa, Alfred O. Hero III, Eric Good, Fred Morady, Frank Bogun. *Electrocardiographic Characteristics of Scar Related Intramural Septal Ventricular Tachycardias*, in preparation.

[2] Miki Yokokawa*, **Dae Yon Jung***, Alfred O. Hero III, Kazim Baer, Fred Morady, Frank Bogun. *Single- and Dual-Site Pace Mapping of Idiopathic Intramural Ventricular Arrhythmias*, Heart Rhythm, 2015, in revision.

[3] Miki Yokokawa*, **Dae Yon Jung***, Kim K. Joseph, Alfred O. Hero III, Fred Morady, Frank Bogun. *Computerized Analysis of the 12-Lead Electrocardiogram to Identify Epicardial Ventricular Tachycardia Exit Sites*, Heart Rhythm, 2014.

(* indicates equal contribution)

**Conferences**

[1] **Dae Yon Jung**, Sungjin Kim, Alfred O. Hero III. *Quaternion Laplacian Information Maps for Dimensionality Reduction*, in preparation.

[2] Kihyuk Sohn, **Dae Yon Jung**, Honglak Lee and Alfred O. Hero III. *Efficient Learning of Sparse, Distributed, Convolutional Feature Representations for Object Recognition*, In Proceedings of 13th International Conference on Computer Vision (ICCV), 2011.

# CHAPTER II

# Analysis of Electrocardiograms for Localizing and Classifying Ventricular Tachycardia and Pace-map Origins

## 2.1 Introduction

A high dimensional signal is not the best representation of information; the latent information is not easily observed, and the computation becomes heavy. Therefore, an effective low dimensional feature should be extracted and selected from high dimensional data. The signal collected from a human heart for clinical purposes is one of these overwhelmingly high dimensional signals. The clinicians often need to answer simple questions, many times yes-no (binary) questions, in analyzing collected data. Electrocardiography, a recording of heart activities over the time domain, produces high dimensional signals that are useful descriptors of the status of a heart. By analyzing the electrocardiograms (ECGs), the information about the origin of ventricular tachycardia (VT) can be classified, and later the spacial coordinates of the VT origins on the heart surface can be precisely estimated.

Ventricular Tachycardia is an arrhythmia that is often caused by a dense fibrous scar created in the ventricles. To cure life-threatening VTs, an ablation procedure can be performed. Prior to the ablation, the origin of the VT needs to be identified,

and pace-mapping is a technique that helps identify the sites of origin of VT within scar tissue. Theoretically, if the catheter is at the site of origin (also called exit site), the ECG morphologies of the VT and the pace-map have to be identical. However, in today's clinical practice, pace-maps are analyzed by visual inspection. If the QRS complex morphology from more than 10 out of the 12 leads appears similar to a reference VT QRS morphology, the location of catheter where the pace-map was obtained is considered to be the origin for that VT. Figure 2.1 shows the overlapping between a reference VT signal and the corresponding pace-map from the site of origin. Two other pace-maps from the same patient are presented to show how the ECGs are different when pace-mapping is performed from other locations.

The ultimate objective in this chapter is to build the framework for estimating each pace-map's locational information within the heart from the temporal 12-lead ECG signals. Assuming that all patients' heart shapes can be mapped to a universal heart, which will transfer all the pace-maps from different patients to a universal coordinate, we can design a coordinate estimation model using the mixture model.

As an initial step toward this goal, a classification of VT origin being either the outside of the heart (Epicardium) or the inside of the heart (Endocardium) is reported in this chapter. In general, the QRS morphology that is generated by pacing from the catheter-tip that is used for mapping (the so called pace-map) is a surrogate of a VT that originates at the site where pacing is performed. Pace-mapping is performed throughout the cardiac surface, and the resulting pace-maps are considered to be the equivalents of VT. The pace-maps are used in this manner in this chapter.

The distinction between epicardial and endocardial origin can be viewed as a simple binary classification of epicardial and endocarial pace-maps. However, there are sources of variances. First, there is patient variance. Heart size, and cardiac location within the thorax, distance of the heart from the skin surface are not identical in every patient, neither is the location of scar and the scar architecture that deter-

mines the origin of the VTs. These factors among others cause different durations, amplitudes, and orientations of the ECG signals. Since all the pace-maps are not from a single patient, epicardial and endocardial pace-maps will have variances according to the patients. Second, VTs originating from different regions in the heart will have different QRS morphologies. Even though ECG signals from the inside of the heart are categorized as one endocardial class, the regional differences including origin within the right or left ventricle or origin at the anterior or posterior heart wall, etc., will result in different QRS morphologies. An appropriate classifier, therefore, needs to be able to correct for all the variabilities and select the correct property that distinguishes both classes.

This chapter followed with a brief explanation about the related work and background in Section 2.2. Section 2.3 describes the 12-lead ECG dataset that is used throughout the analyses in this chapter and the whole thesis. Section 2.4 describes the estimation model and the epicardial-endocardial ECG classification method. Also, analyses on ECG signals and patient clusterings are presented that help understand the dataset and the extracted ECG features. The experimental settings and the classification results are presented and discussed in Section 2.5. Lastly in Section 2.6, we conclude the chapter, and possible upcoming work to this project is discussed.

## 2.2 Background

### 2.2.1 Related Work

ECG analyses have been used in rhythm recognition [34] and arrhythmia prediction [9, 35] use the features of beat to beat analysis for comparison. For classification and localization of the VT origin, ECG features that represent complete characters of 12-lead ECGs need to be used. Cardiologists rely on physical properties of ECGs: the duration of QRS complex, the time interval from the beginning of the QRS complex

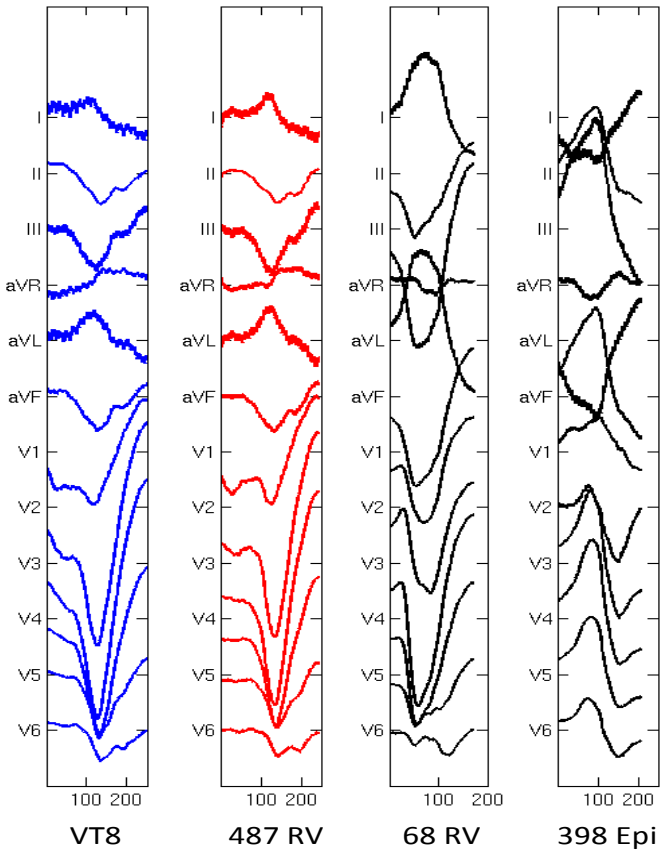


Figure 2.1: Patient 8's VT, Its Exit Site (489 RV) Pace-map, and Two Other Pace-maps

to the peak of the R wave, the QRS peak, etc. [36, 37]. Signal analysts use features built on the physical features: wavelets [35, 38], normalized energy [39], and neural networks [34, 40].

Yokokawa et al. [41] described the value of the QRS morphology using a computerized algorithm in localization of the VT origin. Using 774 pace-maps and 58 VTs, they were able to classify VTs into 10 endocardial regions in the left ventricle with a 70% accuracy. Berruezo et al. [37] reported a 87% sensitivity and 95% specificity for distinguishing epicardial from endocardial VT origins in 9 patients with 69 VTs from the left ventricle. Focusing solely on the absence of Q waves in 636 pace-maps and 19 VTs from 15 patients, Bazan et al. [42] demonstrated that features distinguishing epicardial from endocardial origins are site specific. More recently, Valles et al. [36] reported a 95% classification accuracy using a stepwise algorithm focusing on one

specific cardiac area to distinguish epicardial from endocardial origins.

The previous work assessing accuracy of VT origin tends to have a high classification rate. To put the prior work in the correct perspective, one needs to be aware of the exact datasets that are described in the different publications. The datasets are all limited to a select group of patients and a very narrow spectrum of VT origins (i.e. the basal left ventricular wall), and a small number of VT samples. The number of VT samples is in some of the publications complemented by sites of pace-mapping which is a legitimate way to increase the number of QRS morphologies that can be generated and analyzed per patient; unfortunately this method is underutilized in the prior reports. Furthermore, these studies did not report actual cross-validated classification rates. Rather they reported apparent error rates when the classifier is trained and tested in the entire sample. Thus these accuracy rates are often not achievable in practice.

### 2.2.2 Pace-mapping and its Procedure

Pace-mapping is a technique in cardiac electrophysiology (EP) to map the heart surfaces to its corresponding ECGs. For the purpose of transmitting an electrical stimulus and excite the heart locally, a mapping catheter (the same catheter can be used for both mapping and ablation) is positioned at the inside of the heart (endocardium) or the outside of the heart (epicardium). The placement of a catheter at the endocardium is less invasive since the catheter is inserted into the blood vessels and then directed to the endocardium. It is more invasive to reach the epicardium and requires a puncture of the pericardial space below the sternum. This approach has more potential complications and should only be performed by experienced operators. Rarely open heart surgery is needed to place the catheter outside of the heart. For exact tracking the catheter , the tip contains a localization sensor that can be tracked in the three dimensional space with an accuracy of 1 mm. The location of sites

where pace-maps are generated can thereby be recorded with high accuracy. They are reported as xyz coordinates on the 3D map.

In a given patient, after informed consent is obtained, a 6F quadripolar electrode catheter is introduced into a femoral vein and positioned at the right ventricular apex. Programmed right ventricular stimulation is performed with 1-4 extrastimuli to induce VT [43]. Once the VT is induced and terminated, the mapping procedure starts. The mapping procedure uses three dimensional data that are obtained by touching the cardiac walls with the mapping catheter. A system that is often used is the CARTO system (Biosense Webster, Inc., Diamond Bar, CA, USA) in combination with a 3.5-mm-tip, open-irrigation ablation catheter (Thermocool Navistar, Biosense Webster). Electrograms are filtered at 50-500 Hz. The intracardiac electrograms and leads V1, I, II and III are displayed on an oscilloscope and recorded at a speed of 100 mm/sec. The recordings are stored on optical disc (EPMed Systems, West Berlin, NJ, USA). A voltage map of the left ventricle is generated during sinus rhythm and consists of touching the wall of the endocardium with the mapping catheter and recording the local electrograms at each site of contact. The voltage determines the tissue integrity;. low voltage is defined as bipolar voltage with an amplitude $<1.5$ mV [44]. It indicates scar tissue whereas normal voltage $\geq 1.5$ mV indicates healthy tissue. Epicardial access is performed as needed if arrhythmias can not be localized to the endocardium using a subxyphoid approach described by Sosa et al. [45].

Pace-mapping is performed mainly from within the low-voltage areas in patients with cardiomyopathy. The cycle length of pace-mapping is that of the targeted VT. Pace-mapping is performed uniformly throughout the low voltage area at sites where the local electrograms differ from the prior mapping site. Pace-mapping is also performed at normal voltage sites in an attempt to evenly cover endocardial and epicardial surfaces. Two consecutive captured beats are required for analysis.

### 2.2.3 Sparse Linear Discriminant Analysis

Linear Discriminant Analysis (LDA) is a supervised classifier that seeks for the largest separation among the data according to their class labels. In the procedures of LDA, it projects the data onto the most discriminant directions in a lower dimensional space, which helps the interpretation of the data [32].

The formulation of LDA is to maximize the between-class covariance and minimizing the within-class covariance. Let's $X$ be the $n$ by $p$ data matrix with each row $x_i$ is a $p$ dimensional data vector. All $n$ samples have a class label from $K$ possible classes. The between-class covariance matrix is defined as $\Sigma_b = \sum_{k=1}^{K} \mu_k \mu_k^T$, where $\mu_k$ is the mean vector of class $k$. The within-class convariance matrix is defined as $\Sigma_w = \frac{1}{n} \sum_{k=1}^{K} \sum_{i \in C_k} (x_i - \mu_k)(x_i - \mu_k)^T$, where $C_k$ is the indices of the data vector in the $k$th class. The $K-1$ discriminant vectors, $\beta_k$, can be optimize by maximizing

$$\underset{\beta_k}{\text{maximize}} \quad \{\beta_k^T \Sigma_b \beta_k\} \quad \text{subject to} \quad \beta_k^T \Sigma_w \beta_k = 1, \beta_k^T \Sigma_w \beta_l = 0 \quad \forall l < k \tag{2.1}$$

In the paper by Clemmensen et al. [32], a sparse LDA (sLDA) is introduced by adding $\ell_1$ penalty to the discriminant vectors. However, the within-class covariance is not full rank when $p > n$, and it causes the optimization challenging. Therefore, Clemmensen et al. use the other formulation that yields the LDA, called optimal scoring, which is presented in the paper by Hastie et al. [46]. This formulation adds two new variables: optimal score $\theta_k$ and class indicator matrix $Y$. $Y$ is a $n$ by $K$ matrix, where $Y_{ik} = 1$ if $x_i$ belongs to $k$th class. Also, a positive definite matrix $\Omega$ is added to prevent $\Sigma_w$ from not having full rank. Sparse LDA optimization is achieved by solving

$$\begin{aligned} \underset{\beta_k,\theta_k}{\text{minimize}} \quad & \{||Y\theta_k - X\beta_k||^2 + \gamma\beta_k^T\Omega\beta_k + \lambda||\beta_k||_1\} \\ \text{subject to} \quad & \frac{1}{n}\theta_k^T Y^T Y\theta_k = 1, \theta_k^T Y^T Y\theta_k = 0 \quad \forall l < k, \end{aligned} \tag{2.2}$$

where $\gamma$ and $\lambda$ are the tuning parameters. When $\lambda$ is large, $\beta_k$ becomes a sparse vector. The paper by Clemmensen et al. describes how to solve this optimization problem, and the access to the code is open to the public by the authors.

### 2.2.4 Mixture Model

A mixture model is a statistical model describing the distribution of the whole dataset with a set of possibly overlapping concentrated distributions, each representing a distinct cluster. The specification of a mixture model requires a set of mixture distributions and mixture parameters. These parameters, also called coefficients, describe the proportional contribution of a given mixture component to the overall distribution. A general expression for a mixture model is,

$$f_{MM}(\mathbf{x}) = \sum_{k=0}^{K} \pi_k f^{(k)}(\mathbf{x}; \theta_k). \tag{2.3}$$

$\pi_k$ is the weight of each mixture, and $f^{(k)}$ is a probability distribution with parameters, $\theta_k$. The distribution of the mixture components can be any distributions, and in this chapter, we will use the Gaussian distribution and the Von Mises-Fisher distribution [33].

Mixture models are commonly used in applications due to the simplicity of training using the expectation maximization (EM) algorithm. Gaussian mixtures are the most widely used in the applications involving continuous distributions.

#### 2.2.4.1 Gaussian mixture models

The likelihood function of inputs using the Gaussian mixture model (GMM) is expressed as a convex combination of the Gaussian distributions. The expression for the Gaussian mixture model (GMM) with $K+1$ Gaussians can be written as follows:

$$f_{gmm}(\mathbf{v}) = \sum_{k=0}^{K} \pi_k \mathcal{N}(\mathbf{v}; \boldsymbol{\mu}_k, \boldsymbol{\Sigma}_k) \tag{2.4}$$

This notation of GMM is used throughout this chapter and in Chapter III.

## 2.3 Dataset: Electrocardiograms from Pace-mapping and VTs

### 2.3.1 The Dataset of Pace-map Signals

The pace-maps were collected from 43 different patients. The total number of pace-maps was 3,277; however, the number of pace-maps from a single patient varied from 4 to 227. Out of those 3,277 pace-maps, there were 1,696 epicardial and 1,581 endocardial pace-maps. The balance between epicardial and endocardial pace-maps was not always even for each patient; however, the overall ratio of epicardial to endocardial pace-maps was balanced (51.8% epicardial and 48.2% endocardial pace-maps).

From each 12-lead ECG morphology, a single QRS complex was manually labeled. Therefore, the size of a raw input pace-map signal to start the classification was 12 by the length of QRS complex ($\mathbf{t}$).

For each pace-map, in addition to the endocardial and epicardial origin, other labels were provided:

1. The pacing site location either from the left or right ventricle. The left ventricle wass divided into 10 regions (A-J), and the right ventricle was divided into 4 regions (K1, K2, L1, and L2). Considering that each section has an epicardial

part and an endocardial part, except for the 6 septal regions (A, B, E, F, L1, L2) which only have endocardial parts, there were a total of 22 possible regions where pacing was performed. For a pictorial description of the heart regions, see Figure 2.2.

2. The type of structural heart disease for each patient. Four distinctions were made specifying the cardiac disease process in each of the 43 patients:
   (a) Idiopathic ventricular arrhythmia in patients without structural heart disease
   (b) Non-ischemic cardiomyopathy
   (c) Ischemic (post-infarction) cardiomyopathy
   (d) Arrhythmogenic right ventricular dysplasia/cardiomyopathy

3. The bipolar voltage of pace-mapping locations. If the bipolar voltage was $\geq$1.5mV, it was considered as normal voltage tissue. If the bipolar voltage was $<$1.5mV, the tissue was considered abnormal indicating scarring.

4. The time delay from the pace-mapping stimulus to the beginning of the QRS complex.

5. The QRS width.

Any of these labels can cause irregularity in the ECG morphology and would affect ECG analysis including the epicardial and endocardial classification. Hence, there is a need to collect these extra labels and analyze the data within these subcategories.

### 2.3.2 The Dataset of Validation ECG Signals

Prior to the procedure of pace-mapping, VTs were induced to gather all the VT morphologies that required ablation treatment. The origin of the VTs was then identified by pace-mapping that allowed for ablation of the VTs. Those VTs where the site of origin was identified by pace-map were used for validation of the classification.

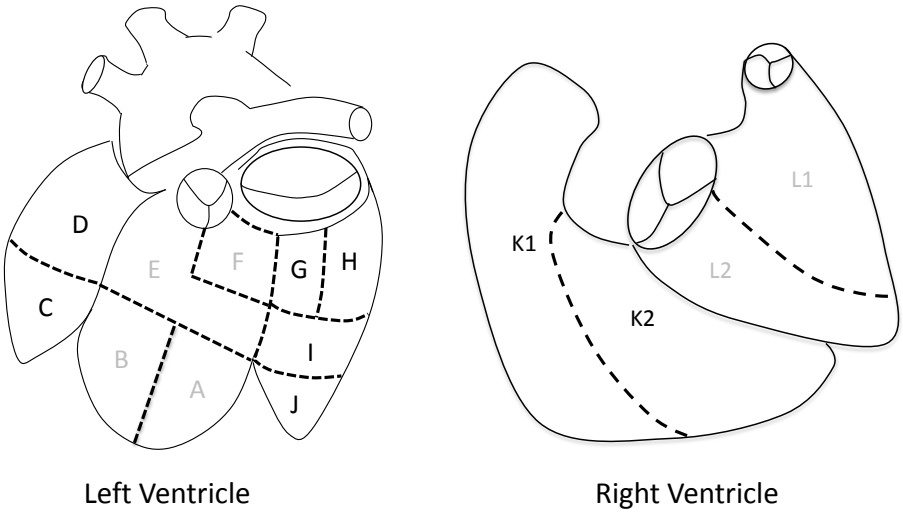


Figure 2.2: Left and Right Ventricle Regions. The region labels in gray are the septal regions with only endocardial sites.

The 12-lead ECGs of 51 VTs from a subgroup of 26 patients were selected to validate the pace-mapping data. Sites with the stimulus to QRS interval time $\leq$ 30 % of the VT cycle length where the pace-mapping morphology matched the VT morphology in $\geq 10/12$ leads were defined as the exit site.

## 2.4 ECG Analysis: Estimation and Classification

### 2.4.1 The Model among Pace-maps, Category Labels, and Coordinates

When the pace-maps are all collected, we have the following variables:

- $\mathbf{X} \in \mathbb{R}^d$ : A $d$ dimensional ECG signal from each pace-map point
- $\mathbf{y} \in \mathbb{Z}$ : A regional category label about the pace-map origin's region
- $\mathbf{Z} \in \mathbb{R}^3$ : A 3 dimensional coordinate of the pace-map origin

The assumptions in modeling the mapping between the $d$ dimensional signal space and the 3 dimensional coordinate space is as follows:

1. There is a universal heart space that all the patients can map their own hearts' coordinates.

2. The shapes of the left and right ventricles from the universal heart are deformations of unit spheres in S2, similar to those of left and right ventricular chambers.

3. The distribution of the pace-map sites in the coordinate space ($\mathbb{R}^3$) follows the Von Mises-Fisher distribution. Note that the pace-mapping coordinates on the heart surface can be homeomorphically deformed to a unit sphere since the ventricular chamber is topologically identical to a sphere.

4. The distribution of the pace-map signals in the signal space ($\mathbb{R}^d$) follows the multivariate Gaussian distribution over a $d$ dimensional Euclidean space. Note that the ECG signals do not lie on a unit sphere unless they are pre-normalized by dividing by the signals' Euclidean norms (root mean square energy).

Based on these assumptions, we construct a model of the pace-map origin coordinates from given ECG signals. In the classification problem, a model of the pace-map origin regional label given an ECG is constructed.

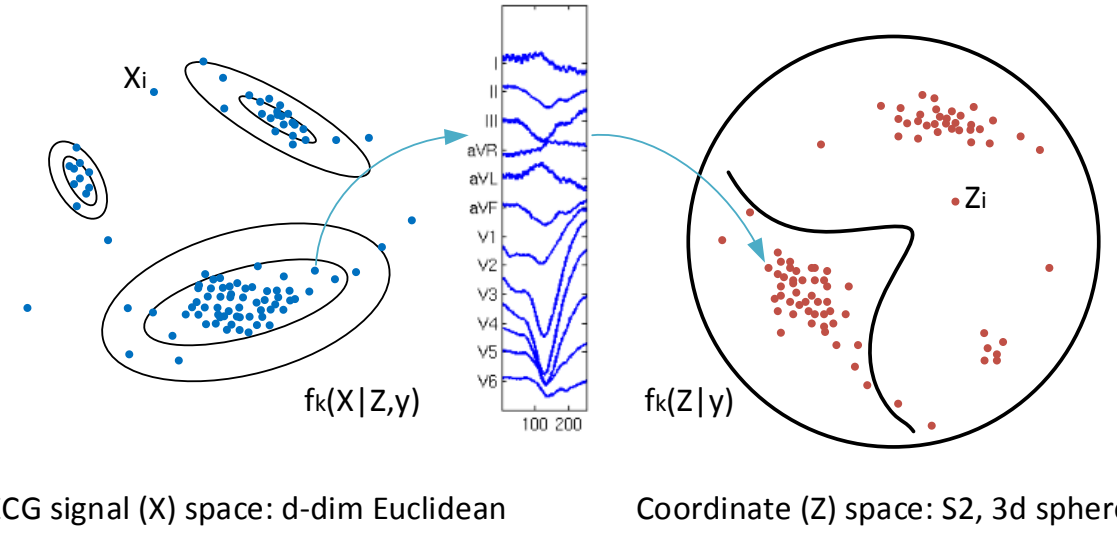


Figure 2.3: A Mapping Between the Pace-map ECGs and the Coordinates

#### 2.4.1.1 MAP Estimation of Coordinates Using Mixture Model

The objective of the pace-map origin reconstruction problem is to estimate the coordinate value $\mathbf{Z}$ when an ECG signal $\mathbf{X}$ is given. $\mathbf{Z}$ can be estimated using the

maximum a posteriori (MAP) estimation approach with a mixture distribution function. MAP estimation starts from maximizing the conditional probability of $\mathbf{Z} \mid \mathbf{X}, \mathbf{y}$.

$$\begin{aligned} &\max_{\mathbf{Z}} f(\mathbf{Z} \mid \mathbf{X}, \mathbf{y}) \\ f(\mathbf{Z} \mid \mathbf{X}, \mathbf{y}) &= \frac{f(\mathbf{Z}, \mathbf{X} \mid \mathbf{y})}{f(\mathbf{X} \mid \mathbf{y})} \\ \Longrightarrow &\max_{\mathbf{Z}} f(\mathbf{Z}, \mathbf{X} \mid \mathbf{y}) \end{aligned} \tag{2.5}$$

This joint probability $f(\mathbf{Z}, \mathbf{X} \mid \mathbf{y})$ is modeled as a sum of mixtures. In this process, the joint probability is separated to a likelihood function and the prior distribution.

$$f(\mathbf{Z}, \mathbf{X} \mid \mathbf{y}) = \sum_{k=0}^{K} \pi^{(k)}(\mathbf{y}) \cdot f^{(k)}(\mathbf{X} \mid \mathbf{Z}, \mathbf{y}) \cdot f^{(k)}(\mathbf{Z} \mid \mathbf{y}) \tag{2.6}$$

In this $K+1$ mixture model, the likelihood represents the distribution in the signal space, which follows the multivariate Gaussian as assumed previously. The posterior is the distribution in the coordinate space, and this is in Von Mises-Fisher distribution.

$$\begin{aligned} f^{(k)}(\mathbf{X} \mid \mathbf{Z}, \mathbf{y}) &\Rightarrow \mathcal{N}(\mathbf{X}; \boldsymbol{\mu}_k, \boldsymbol{\Sigma}_k) \\ f^{(k)}(\mathbf{Z} \mid \mathbf{y}) &\Rightarrow \phi_{vMF}(\mathbf{Z}; \boldsymbol{\mu}_k, \boldsymbol{\kappa}_k) \end{aligned}$$

#### 2.4.1.2 Classification using Mixture Model

A classifier should be able to identify the set of categories, the regional index $\mathbf{y}$, to which the test ECG signal belongs. Likelihood based classification maximizes the likelihood ratio, defined as the ratio of the posterior distribution of one class divided by that of a reference class. The classification decision regions are defined by this maximization and lie in the space of ECG signals $X$. The distance between the

distributions, e.g., as measured by Kullback-Liebler distance, determines the accuracy of the classifier.

The objective in classifying pace-map ECGs is to find out the category label $\mathbf{y}$ from the given ECG signal $\mathbf{X}$. $\mathbf{y}$ can be estimated similarly to Equation 2.5 but without the coordinate variable $\mathbf{Z}$.

$$\max_{\mathbf{y}} f(\mathbf{y} \mid \mathbf{X}) \rightarrow \max_{\mathbf{y}} f(\mathbf{y}, \mathbf{X}) \tag{2.7}$$

The joint probability $f(\mathbf{y}, \mathbf{X})$ has a similar form to Equation 2.6.

$$f(\mathbf{y}, \mathbf{X}) = f(\mathbf{X} \mid \mathbf{y}) \cdot f(\mathbf{y}) = \left[ \sum_{k=0}^{K} \pi^{(k)}(\mathbf{y}) f^{(k)}(\mathbf{X} \mid \mathbf{y}) \right] \cdot f(\mathbf{y}) \tag{2.8}$$

From this mixture model, the distribution of the data given a category is learned with Gaussian mixtures. Since the distribution of the regional categories $f(\mathbf{y})$ is a function representing the proportion of samples in each category, it is fixed independently of the mixture components. In a Bayesian binary classification problem with $\mathbf{y} = 0$ or $\mathbf{y} = 1$, the largest of $f(\mathbf{X}, \mathbf{y} = 0)$ and $f(\mathbf{X}, \mathbf{y} = 1)$ determines the class assigned to $X$.

$$H_0 : \mathbf{X} \sim f(\mathbf{X}, \mathbf{y} = 0)$$
$$H_1 : \mathbf{X} \sim f(\mathbf{X}, \mathbf{y} = 1)$$

When the label $\mathbf{y}$ does not have a prior probability, the theory of most powerful tests specifies the best binary classifier having a particular false alarm level [47]. By the Neyman Pearson Lemma [48], the most powerful test at a given false alarm rate $\alpha$ is as follows:

$$\Phi(\mathbf{X}) = \begin{cases} 1, & \text{if } f(\mathbf{X} \mid \mathbf{y} = 0) < \eta f(\mathbf{X} \mid \mathbf{y} = 1) \\ q, & \text{if } f(\mathbf{X} \mid \mathbf{y} = 0) = \eta f(\mathbf{X} \mid \mathbf{y} = 1) \\ 0, & \text{if } f(\mathbf{X} \mid \mathbf{y} = 0) > \eta f(\mathbf{X} \mid \mathbf{y} = 1) \end{cases} \tag{2.9}$$

,where $q$ and $\eta$ are chosen according to the false alarm rate $\alpha$ [1].

### 2.4.2 Feature Extraction for Epicardial and Endocardial ECG Classification

In the perspective of signal analysis and machine learning, performing a classification from an unknown, complex dataset is designed as a two-step process: feature extraction and classification. Most of the time, the information that is needed for classification is not apparent from the raw data. Training a classifier, such as support vector machine (SVM), on the high dimensional unprocessed raw data will not necessarily result in high classification accuracy. Projection of the raw data onto a lower dimensional space prior to training the classifier is a pre-processing method that can be used to reduce dimensionality. This dimension reduced, derived data is called a "feature", and the preprocessing step is called "feature extraction."

Support vector machine [49], which finds a separating hyperplane in the Euclidean data space, is widely used and generally known for fast optimization and accurate results [50]. If there is a large number of samples, mixture models can be used to learn distributions of the data points. Using these learned distributions from each class of data, the likelihood ratio test can be implemented to classify the labels. Selecting an appropriate classification method on the basis of implementation complexity, model accuracy, number of available training samples, and other criteria is important.

In order to figure out the class separating criteria among the pace-maps, discriminant vectors of sparse linear discriminant analysis (sLDA) [32] were analyzed.

[1] $\alpha = q \cdot \mathbf{P}\left[f(\mathbf{X}, \mathbf{y} = 0) = \eta f(\mathbf{X}, \mathbf{y} = 1) \mid H_0\right] + \mathbf{P}\left[f(\mathbf{X}, \mathbf{y} = 0) < \eta f(\mathbf{X}, \mathbf{y} = 1) \mid H_0\right]$

sLDA was performed 43 times, once for each set of pace-maps from a single patient, which eliminates the patient variance while doing each analysis. The QRS complex, the region of interest from each ECG signal for analysis (refer to Chapter I Section 1.2.1), was divided into three regions (front, middle, and end), and the number of active peaks in the sLDA discriminant vector was observed. From Figure 2.5, which is a histogram of number of activation (non-zero amplitudes in sLDA discriminant vector) in each region for all twelve leads, it is apparent that the middle region has the most activation compared to the other two regions. Generally, the peak of the R waves are located in the middle part. The amplitudes of the R wave peaks, the slopes of reaching and ending R wave peaks, and/or the locations where R wave peaks are located (time interval from the beginning of the QRS complex to the peak of the R wave) can be the possible properties that make sLDA to focus more on the middle region of the QRS complex.

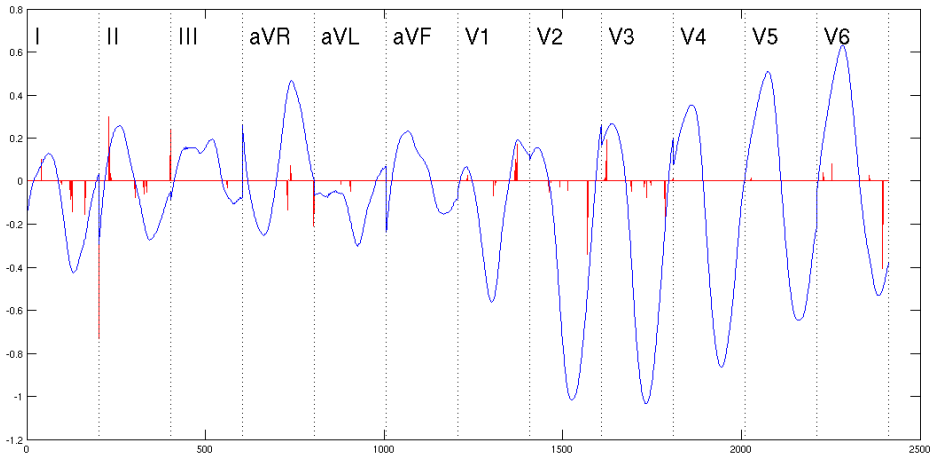


Figure 2.4: Averaged ECG Signal (blue) of a Single Patient's Pace-maps and Its sLDA Discriminant Vector (red) Overlapped

The regions with high amplitudes in sLDA discriminant vector were analyzed additionally. Higher amplitudes indicate that sLDA is holding more weight to those parts in separating the data according to classes. As shown in Figure 2.6, the region with a high-amplitude activation has an apparent difference in QRS complexes of the

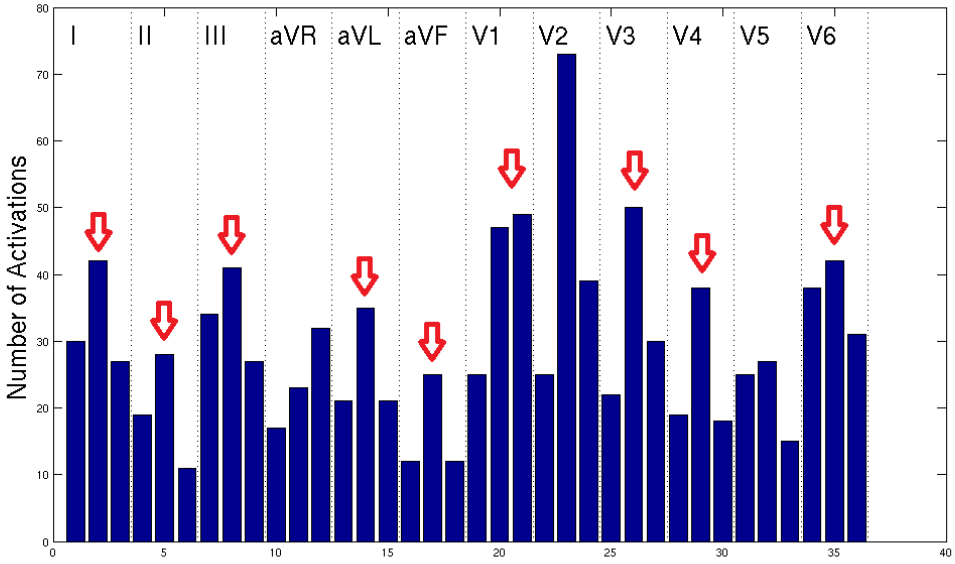


Figure 2.5: Histogram of Number of Activations from sLDA Discriminant Vectors in the Front, Middle, and End of QRS Complexes. The middle region of QRS complexes generally have more activations compared to the front and end regions.

displayed pace-maps. Focusing the analysis on this region for feature identification was beneficial for the distinction of epicardial and endocardial pace-map origins. For instance, sLDA of the patient's pace-maps shown in Figure 2.6 has the highest activation in the last part of V6. When actual pace-maps were examined, epicardial and endocardial signals have different slopes tendencies in that region. This is suggesting that the slope in the final part of the QRS complex is different for epicardial and endocardial pace-maps.

However, each patient has different regions of interest when decomposed by sLDA. In order to include all the information, a new feature consisting of local slopes was extracted. The QRS complex was divided into 9 equidistant segments, and the slopes in these small regions were calculated and concatenated to a single vector. Therefore, instead of analyzing the raw signal or some projected signal by PCA or LDA, the slope information throughout the signal was used to categorize the origin of the pace-maps. This was done for all 12 leads; however, through sLDA, we found that some

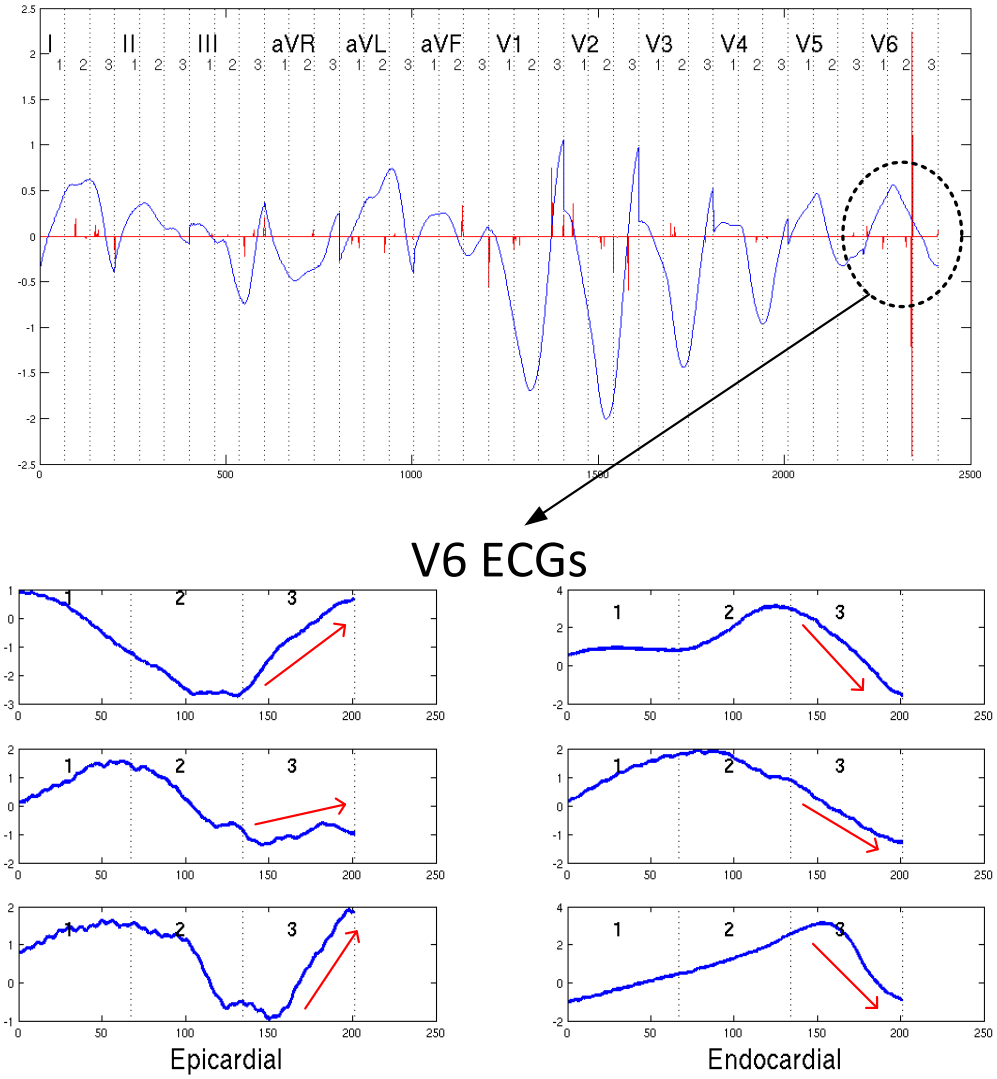


Figure 2.6: A patient's sLDA Discriminant Vector and his/her Exemplary Epicardial and Endocardial lead V6 ECG Signals

leads ahad less distinguishing value compared to others. Figure 2.6 shows that the patient analyzed has less activations in lead II, III, V4, and V5. Therefore, the new slope feature only selected 8 leads instead of all 12 leads, which generally gave less variance over all patients.

Therefore, the feature that we used for the classification of epicardial and enocardial VT and pace-map origins was the slopes of each lead in equi-divided regions (called the "slope feature" in this thesis). The steps from the analysis using sLDA to the extraction of the slope feature are shown in the Figure 2.7.

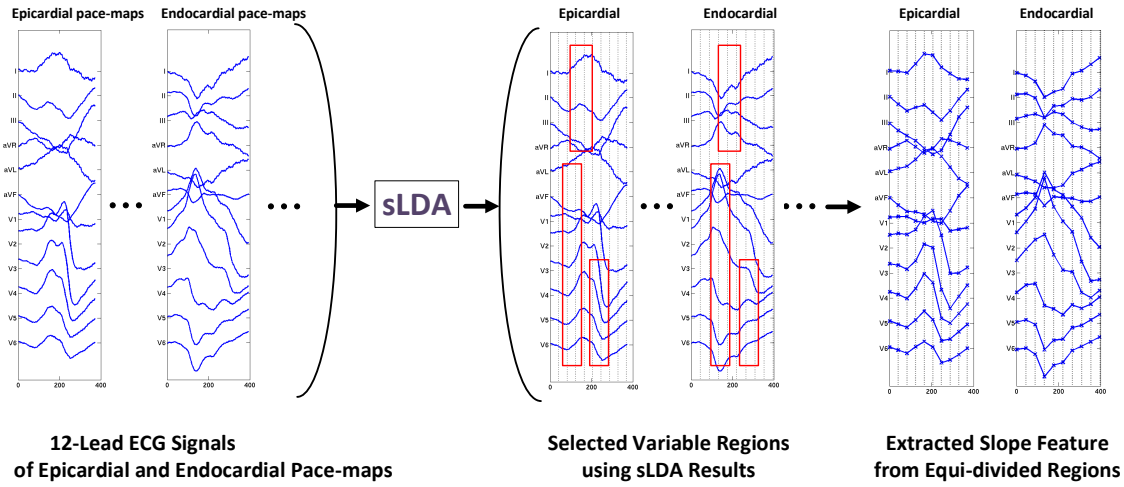


Figure 2.7: The Flow of Analysis and Extraction of the "Slope Feature"

### 2.4.3 Patient Group Analysis

High data variability is a common problem encountered in analyzing ECG data, and more probably any medical data. The human ECG data has notoriously high variability due to the many factors that determine cardiac function, stress, disease, circadian rhythm, etc. Even simple differences such as variability in heart size and torso size may cause variations in the amplitude and orientation of the QRS complex. Also, if a patient has a particular cardiomyopathic process, this may impact on the QRS morphology.

In the context of estimating and classifying pace-map and VT origins, these variances are a major challenge to be overcome. We proposed a method to stratify the patient population in terms of their signal differences using difficulty of pace-map site classification as a stratification measure. In this section, the 43 patients in the dataset were analyzed and compared in order to observe how the cluster of patient groups are formed based on their classification accuracy results.

The proposed measure proceeded as follows. First, an affinity matrix among the patients was calculated. If two patients' ECG characteristics are similar to each other, the mixed pace-maps from the two patients will perform classification as well

as training and testing from a single patient's pace-map ECGs. Thus, for every pair of patients, the two patients' pace-maps were merged to a single set of ECG data, and epicardial versus endocardial classification was performed with 4-fold cross-validation. Out of the 43 patients that we have, 7 patients (patient 20, 23, 27, 36, 38, 41, 42) were excluded because they had two or less pace-maps in either one of the classes. The remaining 36 patients were paired, resulting in $\binom{36}{2}$ pairs, and 4-fold cross-validation on epicardial and endocardial classification were performed for each pair using only the data from that pair.

With the affinity matrix constructed with the classification accuracy, patients were clustered with spectral clustering. Specifically, the eigendecomposition of the pairwise affinity matrix was performed, and the two eigenvectors associated with the two largest eigenvalues were computed. These two eigenvectors were used to form a $36 \times 2$ matrix which was left multiplied by the diagonal $2 \times 2$ matrix of square root eigenvalues. Each row was plotted as ordered pairs in Figure 2.8a. To help visualize the clusters and the affinity of each patient node, all nodes were connected with the minimal spanning tree (MST) in Figure 2.8b.

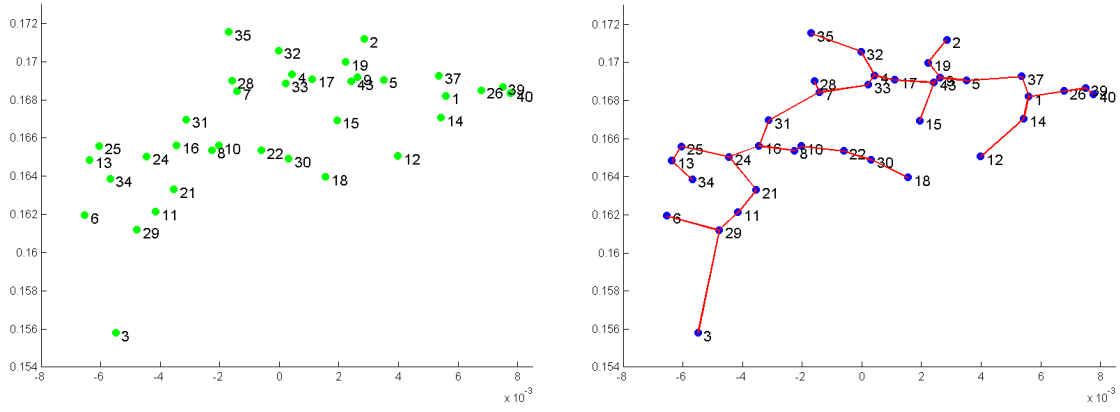

(a) Spectral Clustering of 36 Patients

(b) Patient Clusters Graphed with Minimal Spanning Tree

Figure 2.8: Spectral Clustering on the Patient Affinity Matrix

In this visualization, some clusters of patients appear and others appear to be

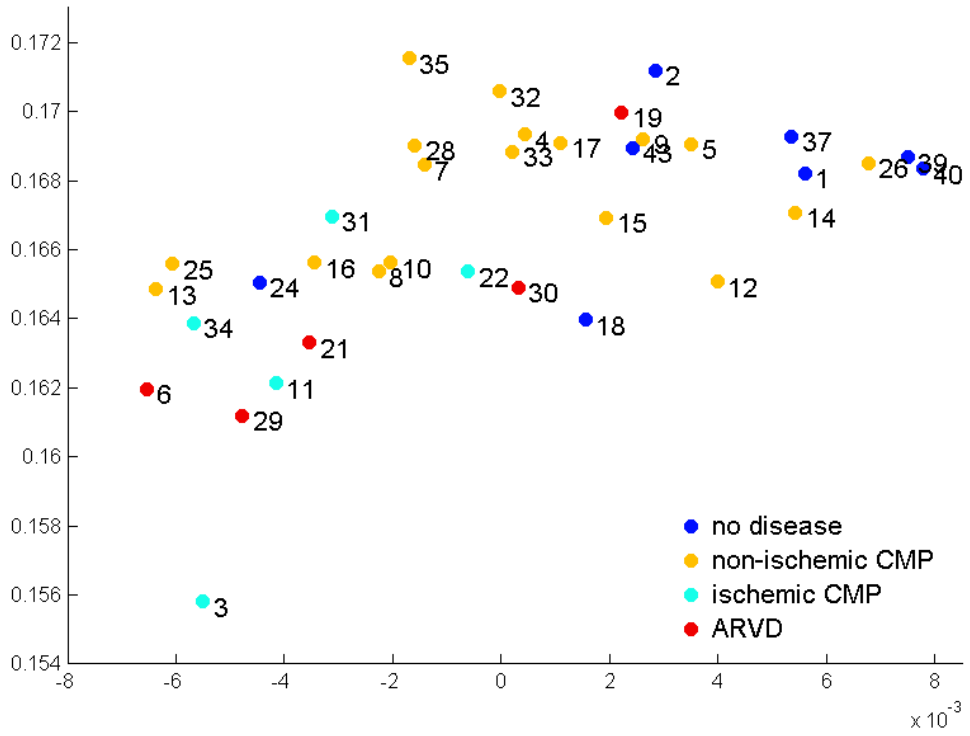


Figure 2.9: Patient Clusters Labeled with Structural Heart Disease Symptoms. The colors indicate different structural heart disease type that each patient has. Blue: no structural heart disease, Yellow: non-ischemic cardiomyopathy, Light Blue: ischemic cardiomyopathy, Red: arrhythmogenic right ventricular dysplasia.

outliers. Specifically, a normalized minimum cut of the MST in Figure 2.8b produces two clusters separated by the cut link between patient 31 and 7. Also, we can see how patient 1, 4, and 16-24 together are central to the clusters. Patient 3, 6, and 35 are patients that diverge from the clusters. There were no significant biographical or medical particularities found for those patients diverging from the group. However, the labels of each patient's structural heart disease history reveal some structure in the graph.

In Figure 2.9, clusters of patients with the same structural heart disease history can be observed. There are indeed overlaps among the patient groups, but there is a trend separating different groups. Patients without structural heart disease are located on the right side of the spectrum, whereas patients with structural heart disease tend to

be on the left of the spectrum, and patients with nonischemic cardiomyopathy (yellow dots) are spread over the entire spectrum.

The outlyers to the general trend in Figure 2.9 graph are patients 19 and 24. Patient 19 has arrhythmogenic right ventricular dysplasia (ARVD) but is closer to the patients with no heart disease. In contrast, patient 24 has no heart disease but is in the left side of the scatter along with the patients with structural heart diseases. These outlier patients indicate that structural heart disease labels are not the single factor that instigates the clusters based on classification accuracy affinity. However, this patient clustering analysis shows that each patient's ECGs have stronger similarities to a particular group of patients over other groups.

## 2.5 Experiments and Results

### 2.5.1 Experimental Settings for Training and Testing

Since 3,277 pace-maps were from 43 different patients, the patient variability had to be considered. In fact, if two different pace-maps from the same patient are one in the training set and the other in the testing set, the classification accuracy increases significantly. To reduce the generalization error, the testing pace-maps had to be completely blinded to the classifier during training. Therefore, data from different patients were placed in the respective training and testing sets. If one patient's pace-maps were used for testing the classifier, only the other 42 patients' pace-maps were used for training the classifier. All 43 patients were tested by the feature extraction and the classification method introduced in Section 2.4, and both the average classification accuracy over these 43 runs and the accuracy over the total number of pace-maps were reported in Table 2.5.

### 2.5.2 Epicardial and Endocardial Classification Over All Pace-maps

The overall accuracy using the mixture model was 84.48% over patients and 80.38% over the total number of samples. The sensitivity and specificity was 80.96% and 79.76% over all pace-map samples. For detailed results over all the patients, see Table 2.5 attached at the end.

When patients with and without structural heart disease were compared, the accuracy of the computerized algorithm in patients without structural heart disease was 92.74% (averaged over each patients) and in patients with structural heart disease was 80.45%. The accuracies in patients with structural heart disease ranged between 77.38% (arrhythmogenic right ventricular cardiomyopathy) and 81.13% (idiopathic cardiomyopathy) in patients with structural heart disease. It was 80.96% in patients with coronary artery disease. Pace-mapping sites with higher bipolar voltage (>1.5 mV) had a higher accuracy (81.57%) as compared to low voltage (≤1.5 mV) sites (79.57%).

| Structural disease | # of patients | # of pace-maps | Classification Accuracy |
|---|---|---|---|
| No heart disease | 14 | 468 | 92.74 |
| ARVD | 6 | 566 | 80.96 |
| Non-ischemic CMP | 18 | 1704 | 81.13 |
| Ischemic CMP | 5 | 554 | 77.38 |

Table 2.1: Classification Accuracies by Structural Heart Diseases

This shows that the patients with no structural heart disease and the normal (high bipolar voltage) heart tissue tend to give a better classification accuracy. We can interpret that the pace-map under the normal category that we defined has more definite distinction of epicardium and endocardium.

For the last, accuracy varies from region to region; ranging from 67.62% (right ventricle) to 86.78% (basal left ventricle). It is apparent that in general pace-maps from the left ventricle were more distinct when epicardial signals were compared to endocarial signals.

| Regional Category | Left Ventricle | | | | | | Right Ventricle | |
|---|---|---|---|---|---|---|---|---|
| | C | D | G | H | I | J | K1 | K2 |
| Number of Samples | 255 | 711 | 224 | 255 | 250 | 183 | 458 | 525 |
| Accuracy (%) | 81.18 | 86.78 | 83.04 | 81.57 | 82.80 | 74.32 | 78.17 | 67.62 |

Table 2.2: Classification Accuracies by Regions

### 2.5.3 Validation with VTs

The classification accuracy for the 51 VTs for which exit sites were determined was 84.31% for differentiating epicardial from endocardial origins with a sensitivity of 88.89% and a specificity of 79.17%.

### 2.5.4 Comparisons with Other Classifiers

This 80.38% classification accuracy had to be compared with other generally known classifiers. Using singular vector machine (SVM) with the slope feature as the input, the results were significantly lower than that of the mixture model classifier (LIBSVM [51] was used for SVM training and testing). These low classification accuracies happened for both linear and kernelized SVMs, which implied that the distribution of the pace-maps are not easily separable by hyperplanes in the feature space.

| Classifier | Classification Accuracy | Sensitivity | Specificity |
|---|---|---|---|
| SVM (linear) | 50.71% | - | - |
| SVM (poly) | 66.66% | - | - |
| SVM (radial basis) | 71.93% | 75.06% | 68.56% |
| Mixture Model | 80.38% | 80.96% | 79.76% |

Table 2.3: Classification Accuracies from Other Classifiers

### 2.5.5 Slope Feature with Different Numbers of Equi-divided Regions

In Section 2.4.2 while describing the slope feature, the number of equi-divided regions was not fixed. By classifying with various slope features extracted from QRS

complexes divided into different numbers of regions, the classification performance was evaluated.

| Number of Equi-divided Regions | Classification Accuracy |
|---|---|
| 6 | 79.62% |
| 9 | 80.38% |
| 12 | 80.35% |
| 15 | 80.32% |
| 18 | 80.14% |

Table 2.4: Classification Accuracies Using Slope Features with Different Numbers of Equi-divided Regions

The number of equi-divided regions can be interpreted as a resolution of the ECG signal. If the number of divisions is small, the signal slopes are roughly sampled, and the classification accuracy decreases. When the number of equi-divided regions is large, the slope feature extracted becomes closer to the original signal and will not perform as good as the slope feature. Out of 5 different numbers of divisions that we tested, 9 equi-divided region slope feature had the best classification result.

## 2.6 Conclusion and Future Research

The ECG as a 12-lead temporal signal is high dimensional and hard to comparatively analyze. We modeled (1) pace-map ECG signals to three dimensional coordinates for estimation and (2) ECGs to one dimensional region categories for their classification. By analyzing the signals with their known origins, we designed a new set of ECG features to use. We proved by experiments that the binary classification of epicardial and endocardial classification can perform with an accuracy of over 80% accuracy.

The present work sets the ground for future development regarding the distinction of VT origins based on the 12 lead ECG morphology. Further development of the concept of the universal heart is envisioned where certain ECG patterns (i.e. VT

morphologies) are anchored with precise coordinates corresponding to a cardiac ECG atlas that has region specific ECG patterns.

| Patient | Num of samples | Num of epi | Num of endo | Classification Accuracy (%) | PPV (%) | NPV (%) | Sensitivity (%) | Specificity (%) |
|---|---|---|---|---|---|---|---|---|
| 1 | 30 | 27 | 3 | 90.00 | 90.00 | NA | 100.00 | 0.00 |
| 2 | 87 | 54 | 33 | 86.21 | 88.89 | 81.82 | 88.89 | 81.82 |
| 3 | 193 | 105 | 88 | 67.36 | 65.44 | 71.93 | 84.76 | 46.59 |
| 4 | 95 | 88 | 7 | 80.00 | 91.57 | 0.00 | 86.36 | 0.00 |
| 5 | 64 | 41 | 23 | 84.38 | 86.05 | 80.95 | 90.24 | 73.91 |
| 6 | 140 | 84 | 56 | 70.00 | 80.88 | 59.72 | 65.48 | 76.79 |
| 7 | 143 | 70 | 73 | 71.33 | 85.37 | 65.69 | 50.00 | 91.78 |
| 8 | 52 | 45 | 7 | 86.54 | 86.54 | NA | 100.00 | 0.00 |
| 9 | 46 | 19 | 27 | 82.61 | 72.00 | 95.24 | 94.74 | 74.07 |
| 10 | 105 | 58 | 47 | 81.90 | 78.26 | 88.89 | 93.10 | 68.09 |
| 11 | 69 | 38 | 31 | 65.22 | 61.67 | 88.89 | 97.37 | 25.81 |
| 12 | 17 | 12 | 5 | 88.24 | 100.00 | 71.43 | 83.33 | 100.00 |
| 13 | 72 | 41 | 31 | 56.94 | 56.94 | NA | 100.00 | 0.00 |
| 14 | 94 | 48 | 46 | 51.06 | 51.06 | NA | 100.00 | 0.00 |
| 15 | 73 | 28 | 45 | 73.97 | 69.57 | 76.00 | 57.14 | 84.44 |
| 16 | 67 | 57 | 10 | 94.03 | 93.44 | 100.00 | 100.00 | 60.00 |
| 17 | 155 | 16 | 139 | 97.42 | 87.50 | 98.56 | 87.50 | 98.56 |
| 18 | 35 | 13 | 22 | 74.29 | 70.00 | 76.00 | 53.85 | 86.36 |
| 19 | 112 | 67 | 45 | 86.61 | 98.15 | 75.86 | 79.10 | 97.78 |
| 20 | 9 | 8 | 1 | 100.00 | 100.00 | 100.00 | 100.00 | 100.00 |
| 21 | 80 | 35 | 45 | 67.50 | 71.43 | 66.10 | 42.86 | 86.67 |
| 22 | 146 | 38 | 108 | 73.97 | NA | 73.97 | 0.00 | 100.00 |
| 23 | 5 | 3 | 2 | 100.00 | 100.00 | 100.00 | 100.00 | 100.00 |
| 24 | 79 | 63 | 16 | 88.61 | 88.57 | 88.89 | 98.41 | 50.00 |
| 25 | 87 | 58 | 29 | 89.66 | 91.53 | 85.71 | 93.10 | 82.76 |
| 26 | 18 | 9 | 9 | 100.00 | 100.00 | 100.00 | 100.00 | 100.00 |
| 27 | 50 | 48 | 2 | 100.00 | 100.00 | 100.00 | 100.00 | 100.00 |
| 28 | 145 | 69 | 76 | 84.83 | 97.96 | 78.12 | 69.57 | 98.68 |
| 29 | 117 | 59 | 58 | 82.05 | 83.93 | 80.33 | 79.66 | 84.48 |
| 30 | 107 | 31 | 76 | 79.44 | 76.47 | 80.00 | 41.94 | 94.74 |
| 31 | 116 | 76 | 40 | 90.52 | 89.16 | 93.94 | 97.37 | 77.50 |
| 32 | 120 | 34 | 86 | 91.67 | 87.50 | 93.18 | 82.35 | 95.35 |
| 33 | 112 | 37 | 75 | 68.75 | 100.00 | 68.18 | 5.41 | 100.00 |
| 34 | 29 | 20 | 9 | 89.66 | 94.74 | 80.00 | 90.00 | 88.89 |
| 35 | 227 | 124 | 103 | 78.41 | 76.98 | 80.68 | 86.29 | 68.93 |
| 36 | 26 | 2 | 24 | 92.31 | 50.00 | 100.00 | 100.00 | 91.67 |
| 37 | 43 | 7 | 36 | 97.67 | 100.00 | 97.30 | 85.71 | 100.00 |
| 38 | 4 | 2 | 2 | 100.00 | 100.00 | 100.00 | 100.00 | 100.00 |
| 39 | 9 | 5 | 4 | 100.00 | 100.00 | 100.00 | 100.00 | 100.00 |
| 40 | 29 | 2 | 27 | 96.55 | 66.67 | 100.00 | 100.00 | 96.30 |
| 41 | 10 | 8 | 2 | 80.00 | 80.00 | NA | 100.00 | 0.00 |
| 42 | 5 | 3 | 2 | 100.00 | 100.00 | 100.00 | 100.00 | 100.00 |
| 43 | 55 | 44 | 11 | 92.73 | 95.45 | 81.82 | 95.45 | 81.82 |
| total | 3277 | 1696 | 1581 | 84.48 | 84.85 | 83.66 | 83.26 | 73.58 |
| | | | sample average | 80.38 | | | 80.96 | 79.76 |

Table 2.5: All Pace-map Details and Epicardial vs. Endocardial Classification Results

# CHAPTER III

# Analysis of Electrocardiograms with Neural Network Algorithms

## 3.1 Introduction

One of the major goals of machine learning is teaching computers to learn from data as humans do. As an initial attempt in the early 1940s, people developed an algorithm that describes connections among the data similar to the interconnection of neurons in a brain. This algorithm was the beginning of the neural networks, learning the network structure among the data and outputs hidden (latent) patterns [52]. About a decade ago with a new breakthrough in the training technique of one of the neural networks, RBM, learning the networks in a hierarchy of multiple layers was introduced [53]. This model of multi-layer network is called deep learning, and it enables the machines to learn a rich connection between the data input layers and the final output layers. Thus, in various fields of applications, the performance using the output from deep learning is better than that obtained using other features. However, the success of deep learning hinges on matching the suitable learning algorithms to the application to ensure that computers learn meaningful elements.

One of the most studied applications using neural networks and deep learning is object recognition, proliferated in the 2000s [54]. At that time, deep learning

was applied to extract image features that perform better for recognition. In fact, classification using features extracted with deep learning algorithms proved to show higher accuracies than that of using raw images or image features in object recognition [55, 56]. However, while images and image features are spatial signals, there was almost no application to temporal signals.

The first attempt of applying neural networks to temporal data was for acoustic modeling in speech recognition. For many years, the state-of-the-art results in speech recognition were achieved by a combination of hidden Markov models (HMMs) with Gaussian mixture models (GMMs) [57]. In 2009, Lee et al. [58] started by applying deep belief networks (DBNs) to audio signals. By 2011, Mohamed et al. [59] introduced an innovational acoustic analysis model with outstanding speech recognition performances by transforming the temporal acoustic signals to Mel Frequency Cepstral Coefficients (MFCCs) in the frequency domain and using DBNs. In their subsequent paper, they also explain the theoretical reason DBNs perform better than other acoustic models presented before [60].

As explained in the previous chapter, electrocardiograms (ECGs) that we use are composed of multi-lead temporal signals. For classifying ventricular tachycardia (VT) origins of ECG signals, GMMs are the basic blocks in the model. However, GMMs are statistically insufficient when the data are distributed on a nonlinear manifold [57]. Moreover, due to the covariance matrix in the multivariate Gaussian distribution, learning the mixtures is computationally heavy. When the covariance matrix is diagonalized to reduce the computational load, which is applied to the experiments in Chapter II as well, GMMs represent the data distribution with an assumption that all data dimensions are uncorrelated.

As a solution to resolve these disadvantages of using GMMs, GMMs can be replaced with restricted Boltzmann machines (RBMs), which is a building block of deep belief network (DBN). In our previous paper, written with Sohn et al. [56], we

presented the equivalence between Gaussian mixtures and Gaussian-softmax RBM in order to use GMM as an initialization step of training RBM efficiently. This equivalence offers a possibility of replacing GMMs in the ECG analysis presented in Chapter II with RBMs and possibly to stack the RBMs to form a deep architecture.

This chapter is organized as follows. In Section 3.2, RBM and discriminative RBM is introduced as a background. The equivalence between GMM and RBM is mathematically shown in Section 3.3. As GMM is used as the classifier model in Chapter II, RBM is used as the classifier model in this chapter, and the application of RBMs to ECG signals and their learned weight matrices are presented in Section 3.4. In Section 3.5, the epicardial and endocardial classification results using RBM is discussed. Finally, the chapter is concluded in Section 3.6 with the mention about future work of using different neural networks and deep learning to ECGs.

## 3.2 Background

### 3.2.1 Restricted Boltzmann Machines

The restricted Boltzmann machine is a bipartite, undirected graphical model with visible (observed) and hidden (latent) units. The RBM can be understood as a Markov random field (MRF) with latent factors that explains the input visible data using binary latent variables. The RBM consists of visible data $\mathbf{v}$ of dimension $L$ that can take real values or binary values, and stochastic binary variables $\mathbf{h}$ of dimension $K$. The parameters of the model are the weight matrix $\mathbf{W} \in \mathbb{R}^{L \times K}$ that defines a potential between visible input variables and stochastic binary variables, the biases $\mathbf{c} \in \mathbb{R}^{L}$ for visible units, and the biases $\mathbf{b} \in \mathbb{R}^{K}$ for hidden units.

When the visible units are real-valued, the model is called the Gaussian RBM,

and its joint probability distribution can be defined as follows:

$$P(\mathbf{v}, \mathbf{h}) = \frac{1}{Z} \exp(-E(\mathbf{v}, \mathbf{h})), \tag{3.1}$$
$$E(\mathbf{v}, \mathbf{h}) = \frac{1}{2\sigma^2} \sum_i (v_i - c_i)^2 - \frac{1}{\sigma} \sum_{i,j} v_i W_{ij} h_j - \sum_j b_j h_j$$

where $Z$ is a normalization constant. The conditional distribution of this model can be written as follows:

$$P(h_j = 1|\mathbf{v}) = \text{sigm}(\frac{1}{\sigma} \sum_i W_{ij} v_i + b_j), \tag{3.2}$$

$$P(v_i|\mathbf{h}) = \mathcal{N}(v_i; \sigma \sum_j W_{ij} h_j + c_i, \sigma^2). \tag{3.3}$$

where $\text{sigm}(s) = \frac{1}{1+\exp(-s)}$ is the sigmoid function, and $\mathcal{N}(\cdot;\cdot,\cdot)$ is a Gaussian distribution. Here, the variables in a layer (given the other layers) are conditionally independent, and thus we can perform block Gibbs sampling in parallel.

### 3.2.2 Discriminative Restricted Boltzmann Machines

RBM and RBMs in deep architecture, called deep belief network (DBN), are commonly used to model the inputs of applications, thus the tasks benefit from expressive features learned. The joint distribution of the inputs and associated labels (classes) can be modeled, and the label can be predicted directly. This algorithm is called Discriminative restricted Boltzmann machines (dRBM) [61].

Discrimative RBM adds the label variable $y$ to the energy function, and correspondingly, a parameter defining the potential between label variables and the hidden variables, $\mathbf{U}$, is added. Therefore, the joint distribution is

$$P(y, \mathbf{v}, \mathbf{h}) \propto \exp(-E(y, \mathbf{v}, \mathbf{h})), \tag{3.4}$$

$$E(y, \mathbf{v}, \mathbf{h}) = -\sum_i c_i v_i - \sum_{i,j} v_i W_{ij} h_j - \sum_k d_k \vec{y}_k - \sum_{k,j} \vec{y}_k U_{kj} h_j - \sum_j b_j h_j \tag{3.5}$$

,and ($\mathbf{W}$, $\mathbf{U}$, $\mathbf{b}$, $\mathbf{c}$, $\mathbf{d}$) are the parameters and $\vec{y}$ is the class indicator vector of the label $y$. From this joint distribution function, the conditional distributions can be derived.

$$P(\mathbf{v}|\mathbf{h}) = \prod_i p(v_i|\mathbf{h}) \tag{3.6}$$

$$P(v_i = 1|\mathbf{h}) = \text{sigm}(\sum_j W_{ji} h_j + c_j) \tag{3.7}$$

$$P(y|\mathbf{h}) = \frac{\exp(\sum_j U_{jy} h_j + d_y)}{\sum_k \exp(\sum_j U_{jk} h_j + d_k)} \tag{3.8}$$

$$P(\mathbf{h}|y, \mathbf{v}) = \prod_j p(h_j|y, \mathbf{v}) \tag{3.9}$$

$$P(h_j = 1|y, \mathbf{v}) = \text{sigm}(\sum_i W_{ij} v_i + U_{jk} + c_j) \tag{3.10}$$

This dRBM model is simply described in Figure 3.1 as a diagram. It is trained using contrastive divergence similar to how RBM is trained. In terms of applying to classification tasks, a hybrid training model is used since generative training is less dependent on the number of samples. The gradient of log likelihood is optimized both in discriminative and generative training [61].

As a classifier, the distribution between the input $\mathbf{v}$ and the label $y$ has to be computed. While $P(y, \mathbf{v})$ is intractable, the conditional distribution $P(y|\mathbf{v})$ is exactly computable.

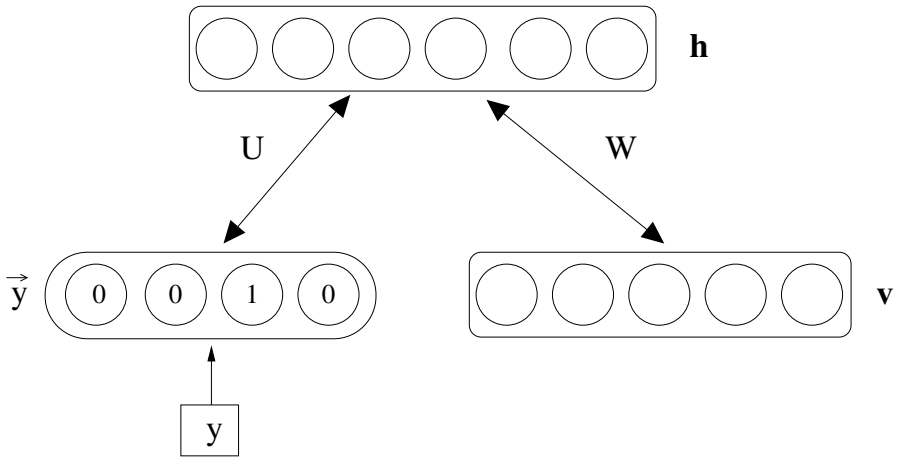


Figure 3.1: Restricted Boltzmann Machine Modeling the Joint Distribution of Inputs and Target Labels. Reprinted from "Classification using Discriminative Restricted Boltzmann Machines" by H. Larochelle and Y. Bengio, ICML 2008.

$$P(y|\mathbf{v}) = \frac{exp(d_y)\prod_{j=1}^{n}(1+exp(\sum_i W_{ij}v_i + U_{jy} + c_j))}{\sum_k exp(d_k)\prod_{j=1}^{n}(1+exp(\sum_i W_{ij}v_i + U_{jk} + c_j))} \tag{3.11}$$

## 3.3 Equivalence between mixture models and RBMs with a softmax constraint

This section was initially addressed to provide a novel training algorithm for RBMs by exploiting the relationship between clustering methods and RBMs since training RBM is know to be difficult. We show that a Gaussian RBM with softmax hidden units can be converted into a Gaussian mixture model, and vice versa. This connection between mixture models and RBMs with a softmax constraint completes the chain of links between K-means, GMMs, Gaussian-softmax RBMs, and sparse RBMs. This chain of links motivate an efficient training method for sparse RBMs.

### 3.3.1 Gaussian mixture models

As in Chapter II, the likelihood of a GMM with $K+1$ Gaussians can be written as follows:

$$P(\mathbf{v}) = \sum_{k=0}^{K} \pi_k \mathcal{N}(\mathbf{v}; \boldsymbol{\mu}_k, \boldsymbol{\Sigma}_k) \tag{3.12}$$

For the rest of the chapter, we denote the GMM with shared spherical covariance as GMM($\boldsymbol{\mu}_k, \sigma^2\mathbf{I}$), when $\boldsymbol{\Sigma}_k = \sigma^2\mathbf{I}$ for all $k \in \{0, 1, \ldots, K\}$. For the GMM with arbitrary positive definite covariance matrices, we will use the shorthand notation GMM($\boldsymbol{\mu}_k, \boldsymbol{\Sigma}_k$).

### 3.3.2 Gaussian-softmax RBMs

We define the Gaussian-softmax RBM as the Gaussian RBM with a constraint that at most one hidden unit can be activated at a time given the input, i.e., $\sum_j h_j \leq 1$. The energy function of the Gaussian-softmax RBM can be written in a vectorized form as follows:

$$\begin{aligned} E(\mathbf{v}, \mathbf{h}) &= \frac{1}{2\sigma^2}||\mathbf{v} - \mathbf{c}||^2 - \frac{1}{\sigma}\mathbf{v}^T\mathbf{W}\mathbf{h} - \mathbf{b}^T\mathbf{h} \\ \text{subj. to} \quad & \sum_j h_j \leq 1 \end{aligned} \tag{3.13}$$

For this model, the conditional probabilities of visible or hidden units given the other layer can be computed as:

$$P(\mathbf{v}|\mathbf{h}) = \mathcal{N}(\mathbf{v}; \sigma\mathbf{W}\mathbf{h} + \mathbf{c}, \sigma^2\mathbf{I}) \tag{3.14}$$

$$P(h_j = 1|\mathbf{v}) = \frac{\exp(\frac{1}{\sigma}\mathbf{w}_j^T\mathbf{v} + b_j)}{1 + \sum_{j'} \exp(\frac{1}{\sigma}\mathbf{w}_{j'}^T\mathbf{v} + b_{j'})}, \tag{3.15}$$

where $\mathbf{w}_j$ is the $j$-th column of the $\mathbf{W}$ matrix, often denoted as a "basis" vector for the $j$-th hidden unit. In this model, there are $K+1$ possible configurations (i.e., all hidden units are 0, or only one hidden unit $h_j$ is 1 for some $j$).

### 3.3.3 Equivalence between Gaussian mixtures and Gaussian-softmax RBMs

As Equation 3.14 shows, the conditional probability of visible units given the hidden unit activations for Gaussian-softmax RBM follows a Gaussian distribution. From this perspective, the Gaussian-softmax RBM can be viewed as a mixture of Gaussians whose mean components correspond to possible hidden unit configurations.[1] In this section, we show an explicit equivalence between these two models by formulating the conversion equations between GMM($\boldsymbol{\mu}_k, \sigma^2\mathbf{I}$) with $K+1$ Gaussian components and the Gaussian-softmax RBM with $K$ hidden units.

**Proposition III.1.** *The mixture of $K+1$ Gaussians with shared spherical covariance of $\sigma^2\mathbf{I}$ is equivalent to the Gaussian-softmax RBM with $K$ hidden units.*

*Proof.* We prove by constructing the following conversions.

**(1) From Gaussian-softmax RBM to GMM($\boldsymbol{\mu}_k, \sigma^2\mathbf{I}$):**

We begin by the decomposition using a chain rule:

$$P(\mathbf{v}, \mathbf{h}) = P(\mathbf{v}|\mathbf{h})P(\mathbf{h}),$$

where

$$P(\mathbf{h}) = \frac{1}{Z}\int d\mathbf{v}\exp(-E(\mathbf{v}, \mathbf{h})).$$

Since there are only a finite number of hidden unit configurations, we can explicitly enumerate the prior probabilities:

$$P(h_j = 1) = \frac{\int d\mathbf{v}\exp(-E(\mathbf{v}, h_j = 1))}{\sum_{j'}\int d\mathbf{v}\exp(-E(\mathbf{v}, h_{j'} = 1))}$$

If we define $\tilde{\pi}_j = \int d\mathbf{v}\exp(-E(\mathbf{v}, h_j = 1))$, then we have $P(h_j = 1) = \frac{\tilde{\pi}_j}{\sum_{j'}\tilde{\pi}_{j'}} \triangleq \pi_j$.

[1] In fact, the Gaussian RBM (without any constraints) can be viewed as a mixture of Gaussians with an exponential number of components. However, it is nontrivial to use this notion itself to develop a useful algorithm.

In fact, $\tilde{\pi}_j$ can be analytically calculated as follows:

$$\begin{aligned}\tilde{\pi}_j &= \int d\mathbf{v} \exp(-E(\mathbf{v}, h_j = 1)) \\ &= \int d\mathbf{v} \exp(-\frac{1}{2\sigma^2}||\mathbf{v} - \mathbf{c}||^2 + \frac{1}{\sigma}\mathbf{v}^T\mathbf{w}_j + b_j) \\ &= (\sqrt{2\pi}\sigma)^L \exp(b_j + \frac{1}{2}||\mathbf{w}_j||^2 + \frac{1}{\sigma}\mathbf{c}^T\mathbf{w}_j)\end{aligned}$$

Using this definition, we can show the following equality:

$$P(\mathbf{v}) = \sum_j \pi_j \mathcal{N}(\mathbf{v}; \sigma\mathbf{w}_j + \mathbf{c}, \sigma^2\mathbf{I}).$$

**(2) From GMM($\boldsymbol{\mu}_k, \sigma^2\mathbf{I}$) to Gaussian-softmax RBM:**

We will also show this by construction. Suppose we have the following Gaussian mixture with $K + 1$ components and the shared spherical covariance $\sigma^2\mathbf{I}$:

$$P(\mathbf{v}) = \sum_{j=0}^{K} \pi_j \mathcal{N}(\mathbf{v}; \boldsymbol{\mu}_j, \sigma^2\mathbf{I}). \tag{3.16}$$

We can convert from this GMM($\boldsymbol{\mu}_k, \sigma^2\mathbf{I}$) to a Gaussian-softmax RBM using the following transformations:

$$\mathbf{c} = \boldsymbol{\mu}_0 \tag{3.17}$$

$$\mathbf{w}_j = \frac{1}{\sigma}(\boldsymbol{\mu}_j - \mathbf{c}), j = 1, ..., K \tag{3.18}$$

$$b_j = \log\frac{\pi_j}{\pi_0} - \frac{1}{2}||\mathbf{w}_j||^2 - \frac{1}{\sigma}\mathbf{w}_j^T\mathbf{c}. \tag{3.19}$$

It is easy to see that the conditional distribution $P(\mathbf{v}|h_j = 1)$ can be formulated as a Gaussian distribution with mean $\boldsymbol{\mu}_j = \sigma\mathbf{w}_j + \mathbf{c}$, which is identical to that of the Gaussian-softmax RBM. Further, we can recover the posterior probability of hidden

units given the visible units as follows:

$$P(h_j = 1|\mathbf{v}) = \frac{\pi_j \exp(-\frac{1}{2\sigma^2}||\mathbf{v} - \sigma\mathbf{w}_j - \mathbf{c}||^2)}{\sum_{j'=0}^{K} \pi_{j'} \exp(-\frac{1}{2\sigma^2}||\mathbf{v} - \sigma\mathbf{w}_{j'} - \mathbf{c}||^2)}$$
$$= \frac{\exp(\frac{1}{\sigma}\mathbf{w}_j^T\mathbf{v} + b_j)}{1 + \sum_{j'=1}^{K} \exp(\frac{1}{\sigma}\mathbf{w}_{j'}^T\mathbf{v} + b_j)}$$

Therefore, a Gaussian mixture can be converted to an equivalent Gaussian RBM with a softmax constraint. □

Similarly, the Gaussian mixture with shared diagonal covariance is equivalent to the Gaussian-softmax RBM with a slightly more general energy function, where each visible unit $v_i$ has its own noise parameter $\sigma_i$, as stated below.

**Corollary III.2.** *The mixture of $K+1$ Gaussians with a shared diagonal covariance matrix (with diagonal entries $\sigma_i^2, i = 1, ..., L$) is equivalent to the Gaussian-softmax RBM with the following energy function: $E(\mathbf{v}, \mathbf{h}) = \sum_i \frac{1}{2\sigma_i^2}(v_i - c_i)^2 - \sum_{i,j} \frac{1}{\sigma_i} v_i W_{ij} h_j - \sum_j b_j h_j$.*

Further, the equivalence between mixture models and RBMs can be shown for other settings. For example, the following corollaries can be derived from Proposition III.1.

**Corollary III.3.** *The binary RBM (i.e., when the visible units are binary) with a softmax constraint on hidden units and the mixture of Bernoulli models are equivalent.*

**Corollary III.4.** *GMM($\mathbf{0}, \mathbf{\Sigma}_k$) with arbitrary covariance matrices and the factored 3-way RBM [62] with a softmax constraint on hidden units are equivalent.*

### 3.3.4 Implication

Proposition III.1 has important ramifications. First, it is well known that K-means can be viewed as an approximation of a GMM with spherical covariance by

letting $\sigma \to 0$ [63]. Compared to GMMs, the training of K-means is highly efficient; therefore, it is plausible to train K-means to provide an initialization of a GMM.[2] Then, the GMM is trained with EM, and we can convert it to an RBM with softmax units. This can provide an efficient initialization for training sparse RBMs.

## 3.4 Application of RBM to Electrocardiograms

Following from Chapter II, the objective is to classify the ventricular tachycardia and pace-map origins to either epicardial or endocardial by analyzing their ECG signals. In Chapter II, ECG signals were decomposed using sparse LDA, and through that analysis, the slopes in equidivided time ranges were found to have high discriminating values. Having these slopes as the input ECG feature, the likelihood distribution between the inputs and their corresponding origin classes was learned. GMM was used as the trainable distribution model, and the classification results using that GMM likelihood distribution were reliable.

In the previous section, the equivalence between GMM and Gaussian softmax RBM has been proven. This indicated a possibility of designing an epicardial versus endocardial classifier with RBM instead of GMM. RBM has a comprehensive network between the input layer and the hidden layer, and can therefore be thought of as more expressive than GMM. Also, neural networks, such as RBM, can be stacked into multiple layers, learning latent information in hierarchies that might give a refined interpretation of the input data.

In this section, pace-map ECGs were learned with the discriminative RBM, introduced in Section 3.2. In a classification problem, the distribution of labels given input signals must be calculated, and the discriminative RBM estimates this distribution by having both the signals and its corresponding labels as inputs. While learning the

[2]K-means learn cluster centroids and provides hard-assignment of training examples to the cluster centroids (i.e., each example is assigned to one centroid). This hard-assignment can be used to initialize GMM's parameters, such as $\pi_k$ and $\sigma$, by running one M-step in the EM algorithm.

pace-maps with the discriminative RBM, the change in weight matrices depending on the number of hidden layers was examined. We observed that the number of hidden units influences the accuracy of the discriminative RBM training performance. Here, for the purpose of variable selection, a discriminative RBM on each of the 12 ECG lead signals was trained separately.

### 3.4.1 RBM and the Number of Hidden Units

Training an RBM model requires control of numerous meta-parameters. Some parameters are related to the process of training iterations, such as the learning rate, the momentum, and the weight-cost. Some other parameters are set to target the desired model specifications, such as the sparsity value and the number of hidden units. Since Proposition III.1 in Section 3.3.3 states that the number of hidden units in RBM corresponds to the number of mixtures in GMM while showing the equivalence between GMM and Gaussian softmax RBM, RBM trained on the pace-map ECG dataset with different numbers of hidden units are examined in this section.

Following from the intuition of a mixture model, the number of hidden units can be interpreted as the maximum possible number of components to learn a good explanatory model for a given training dataset. As the complexity of a dataset increases, the number of required components to describe the data grows as well. The paper by Le Roux et al. [64] proved that an RBM with a larger number of hidden units is guaranteed to better describe the likelihood function, while simultaneously defining the representational power of RBM and deep belief network. In order words, having more numbers of hidden units guarantees to describe the input dataset better.

The change in the weight bases of the RBM according to different numbers of hidden units was investigated with the pace-map ECG dataset used in Chapter II. The 3277 pace-map ECGs were used to train discriminative RBMs at given numbers of hidden units. According to the RBM training guide written by Hinton [65], a good

recipe for choosing a number of hidden units is to multiply the number of bits needed to describe each input vector (estimated by negative $log_2$ of $p(\mathbf{v})$) by the number of training samples, and reduce the result by an order of magnitude. For the pace-map ECG dataset, the number of hidden units following Hinton's recipe varied from 200 to 400. However, a full sequence of numbers of hidden units was chosen to show the changes in RBM training, starting from 25 hidden units to 500 hidden units. For illustration purposes, we restricted the analysis in this section to a single lead ECG signal from lead V5.

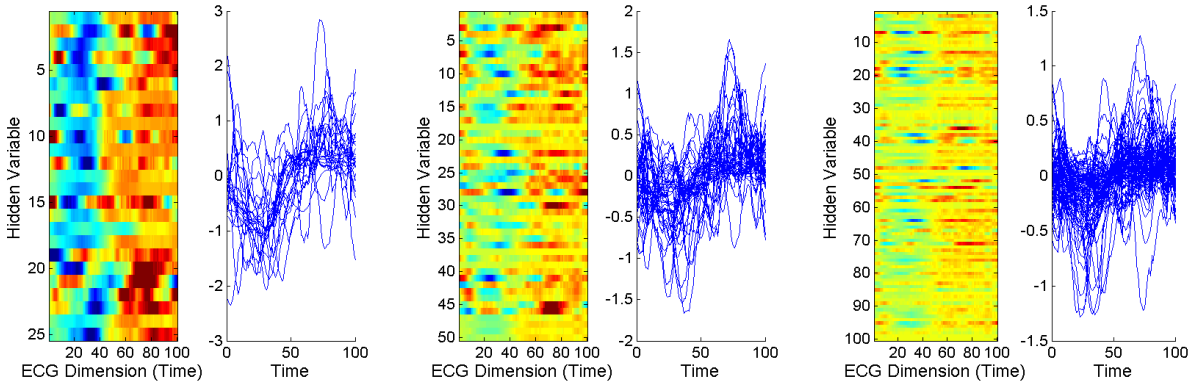


(a) 25 Hidden Layers (b) 50 Hidden Layers (c) 100 Hidden Layers

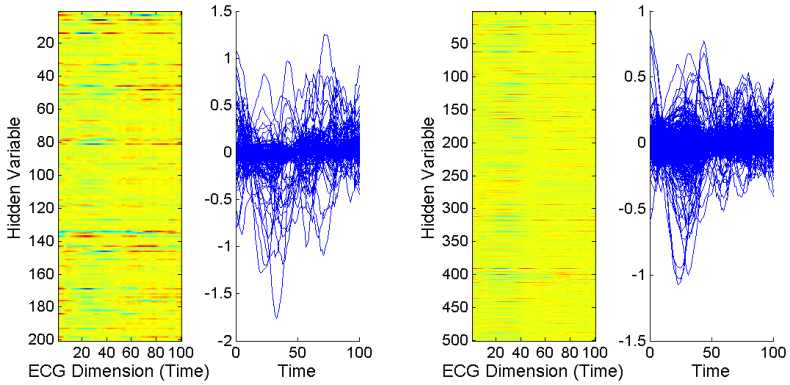


(d) 200 Hidden Layers (e) 500 Hidden Layers

Figure 3.2: Weight Matrix Visualizations for Different Numbers of Hidden Units. The size of an RBM weight matrix is the dimension of the input by the number of hidden units. For each subfigure, the left image is the learned weight matrix (transposed), and the right plot is the column vectors of the weight matrix overlapped to a single plot. In the image of the weight matrix, blue indicates negative values, red indicates positive values, and the color close to yellow and green indicates the values near zero.

Figure 3.2 presents the learned weight matrices with the different numbers of hidden units. The column vectors of an RBM weight matrix represent the weight bases, and thus the number of columns is the number of hidden units assigned. For each subfigure with a given number of hidden units, the left images show the transposed weight matrix: blue indicates negative values, red indicates positive values, and the color close to yellow and green indicates the values near zero. The plots in the right sides are overlappings of each column vectors (signals) of the weight matrix. Therefore, a left image and a right plot in each subfigure represent the same weight matrix in two different ways.

When the signal of ECG lead V5 was trained with 25 hidden units, presented in Figure 3.2a, an apparent trend in weight bases was observed. It took negative weights in the first half of the signal and gave more positive weights in the second half, which created a sigmoid-function-like shape. As the numbers of hidden units increased to 50 and 100, the importance of the negative values in the first half and the positive values in the second half was still observable, but there were additions of noisy near-zero bases. As the numbers of hidden units were increased to 200 and 500, the weight matrix image in the right side presented the trend better than the weight signal plot in the left side. There were more blues (negative values) in the first half of the weight matrices, and some reds (positive values) in the second half, that followed the trend in weight matrices with lower numbers of hidden units.

When we observed the changes in plots from 25 hidden units to 500 hidden units, the bases with 25 hidden units looked rough; however, 500 hidden units looked redundantly dense. This redundancy may imply a property of the pace-map ECG dataset. The classification performance according to the different numbers of hidden units will be discussed with the results in Section 3.5.

### 3.4.2 RBM with ECG Signals from Each Lead

An 12-lead ECG consists of twelve time series signals. Although all twelve signals are originated and collected from a single patient's heart, the signals from each lead represent different aspects of a heart rhythm. This, in other words, means that signals from some leads can have more relevant information to the classification objective, and some might contain less relevant information. By training discriminative RBM with signals from each lead separately, the relevance of each lead to the epicardial and endocardial classification was analyzed.

In Chapter II, each patient's pace-maps were learned with sparse LDA to analyze the components of the ECG signals having more importance to the epicardial and endocardial classification. For the analysis in this chapter, each lead's signals were learned with discriminative RBM, and the trained weight matrices were visualized. From the RBM notations used in the previous sections, $\mathbf{W}$ is the weight matrix between the input ECG layer and the hidden layer. The column is the dimension of the ECG time sequence, and the row is the samples of the hidden layer. Therefore, each row vector represents a time series signal basis.

Each discriminative RBM was trained with 500 hidden layers, and the weights were presented in Figure 3.3. The differences in the weight matrices trained with each lead signal as an input were apparently observed. The weights can be categorized to different types. Some of the leads had dynamic variances in the particular time ranges of the signal, such as in lead I, II, V4, and V5. These leads showed dynamic weight in the first one third of the time range (Figure 3.5 at the end of the chapter). Leads like aVF, V2, and V3 had highly activated bases and numerous other bases without high amplitude values. Among the bases without high amplitudes, some periodicities were observable (Figure 3.6). There were leads with no trends in weight. Lead aVR and aVL had dynamic spreads over the whole range (Figure 3.7).

The classification performance using each one of these trained discriminative RBM

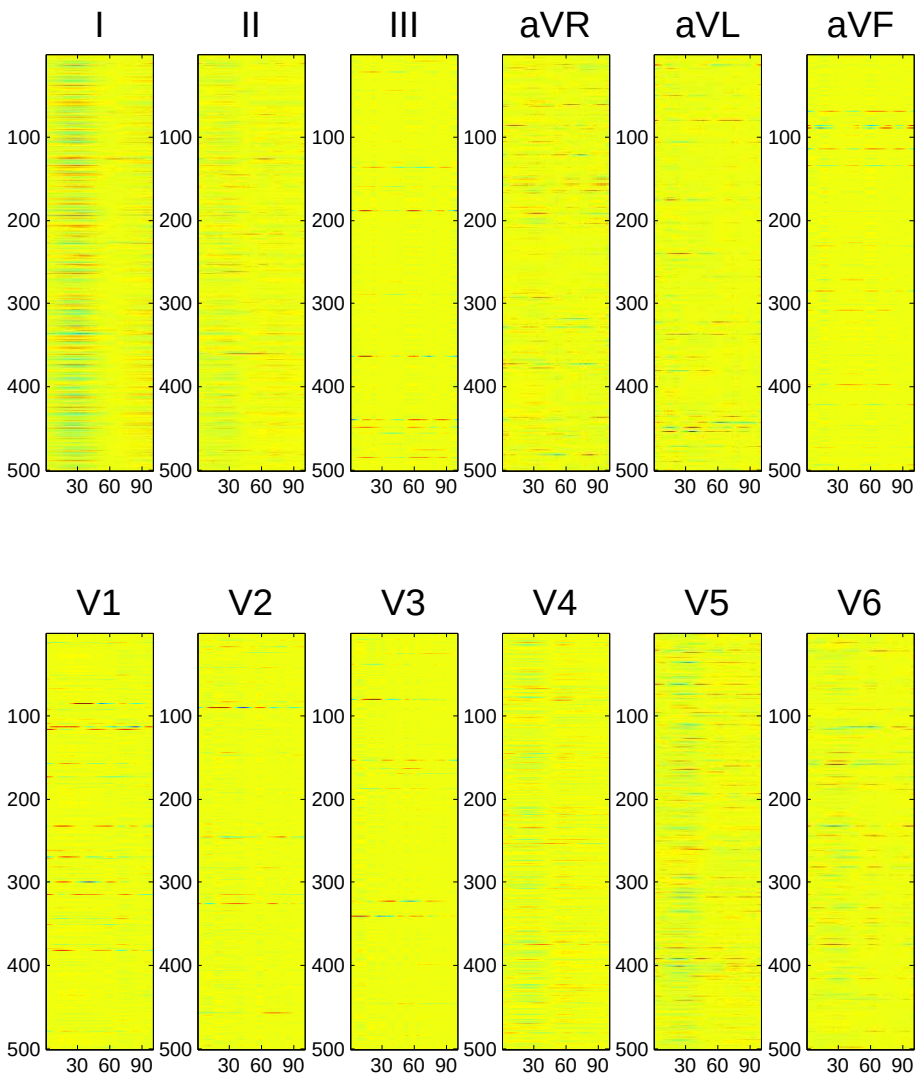


Figure 3.3: Weight Matrices Trained with Single Lead ECG Signals: All leads. All images of the weight matrices are set to the same color scale for a fair comparison among them: blue indicates negative values, red indicates positive values, and the color between yellow and green is corresponding to the values near zero. This figure is best viewed in color.

was examined. A binary epicardial and endocardial classification for pace-map sites of origins was performed. The classifiers train by different ECG lead signals resulted in classification accuracies ranging from 54% to 76%.

Lead V1, V2, and V3 were the leads underperforming in this classification. Especially, lead V2 had a very low classification rate, close to random guessing in binary classification (54.3%). These leads were the ones that had two or three high ampli-

tude bases with many low periodic bases, presented in Figure 3.6. The periodicity over the range of time was because RBM cannot find good class separating bases. High classification accuracies appeared in the leads with define trends in the bases. The weigh matrices trained with Lead I, V4, V5, and V6 had dynamic amplitude variances concentrated in the beginning and the end of the time range as shown in Figure 3.5, and classifiers trained with those leads outperform those of other leads.

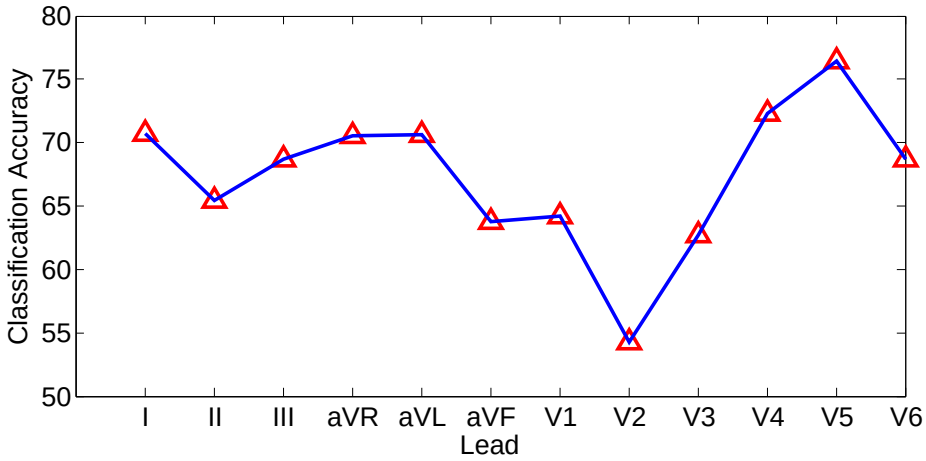


Figure 3.4: Epicardial and Endocardial Classification Accuracy by Discriminative RBM with ECG Signals from Each Lead

## 3.5 Results and Discussion

The experimental setting for the classification of epicardial and endocardial origins of 3277 pace-maps was exactly identical to that of Chapter II. The pace-maps were divided into 43 sets according to their belonging patients. The training and testing of the classification was performed 43 times, using one patient's pace-maps as a testing set and the remaining pace-maps as a training set for each time (leave-one-patient-out). The average classification accuracy over theses 43 runs was reported.

The overall classification accuracy between epicardial and endocardial pace-map ECGs using discriminative RBM was 79.12% over all patients. We know that the representational power of RBM is greater than that of GMM. However, with discrim-

inative RBM as the classifier, both the raw ECGs and the slope feature from Chapter II were not enough to reach over 80% accuracy. This result inspired the use of hybrid discriminative RBM, which is a mixed training of discriminative and generative RBM, and deep learning networks for more detailed classifier.

The best result of 79.12% was achieved with 100 hidden units. The epicardial and endocardial classification accuracy increased as the number of hidden units increases up to 100. However, in numerous trials, the classification accuracies were lower for the number of hidden units over 100. Especially, the biggest drop in performance happened as the hidden units increase from 100 to 200. Although more hidden units guaranteed improvements in achieving distributions according to Le Roux et al. [64] as mentioned in Section 3.4.1, the 3277 pace-maps used for this classification problem probably can be described with around 100 bases. It can be interpreted as the weight bases becoming redundant and noisy as the number of hidden units is targeted to be over 100.

| Number of Hidden Units | Classification Accuracy |
|---|---|
| 25 | 78.65% |
| 50 | 78.76% |
| 100 | 79.12% |
| 200 | 78.18% |
| 500 | 77.47% |
| 1000 | 77.18% |

Table 3.1: Classification Accuracies Using Discriminative RBM with Different Numbers of Hidden Units

## 3.6 Conclusion and Future Research

Restricted Boltzmann machine has been widely used in numerous applications with superior performances. As an effort to apply the RBM to ECGs in this chapter, a mathematical equivalence between mixture model and RBM is established, and based on that connection, a RBM classifier is designed following from the GMM classifier

presented in the previous chapter. Epicardial and Endocardial ECG classificaiton with discriminative RBM did not outperform the classification with GMM. However, the trained weight matrices are analyzed to visually interpret the information learned from the ECG signals.

There is a broad range of future work to be done with applying RBM and, moreover, neural networks to ECGs. First, extensions of discriminative RBMs can be used to train the classifier. Using a combination of discriminative and generative RBM trainings, called hybrid discriminative RBM, and applying sparsity constraint to the RBMs (sparse RBM) are the two most possible extensions to enhance the classifier and classification results. By approaching the problem with a more generative perspective, we can attempt to learn the ECGs using unsupervised feature learning. This will create a new representation of ECGs and advance the ECG feature sets. Generally, this unsupervised feature learning problem can be extended to learning the features from low-frequency, time-series signals.

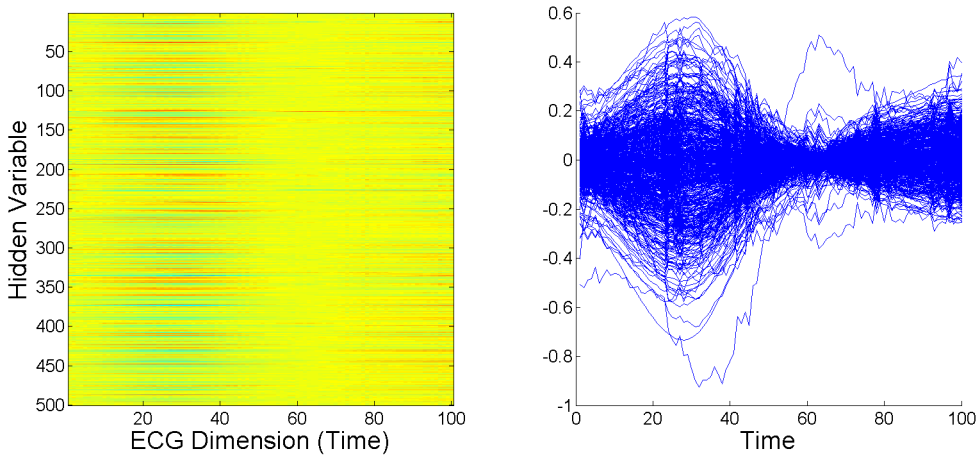


(a) Lead I

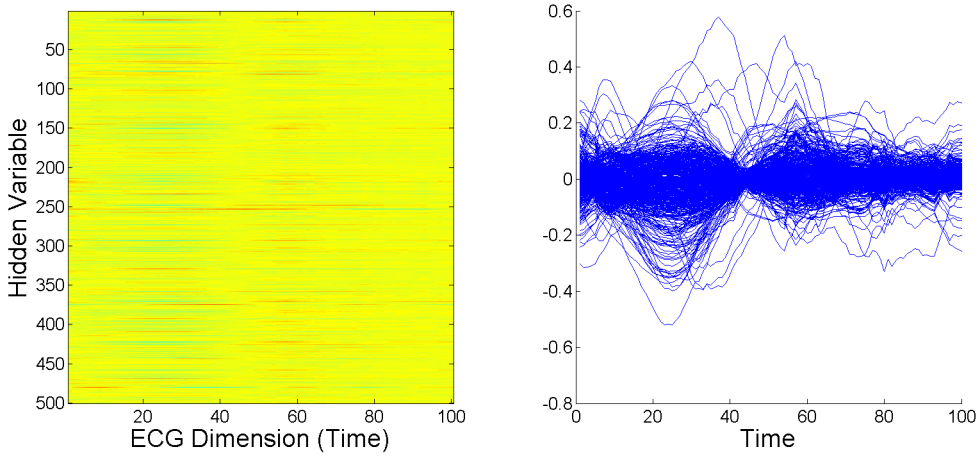


(b) Lead V4

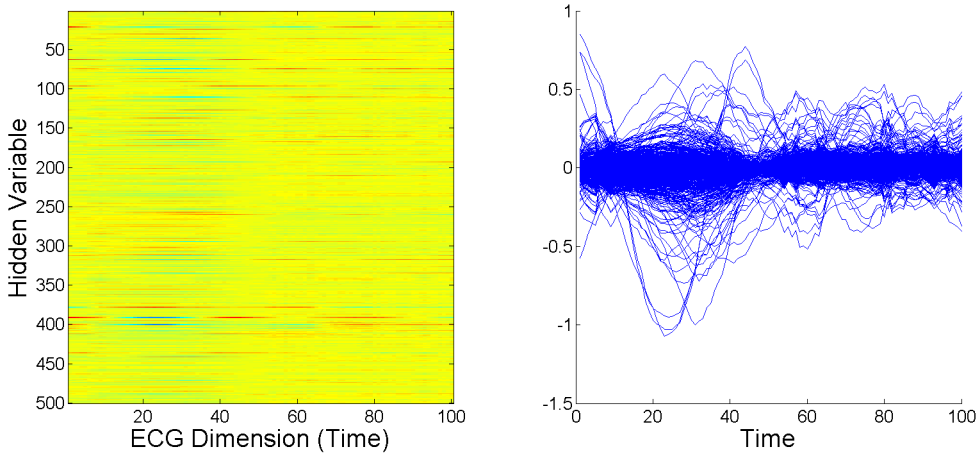


(c) Lead V5

Figure 3.5: Weight Matrices Trained with Single Lead ECG Signals: Lead I, V4, and V5. The weight matrices are from discriminative RBM trained with 500 Hidden Units. The weight concentrated in the starting time range is observable with these three leads.

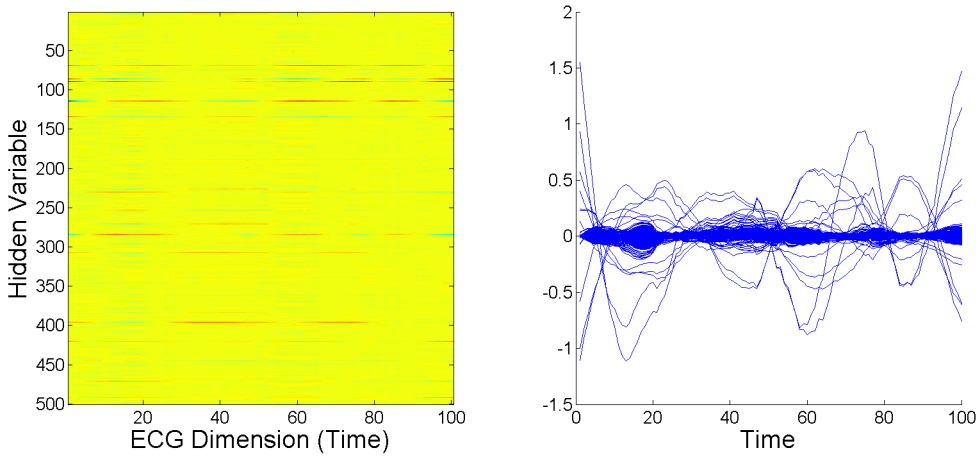


(a) Lead aVF

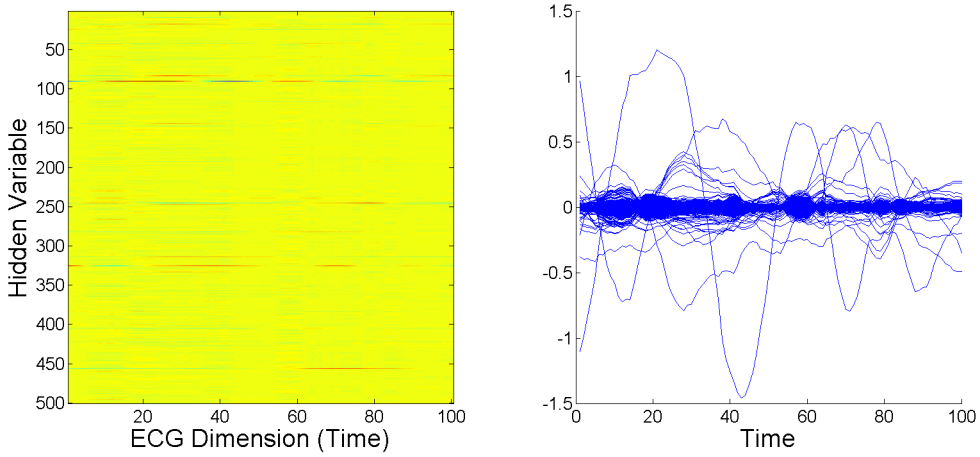


(b) Lead V2

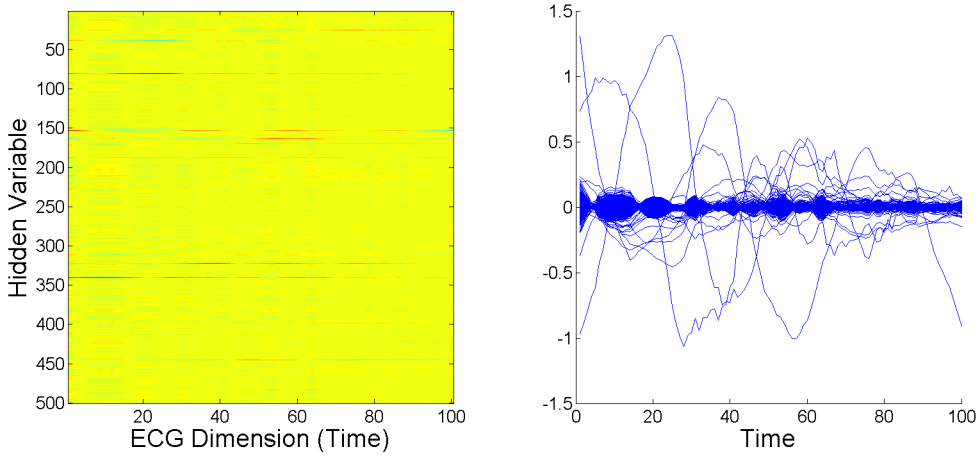


(c) Lead V3

Figure 3.6: Weight Matrices Trained with Single Lead ECG Signals: Lead aVF, V2, and V3. The weight matrices are from discriminative RBM trained with 500 Hidden Units. High-amplitude bases and periodics bases are observable in these leads.

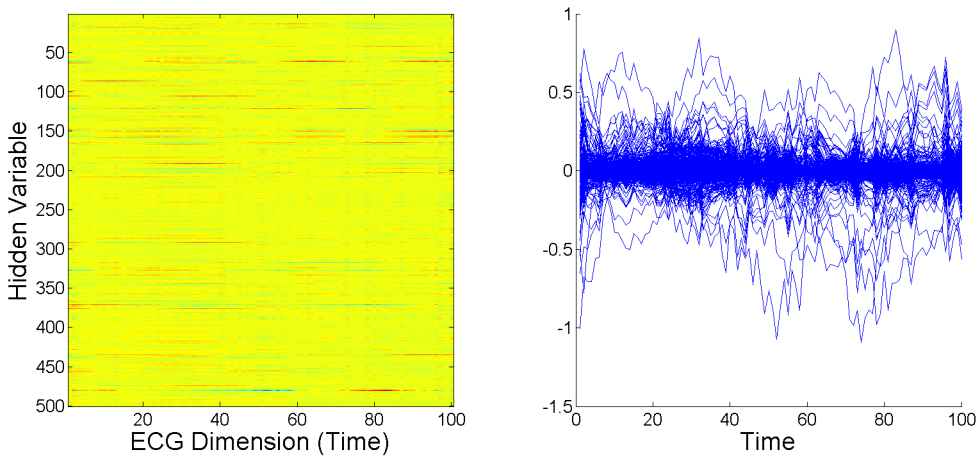


(a) Lead aVR

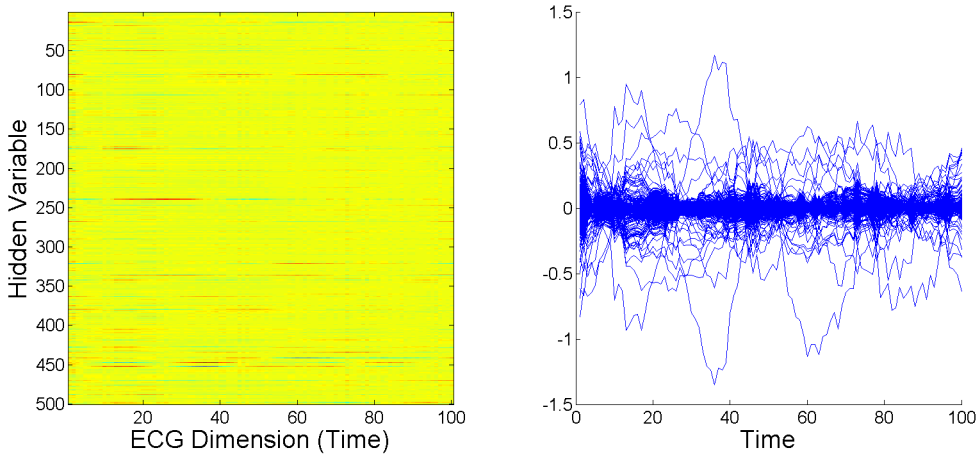


(b) Lead aVL

Figure 3.7: Weight Matrices Trained with Single Lead ECG Signals: Lead aVR and aVL. The weight matrices are from discriminative RBM trained with 500 Hidden Units. Signals from these leads learned noisy bases with no particular trends.

# CHAPTER IV

# Quaternion Laplacian Information Maps for Dimensionality Reduction and Its Application to Analysis of Electrocardiograms

## 4.1 Introduction

Extracting a meaningful representation (or a feature) from high dimensional data has been a challenge for decades. [54, 66, 67, 68] One of the heavily studied methods for finding a meaningful representation is manifold learning, which involves embedding characteristic properties of the original high-dimensional data into a lower dimension, Riemannian manifold [54, 69, 70]. Until recently, the distinctions of various manifold learning methods come from (1) the measurement of proximity among the original data points and (2) the embedding optimization.

A new approach to manifold learning adds an element of a priori knowledge that there exists a low-dimensional Riemannian manifold embedded in the data. With our a priori knowledge of the manifold, embedded points expose the desired latent information from original data. For example, when images of an object from different angles are embedded into the surface of a sphere, the embedding represents those changes in angle. This approach was originally presented with a method called Spherical Laplacian Information Maps (SLIM) [71]. SLIM uses a priori knowledge

and reconstructs a statistical manifold with a constraint that embedded points must lie on the surface of a three dimensional sphere, 2-sphere ($S^2$).

In this paper, we present an improved method called Quaternion Laplacian Information Maps (QLIM), which constrains the embedding manifold to be a quaternion space instead of a three-dimensional sphere. A quaternion is a four-dimensional number that can fully describe the rotations in three-dimensional Euclidean space, $SO(3)$. In terms of its geometry, a unit quaternion lies on a four-dimensional sphere, called 3-sphere ($S^3$). By extending a 2-sphere embedding in SLIM to a quaternion embedding with QLIM, which is still interpretable, we introduce the benefits of this manifold dimension extension for applications in electrocardiogram (ECG) analysis and camera angle estimation.

The remainder of the chapter proceeds as follows. In Section 4.2.1, an overview of previous manifold learning methods and a brief background to unit quaternions and a geodesic distance measure among quaternion points are presented. Section 4.3 illustrates the methodology of Quaternion Laplacian Information Maps, and its application to different data is shown in Section 4.4. Finally, we conclude and present future directions in Section 4.5.

## 4.2 Background

### 4.2.1 Related Work

More than a decade ago, many dimensionality reduction methods were newly presented in order to enhance the previous methods such as principle component analysis (PCA) or classical multidimensional scaling (MDS). PCA and MDS have difficulties in finding the nonlinear structures contained in high dimensional data. For example, if the data is existing in a curved space, two point which are laying very closely in the Euclidean structure can be very far following their embedding curved

space. Concerning these hidden low dimensional structures, Tenenbaum et al. [66] introduced the method called isometric feature mapping, or Isomap. Isomap first defines the neighborhood graph, which indicates only the data points that are near each point. Either k-nearest neighborhood or the distance threshold ($|x_i - x_j| < \varepsilon$) can be used to limit the near by points. From this neighborhood graph, the geodesic distance is measured to be used as the weight among the neighboring points. The selection of the metric in this step is important for the low dimensional embedding output. Finally MDS is applied to the distance matrix from the previous step to find the new embedding. This flow of dimensional reduction steps became very standard from the introduction of this method, Isomap.

In the same period, similar reduction method called locally linear embedding (LLE) is shown by Roweis et al. [72]. The motivation and aim of the method is the same as that of Isomap: reduce the dimension to find the best neighborhood-preserving embedding. The first step of finding the neighboring points in the high dimensional space is the same. However in the second step, LLE creates a reconstruction matrix, which reconstructs the data points from all the neighboring points. Having this reconstruction matrix, it reconstructs the low dimension embeddings with the goal of minimal reconstruction error. LLE basically adopted the idea of reducing the reconstruction error, which is a basis in most learning methods.

The difference between Isomap and LLE is mentioned in the paper by Silva et al. [73]. LLE only preserves the local geometry of the data. It maps the nearby point in the high dimensional space to the nearby points in the low dimensional space. However, Isomap preserves the global geometry of the data: embedding nearby points to nearby and far away point to far away from the original data to the low dimensional embedding.

Spherical Laplacian Information Maps (SLIM) by Carter et al. [71] is a combined dimensional reduction method of two different methods: Laplacian eigenmaps by

Belkin et al. [74] and Fisher Information Non-parametric Embedding (FINE) by Carter et al. [75]. Laplacian eigenmaps is unique in its setting of the transformation. Just like Isomap and LLE, it starts with setting the nearest neighbor graph. With this graph, the weight between each neighboring points is assigned using Gaussian kernel (or heat kernel), which is exponentially decaying as the distance between two points grows. Using this weight matrix, the embedding objective function is set intuitively, larger the weight closer the embedding, and this objective function is derived to be an equation involving Laplacian matrix.

Fisher Information Nonparametric Embedding (FINE) [75] involves a new concept to the dimensional reduction methodologies. Instead of calculating the distance between each data points using some metrics, FINE realizes each data as a distribution on a statistical manifold, and computes the distance between each data point's distribution using Fisher information distance. After constructing this distance matrix, the rest of the steps is similar to Isomap, finding the embedding using MDS. In the process of dimensional reduction, setting the weight within the dataset is very important. FINE made this process very simple by not specifying the metric, but just by estimating the distribution of each data point.

Finally, Spherical Laplacian Information Maps [71] is the most recent work that the following section will expand on. If we have some idea about what the low dimensional structure would be, we can constrain the embedding space with its space. For example, if we have a dataset of a single object images at different angles, we know the hidden structure of this dataset will be in the three dimensional space, probably within some radial space around the object. Using the distance matrix setting from FINE and the kernel and objective function setting from Laplacian eigenmaps, SLIM embeds the high dimensional data to a low dimensional spherical space.

### 4.2.2 $S^3$ and Unit Quaternion

A unit 3-sphere, $S^3$, is mathematically defined as following:

$$S^3 = \{(x_0, x_1, x_2, x_3) \in \mathbb{R}^4 : x_0^2 + x_1^2 + x_2^2 + x_3^2 = 1\} \tag{4.1}$$

It is basically a sphere in the four dimensional space. The special orthogonal group in three dimensions, SO(3), is about all rotations in the three dimensional Euclidean space, $\mathbb{R}^3$. The unit quaternion is the coordinate system that has full description of the SO(3) group.

$S^3$ is a double covering group of SO(3). This means that two different points in $S^3$ correspond to one same rotation in the three dimensional space. This fact can be easily shown by knowing the structure of the quaternion. The quaternion is a number system combining two complex numbers. However, in the aspect of rotations, it is a four vector representing the three dimensional rotation axis, $\boldsymbol{v}$, and the angle, $\theta$, respect to that axis. With a simple manipulation of the equations, the axis and the angle can be expressed with the coordinates of the quaternion points.

$$h = (x_0, x_1, x_2, x_3) = (\cos\frac{\theta}{2}, \sin\frac{\theta}{2} \cdot \boldsymbol{v}) \tag{4.2}$$

$$\begin{aligned} \theta &= 2 \times \arccos x_0 \\ \boldsymbol{v} &= \frac{(x_1, x_2, x_3)}{\sin\frac{\theta}{2}} \end{aligned}$$

Under the SO(3) interpretation, two antipodal points in $S^3$ represent the same rotation.

$$-h = (-x_0, -x_1, -x_2, -x_3) = (\cos\frac{\theta'}{2}, \sin\frac{\theta'}{2} \cdot \boldsymbol{v}') \tag{4.3}$$

$$
\begin{aligned}
\theta' &= 2 \times \arccos(-\mathrm{x}_0) \\
&= 2 \times (\pi - \arccos \mathrm{x}_0) \\
&= 2\pi - \theta \\
&\equiv -\theta \\
\boldsymbol{v}' &= \frac{(-\mathrm{x}_1, -\mathrm{x}_2, -\mathrm{x}_3)}{\sin \frac{\theta'}{2}} \\
&= \frac{(-\mathrm{x}_1, -\mathrm{x}_2, -\mathrm{x}_3)}{\sin(\pi - \frac{\theta}{2})} = \frac{(-\mathrm{x}_1, -\mathrm{x}_2, -\mathrm{x}_3)}{\sin \frac{\theta}{2}} = -\boldsymbol{v}
\end{aligned}
$$

As the sign of an angle is according to the direction of the axis (clockwise and counter-clockwise), a negative angle rotation to a negative directed axis is identical to the angle's absolute valued (positive) rotation to the axis switched its direction to positive.

It is obvious that only two antipodal points correspond to one same rotation. If there are two different $S^3$ points, $\mathrm{h} \neq \mathrm{h}'$ & $\mathrm{h} \neq -\mathrm{h}'$, and they represent the same rotation, there is an obvious contradiction to the statement.

$$
\begin{aligned}
\mathrm{h} &= (\mathrm{x}_0, \mathrm{x}_1, \mathrm{x}_2, \mathrm{x}_3) \quad \mathrm{h}' = (\mathrm{x}'_0, \mathrm{x}'_1, \mathrm{x}'_2, \mathrm{x}'_3) \\
\theta &= 2 \times \arccos \mathrm{x}_0 = 2 \times \arccos \mathrm{x}'_0 \\
&\rightarrow \arccos \mathrm{x}_0 = \arccos \mathrm{x}'_0 \\
&\therefore \mathrm{x}_0 = \mathrm{x}'_0 \quad \textit{or} \quad \mathrm{x}_0 = -\mathrm{x}'_0 \qquad \textit{contradiction}!
\end{aligned}
$$

Using this basic relationships between $S^3$ and SO(3), the optimization process in QLIM will be justified. In the section 4.3.3, these properties of the unit quaternion space will be used in calculating gradients for the optimization.

## 4.3 Methodology: Quaternion Laplacian Information Maps

Quaternion Laplacian Information Maps, abbreviated as QLIM, is a methodology of reducing the dimensionality of a given dataset to that of the unit quaternion space. Although QLIM follows the steps of SLIM [71], the embedding objective function and its optimization process are different from that of the embedding with the spherical constraint. The first part of estimating (or actually calculating) the distribution and constructing neighborhood matrix are followed from FINE [75]. Laplacian eigenmaps' [74] methods of calculating weights among the points and setting the kernel matrix in the embedding function are utilized. Finding the optimal embedding from the objective function is specified according to the unit quaternion space.

### 4.3.1 Formation of a Weight Matrix from the Input Data

Given a dataset, each point's density is calculated and denoted as $p_i$, $i = 1, ..., N$, where $N$ = the number of data points. The distance between two distributions is defined by the Fisher information distance [76]. However, without the prior knowledge about the geometry, or the prior's of the distribution parameters, it is hard to compute the exact value of the Fisher distance. Therefore, the Hellinger distance, which is proven to converge to the value of Fisher distance when the two distributions are similar [71], is used.

$$D_H(p_i, p_j) = \sqrt{\int \left(\sqrt{p_i(x)} - \sqrt{p_j(x)}\right)^2 \mathrm{d}x} \tag{4.4}$$

However, only the distances between the neighboring points are desired to be known because knowing all the distances and reducing them are the same as MDS. Furthermore, Hellinger distance does not converge to Fisher distance if the two distributions are very different. There are two ways to select the appropriate neighbor points: by computing the k nearest neighbors based on the $D_H$ values or by thresholding the

distance, $D_H < \varepsilon$, and assigning a large value to the points beyond that threshold. The weight matrix, which computes the weight based on this neighboring distance matrix, is calculated using a Gaussian kernel.

$$W_{ij} = exp(-D_T(p_i, p_j)/t) \tag{4.5}$$

$$D_T(p_i, p_j) = \begin{cases} D_H(p_i, p_j) & \text{if i and j are neighboring} \\ \max D_H(p_i, p_j) & \text{otherwise} \end{cases} \tag{4.6}$$

,where t is some constant, which is considered as the kernel width. This weight matrix is a summarization of the high dimensional information, and this matrix is the only input to the embedding function beyond this step.

### 4.3.2 Design of the Embedding Objective Function with Quaternion Constraints

The objective of the low dimensional embedding is to place two samples highly weighted closely and lightly weighted far away in the low dimensional manifold. In order to design this objective with the given weight matrix, the geodesics in the embedding space, the unit quaternion space in QLIM, have to be defined. It is known that the geodesics in the spherical space are arc cosine of the inner product of two points. It is simple derivation to show that the geodesics in the unit quaternion space are the same as those of the spherical space:

$$D_q(q_i, q_j) = \arccos(q_i \cdot q_j) \tag{4.7}$$

Knowing both the weight matrix of the original dataset and the geodesics in the embedding space, we can utilize the Laplacian eigenmaps [74] framework, just like

SLIM [71] did.

$$Q = \arg\min_{q_i} \sum_i \sum_j W_{ij} D_q(q_i, q_j) \tag{4.8}$$

Here, Q is all the embedding points, $Q = q_1, ..., q_N$. One trivial embedding satisfying this objective function is to place all the point in one same place, leading all $D_q$'s to zero. In order to avoid this situation, additional constraint is needed in the objective function. The goal of this constraint is to make the embedding points spread throughout the space.

$$Q = \arg\max_{q_i} \sum_i \sum_j D_q(q_i, q_j)^\gamma \tag{4.9}$$

, where $\gamma$ is the parameter that controls the degree of the spread over the space. Since the objective of the equation 4.9 is to maximize its value, the spread of the embedding will try to become noisy to increase their summations of the point to point geodesics by creating unnecessary zig zags instead of straight layout. A regulation parameter, $\lambda$, is multiplied to decrease this unnecessary noisy occurring in the process of optimization. Therefore, the final objective function that transforms the dataset weight matrix to the low dimensional embedding is

$$Q = \arg\max_{q_i} \sum_i \sum_j \lambda D_q(q_i, q_j)^\gamma - W_{ij} D_q(q_i, q_j) \tag{4.10}$$

### 4.3.3 Optimization

Equation 4.10 does not have a closed form solution because the geodesics defined are nonlinear. Therefore, the optimal embedding is found using gradient based optimization schemes. There are two options: first, the gradient ascent can be applied directly in the quaternion space, which is a constrained optimization. Second, the embedding points can be projected to the Euclidean space using stereographic projection. An unconstrained optimization can be applied in the Euclidean space and then projected back to the original quaternion space. Both methods are valid, but

the manipulation of gradients in the quaternion space is not fully proved yet.

Using the gradient descent (gradient ascent in the case with QLIM since it is finding the maximum) on the open Euclidean space is straight forward. Moving the variable according to its gradient direction, it will eventually arrive at the objective function's pivot points. However in the unit quaternion space, gradients can lead the variables, the embedding points in QLIM, outside of the quaternion space since a gradient of a quaternion point is not necessarily quaternion. Therefore, after each steps, each point is normalized to be projected back to the unit quaternion space. This procedure is introduced in the paper by Schmidt et al. [77], and the proof is shown in Section 4.6: Appendix.

$$\mathrm{J} = \sum_{\mathrm{i}} \sum_{\mathrm{j}} \lambda \mathrm{D_q}(\mathrm{q_i}, \mathrm{q_j})^{\gamma} - \mathrm{W_{ij}} \mathrm{D_q}(\mathrm{q_i}, \mathrm{q_j}) \tag{4.11}$$

$$\begin{aligned} \mathrm{Q_{n+1}} &= \mathrm{Q_n} + \mu \frac{\partial}{\partial \mathrm{Q_n}} \mathrm{J} && (4.12) \\ \mathrm{Q_{n+1}} &= \|\mathrm{Q_{n+1}}\| && (4.13) \end{aligned}$$

Equation 4.12 is the iterative steps in the gradient ascent method, and $\mu$ is the step size.

There is a bijective mapping from $S^n$ to $\mathbb{R}^n$ except for one pole in $S^n$, which is called stereographic projection. If all the unit quaternion points, which is a subset of $S^3$, are projected to a plane in $\mathbb{R}^3$, unconstrained optimization can be used to optimize QLIM embedding. To elaborate this mathematically, let $U = \mathbb{S}^3 - (0, 0, 0, 1)$, and $\varphi^{-1} \colon U \to \mathbb{R}^3$ be the stereographic projection:

$$(x_1, x_2, x_3, x_4) \in U \mapsto \left( \frac{x_1}{1 - x_4}, \frac{x_2}{1 - x_4}, \frac{x_3}{1 - x_4} \right). \tag{4.14}$$

And $\varphi\colon \mathbb{R}^3 \to U$,

$$(X_1, X_2, X_3) \in \mathbb{R}^3 \mapsto \frac{1}{1 + X_1^2 + X_2^2 + X_3^2}(2X_1, 2X_2, 2X_3, -1 + X_1^2 + X_2^2 + X_3^2). \quad (4.15)$$

The objective function for QLIM is

$$J = \sum_{i,j} (\lambda D_{ij}^{\gamma} - W_{ij} D_{ij}) \quad (4.16)$$

where $D_{ij}$ is the arc distance between sample points $q_i$ and $q_j$, which is denoted as $D_q(q_i, q_j)$ in above equations.

Since all the maps involved are smooth, we use chain rule to compute the gradient of $\overline{J} = J \circ \varphi$. Consider the gradients of $J$:

$$\frac{\partial J}{\partial q_i} = \sum_{j \neq i} (\lambda \gamma D_{ij}^{\gamma - 1} - W_{ij}) \frac{D_{ij}}{\partial q_i} \quad (4.17)$$

$$= \sum_{j \neq i} (\lambda \gamma D_{ij}^{\gamma - 1} - W_{ij}) \frac{q_j^T}{\sqrt{1 - \langle q_i, q_j \rangle^2}} \quad (4.18)$$

Recall that $\overline{J}$ will be a function of $\mathbb{R}^{3n}$ where $n$ is the number of sample points. It suffices to provide the gradient for the first three coordinates. This is step is simple. For first three coordinates $(X_1, X_2, X_3)$, compute $q_1 = (x_1, x_2, x_3, x_4) = \varphi(X_1, X_2, X_3)$, and

$$\frac{\partial \overline{J}}{\partial X_{1,2,3}} = \frac{\partial J}{\partial x_{1,2,3,4}} \circ \varphi' \quad (4.19)$$

$$= \sum_{j \neq 1} (\lambda \gamma D_{1j}^{\gamma - 1} - W_{1j}) \frac{1}{\sqrt{1 - \langle q_1, q_j \rangle^2}} q_j^T \varphi' \quad (4.20)$$

The Hessian can be computed as well, but the matrix size will be very large ($3n$ by $3n$), and it looks like there is no sparse structure either.

## 4.4 Experiments and results

### 4.4.1 ECG Analysis: Dimension-reduced Embedding and Classification of Pace-map Origins

12-lead ECG signals of VTs and pace-maps contain the information about their sites of origin in the heart. VTs and pace-maps (induced VTs) are arrhythmias that originate from scar tissue and electrically activate in a manner that results in a particular 12 lead ECG morphology that is different for each VT. The origin of the VT can be determined based on the 12 lead ECG morphology of the VT. The different leads of the ECG record the electrical activation in different directions. The signals generated by the VT reflect the directional electric activation along the recording leads the ECG. As indicated in Chapter I Section 1.2.1, the ECGs are collected from 10 electrode leads that are placed on the limbs and the precordiums. Figure 4.1 describes the direction that each lead represents in the three dimensional space. The leads from limbs (I, II, III, aVL, aVR, and aVF) describe the directions in the plane parallel to the body. The precordial leads (V1-V6) covers the directions in the plane that is perpendicular to the body.

The origin location and directional information in ECG signals are what we want to extract through this dimension-reduced embedding. The experiments with ECGs will show how QLIM presents this information better compared to other dimensionality reduction methods.

The ECG dataset from Chapter II, that consists of 3277 pace-maps from 43 patients and 51 VTs from 26 patients, has been labeled with regional information as described in Section 2.3. Since we have the labels to each ECG data points, ECG signals are embedded in Euclidean, spherical, and quaternion space using multi-dimensional scaling (MDS), Laplacian eigenmap (LEM), SLIM, and QLIM. Using these embedding representations, classification of the regions of pace-map origins is performed

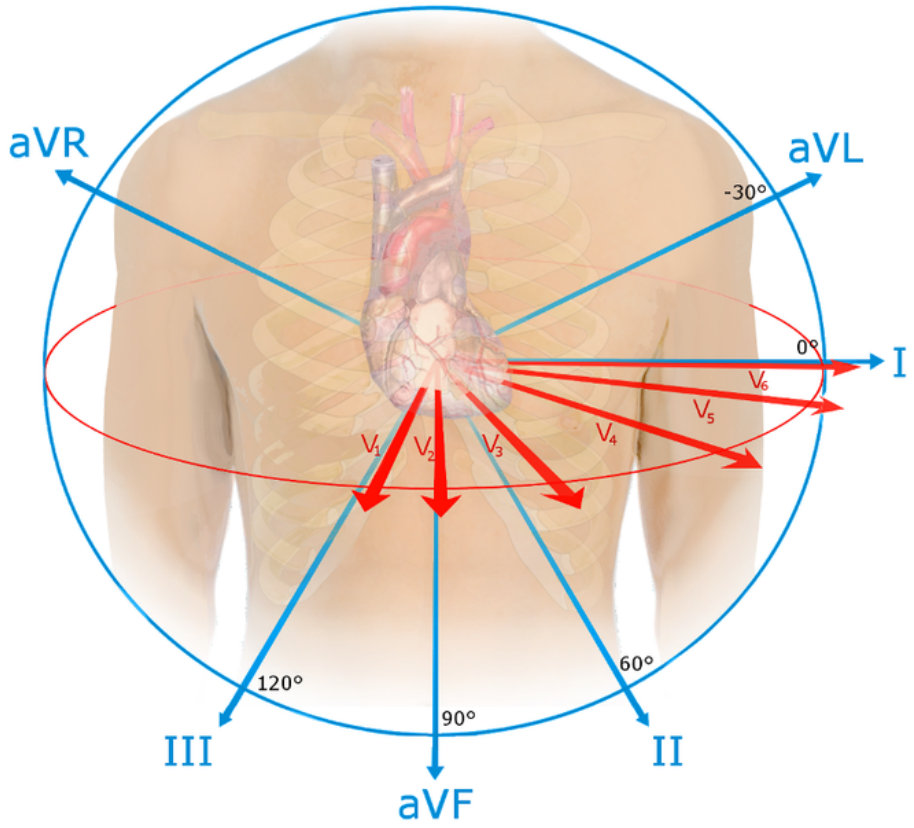


Figure 4.1: Directions of ECG Leads in Three Dimensions. Reprinted from Electrocardiography, In *Wikipedia,n.d.*, Retrieved April 14, 2015, from http://en.wikipedia.org/wiki/Electrocardiography. Reprinted with permission.

with support vector machine (SVM).

#### 4.4.1.1 Classification of Left Ventricle, Endocardial Pace-maps

In order to use QLIM for ECG analysis, an underlying assumption that the origin of VTs and pace-maps lie on a single, closed manifold is needed. In previous research by Yokokawa et al. [41], a classification of VTs and pace-maps originating only from a single, endocardial chamber was presented. Pace-mapping was performed from a total of 921 left ventricular, endocardial sites in 33 patients, and the pace-maps were categorized to 10 regions in the left ventricle. Following this work, we started by analyzing pace-map ECGs from left ventricle, endocaridum only. First, pace-maps from the regions with less than 50 samples are excluded, that narrows down the number of suitable pace-maps to 648 from 4 regions in 18 patients.

The embeddings of 648 pace-maps using MDS, LEM, SLIM, and QLIM were presented in Figure 4.2. The embedding space was well represented from the figure. MDS and LEM projected the point into open Euclidean space, and SLIM forced the point to be on the spherical surface. Since a unit quaternion is a four dimensional vector, visualizing quaternions is not easy. The embedded quaternion points were transformed to a three rotational angles, pitch, yaw, and roll, and those angular values were plotted in XYZ coordinates.

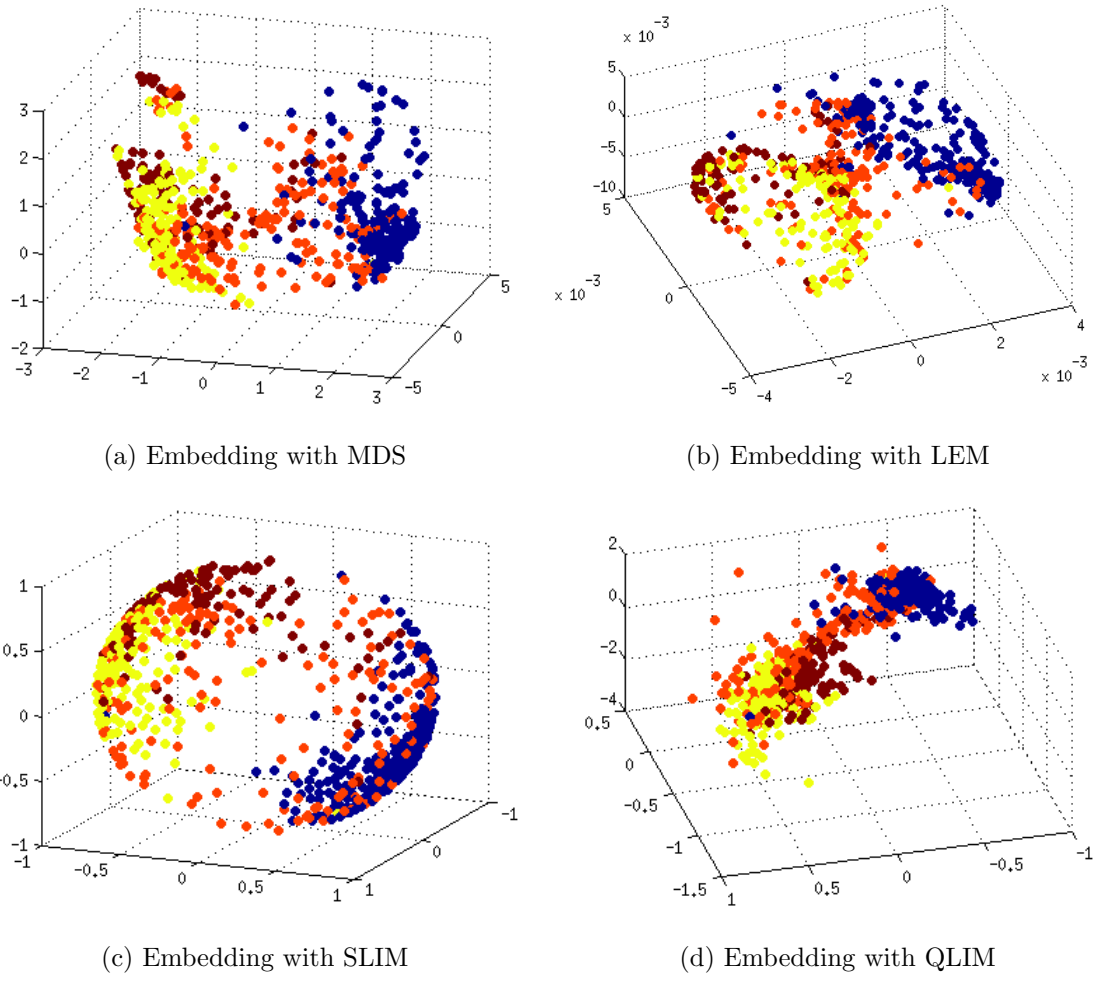

(a) Embedding with MDS

(b) Embedding with LEM

(c) Embedding with SLIM

(d) Embedding with QLIM

Figure 4.2: 648 Endocardial Pace-maps Embedded with Different Dimensionality Reduction Methods. The colors represent different regions in the left ventricle. Blue: D endo, Yellow: G endo, Red: H endo, Brown: I endo.

Overall, a strong separation between pace-maps from region D (blue) and region G (yellow) was observed from QLIM. Pace-maps from region H (red) were generally

spread over the range for all four embeddings. Based on these data it is difficult to conclude the superiority of any of these methods over each other. Therefore, classification in four regions was performed with each representation from different dimensionality reduction methods. All classifications were trained and tested with SVM with radial-basis kernel. It was cross-validated with leave-one-patient-out, following the procedure in Chapter II. For SLIM and QLIM, the embedding results were not uniform for each trial because the gradient method was used for their optimization. The classification accuracy was averaged over ten trials for SLIM and QLIM embedding cases.

| Dimensionality Reduction | Classification Accuracy |
|---|---|
| None (raw signal) | 64.97% |
| MDS | 65.90% |
| LEM | 67.13% |
| SLIM | 67.75% |
| QLIM | 68.07% |

Table 4.1: 648 Endocardial Pace-maps' 4 Region Classification Using Representations from Different Dimensionality Reductions

All four embeddings resulted in a higher classification accuracy than the classification using raw ECG signals. With the knowledge that the pace-map points we analyzed were on a closed surface of the inner ventricular wall (endocardium), which can be interpreted as a deformation of a hemisphere, it is reasonable to postulate that the embedding in quaternions resulted in the highest classification accuracy.

#### 4.4.1.2 Classification of Epicardial Pace-maps

All epicardial VTs and pace-maps have their sites of origins on a closed surface sourrounding both left and right ventricles. Therefore, epicardial pace-maps of left and right ventricles can be analyzed together unlike the endocardial pace-maps.

As in the previous section, the regions with less than 50 samples were excluded. 843 epicardial pace-maps from 20 patients and 4 regions, including two regions from

the left ventricle and two regions from the right ventricle, were selected.

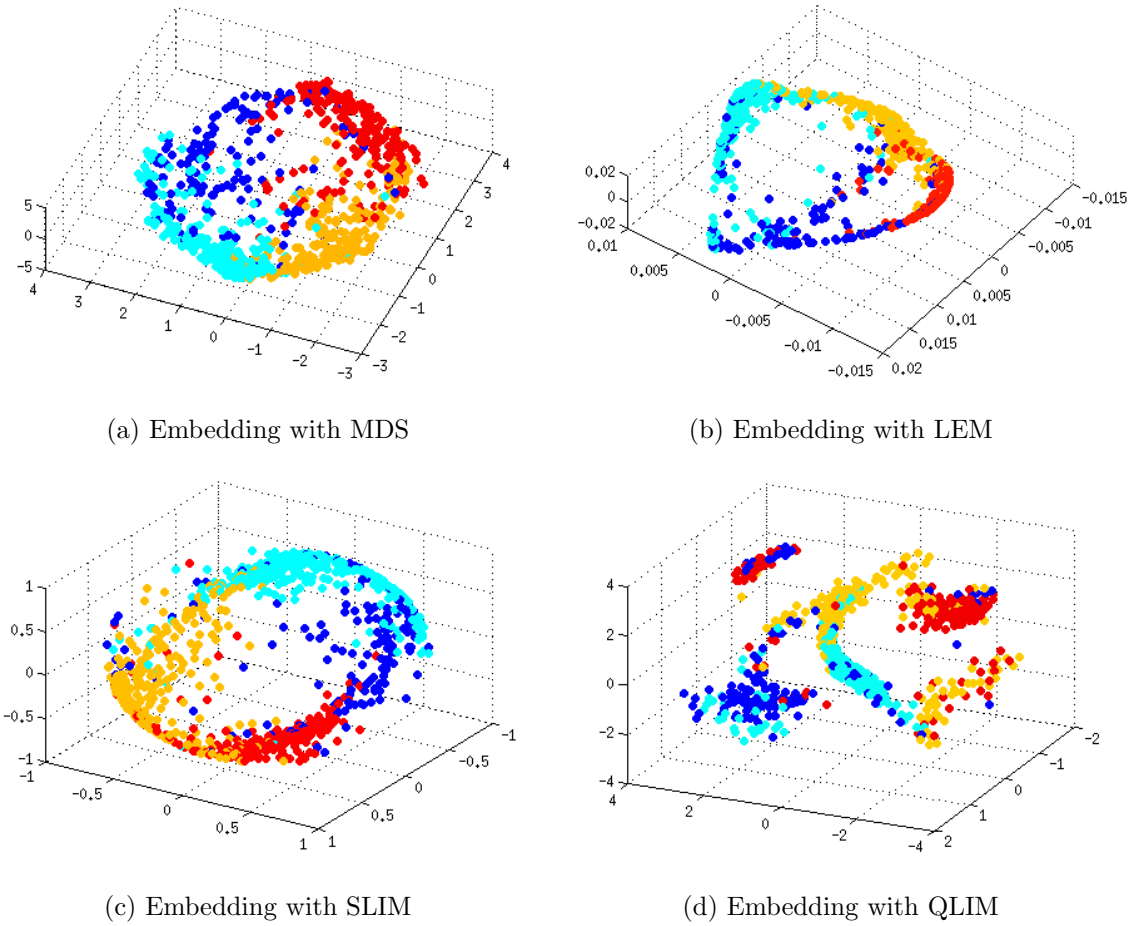

(a) Embedding with MDS

(b) Embedding with LEM

(c) Embedding with SLIM

(d) Embedding with QLIM

Figure 4.3: 843 Epicardial Pace-maps Embedding with Different Dimensionality Reduction Methods. The colors represent different regions in the epicardial ventricle. Blue: C epi (LV), Light blue: D epi (LV), Yellow: K1 epi (RV), Red: K2 epi (RV).

For the embedding of epicardial pace-maps, an apparent separation between the left ventricle (blue and light blue) and the right ventricle (yellow and red) pace-maps exists in QLIM. Also, pace-maps from D region (light blue), K1 region (yellow), and K2 region (red) have strong clusters together while pace-maps from C region (blue) tend to spread through the embedding space. It is also interesting to see how SLIM enforces the embedding on a circular strip. For QLIM, as the embedded quaternions are presented with the pitch, yaw, and roll converted from the 4-vector quaternions, the periodicity of these rotation angles cause discontinuity on the three dimensional representation.

| Dimensionality Reduction | Classification Accuracy |
|---|---|
| None (raw signal) | 78.88% |
| MDS | 78.41% |
| LEM | 79.83% |
| SLIM | 78.77% |
| QLIM | 78.98% |

Table 4.2: 843 Epicardial Pace-maps' 4 Region Classification Using Different Dimensionality Reductions

Unlike the previous endocardial pace-map classifications, the classification accuracies are very close for all of the dimension-reduced representations. Solely using the raw ECG signal already has high classification results. LEM and QLIM by clustering the pace-maps with larger separations have better classification accuracies than the other methods.

### 4.4.2 QLIM with Images: Extraction of Rotational Information

By the nature of imaging, every image has a viewpoint direction or a camera angle. Especially, if an image presents an object, we can describe the viewpoint respect to the object's coordinate plane. This process of interpreting angular(or rotational) information from a given image is intuitive to human visual perception. Using dimensionality reduction, a sequence of single object images from different angles can be reduced to the space where rotation can be visualized and described. Through the following experiments, we analyze the parameters of QLIM and test the applicability of QLIM as a real image pose estimator.

#### 4.4.2.1 Parameters

There are two parameters in the objective function that have impacts on the embedding: $\gamma$, which controls the spread, and $\lambda$, which controls the noise level of the embedding points. Both of these parameters are very important in order to embed the points correctly. Since the dimensionality reduction is transforming high dimensional

data to low dimensional embedding points, distortions in representation can happen if it is not appropriately embedded. The general functionalities of each parameter are known from the setting of the objective function; however, it is desirable to better understand this trend.

A synthetic car data is used for this experiment. This data is a sequence of images of a red car pictured with a camera rotating 180 degree around the object in a circle. A pair of $\gamma$ and $\lambda$ value is set for each embedding, and the series of embedding is shown in a single figure. Ideally, the low dimensional trajectory supposed to be a complete semi-circle which represents the camera trajectory around the car. The complete results are shown in Figure 4.4.

The general trend of $\lambda$ is that the embedding becomes noisier as the value increases. This is because maximizing $\lambda D_q(q_i, q_j)^\gamma$ becomes more significant than minimizing $W_{ij}D_q(q_i, q_j)$ in equation 4.10. Especially when it becomes greater than 1, the noise significantly distorts the trajectory. The embedding is meaningless when either $\gamma$ or $\lambda$ is too small since, in this case, only the term with the weight matrix, $W_{ij}D_q(q_i, q_j)$, remains in the objective function, and the trivial embedding occurs. In Figure 4.4, this is completely shown with $\gamma = 0.01$. The visually best embedding with this dataset is with the value of $\gamma = 0.8$ and $\lambda = 1$. However, these parameter values also depend on the number of data points. When the number of images of this car is doubled without changing the camera rotation angles (180 degree around the car), the best embedding seemed to appear at the $\gamma$ value between 0.01 and 0.02 and the $\lambda$ value of 0.5. Therefore, if we can find more mathematical relationship between the embedding, the number of data points, the spread through $\gamma$, and the noise through $\lambda$, it will become a very powerful dimensionality reduction method.

80 pictures of a car rotating 180 degrees

(a) The Car Image Dataset Used to Test the Parameter Trends

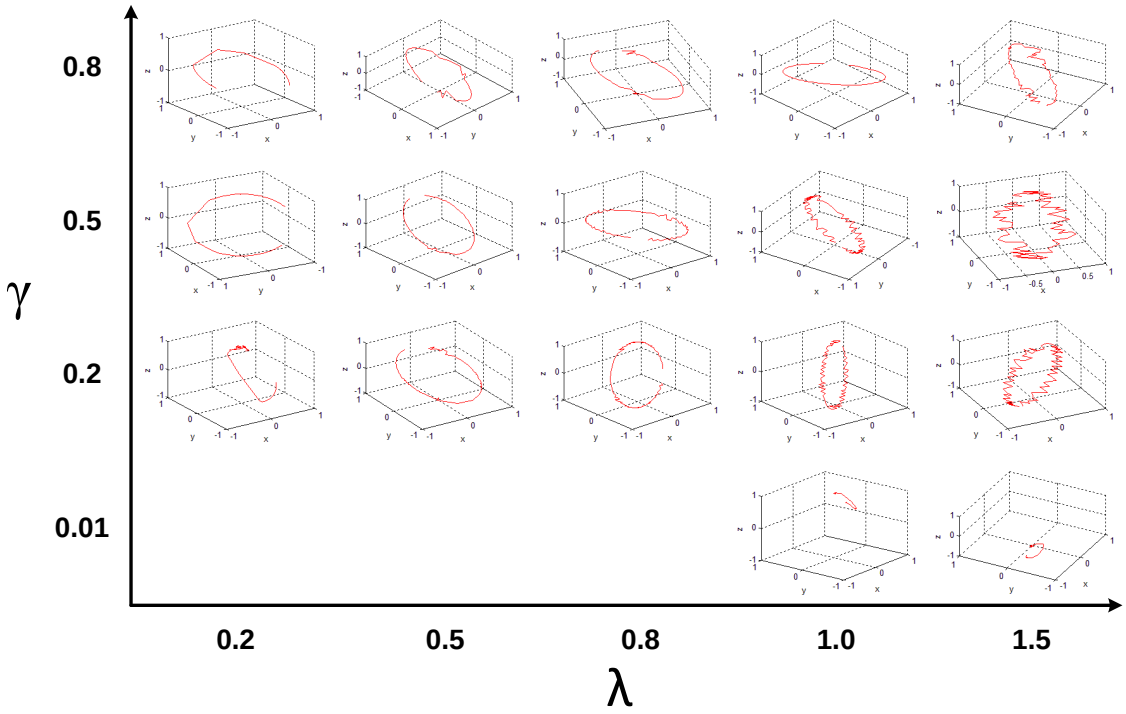


(b) The Parameter Trends. The vertical axis presents the values of $\gamma$ and the horizontal axis presents the values of $\lambda$

Figure 4.4: QLIM Parameter Anaylsis

#### 4.4.2.2 360 Degree Rotation with a Real Image

Figure 4.5 shows the real telephone images as high dimensional data, the QLIM embedding of that dataset, and the distance matrix, which is directly related to the similarity matrix and the kernel matrix, used in that embedding. The exact embedding of this dataset should be a whole circle, representing the full 360 degree rotation of the camera around the telephone. The QLIM embedding seems like a bent eclipse. This apparently is an inaccurate embedding, and it is not giving the exact (near the ground truth) values of the camera angle. However, when the distance matrix is examined, the QLIM embedding is reasonably explained. Although the first

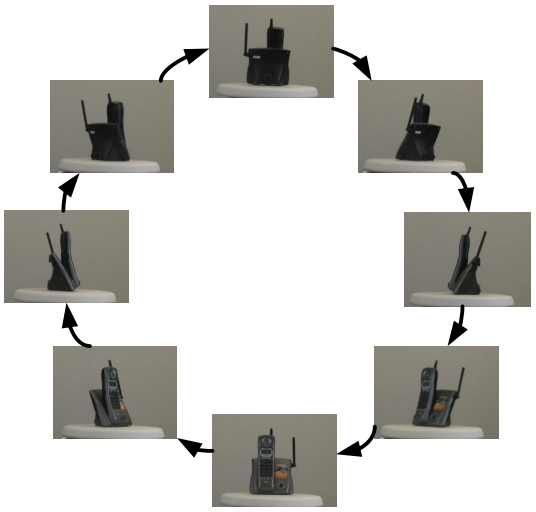

200 pictures of a phone rotating 360 degree

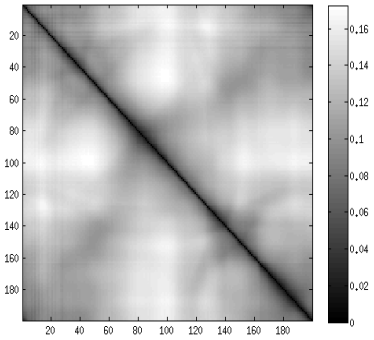


Distance Matrix

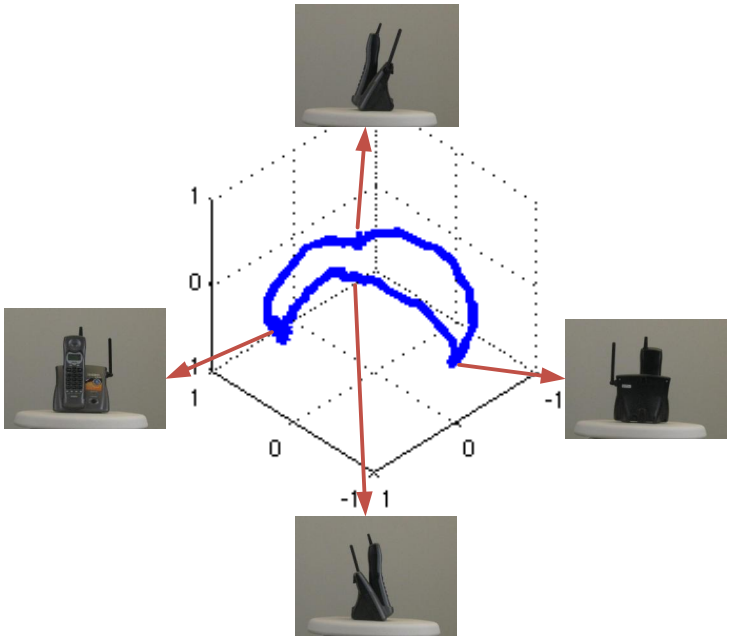


QLIM embedding with gamma value 0.02

Figure 4.5: QLIM Embedding of the Real Telephone Image Dataset and Its Distance Matrix. The embedding is reasonably explained with the presentation of the distance matrix.

and the hundredth images are very different, having a low kernel value, the images near the hundredth images (80 120) are similar to each other. We can see the definite high values through the diagonal from the right top to the left bottom. This is due to the left and right views of the telephone being similar, and thus, embedding points

cannot spread out. In order to get accurate angle values from the unit quaternion embedding through QLIM, an appropriate setting of the kernel function and the distance matrix should be able to recover this misleading information.

## 4.5 Conclusion and Future Research

In this chapter, we presented a dimensionality reduction methodology with a new type of embedding space. By constraining the embedding space to a unit quaternion space, the embedding function and its optimization process were modified. The quaternion embedding from QLIM provided better clusters and more information compared to that of spherical embedding from SLIM and open Euclidean embedding from MDS and LEM. The experiments with ECG data presented clusters by the belonging regions of the pace-map origins. The precision of the pace-map clustering is verified by classifying regions of the pace-map origins using the embedding representations as inputs. Also with the turntable image data, QLIM parameters were analyzed, and the rotational information that is contained in the images was observed.

There are following future work:

1. In depth analysis about the convexity of QLIM optimization
2. More experimental results with datasets involving more than three dimensional information (e.g. Electron Backscatter Diffraction (EBSD) data)

## 4.6 Appendix

### Relating the Method by Schmidt and Niemann [77] to Simple Normalization

The notations in the paper by Schmidt et al.[77] are as follows: Given the initial quaternion point as $h_0$, and the gradient at that point as $v_4$, the new quaternion point, $h_z$, shifted by the gradient is,

$$h_z = \sin\theta \times v_{4N} + \cos\theta \times h_0$$

,where $v_{4N} = \frac{v_4}{|v_4|}$ and $\theta = |v_4|$.

Now, let's start from the normalizing the vector that is originally the sum of $h_0$ and $v_4$. As $h_0$ is a unit quaternion, $|h_0|$ equals to the value of 1.

$$\begin{aligned} h_z &= \frac{h_0 + v_4}{|h_0 + v_4|} \\ &= \frac{|h_0|}{|h_0 + v_4|} \times h_0 + \frac{|v_4|}{|h_0 + v_4|} \times \frac{v_4}{|v_4|} \\ &= \cos\theta \times h_0 + \sin\theta \times v_{4N} \end{aligned}$$

The conversion of the fractions to sine and cosine is visually apparent in Figure 4.6. Also, the size of $\theta$ is indeed equal to the norm of $v_4$ because of the small angle approximation.

$$\theta \approx \tan\theta = \frac{|v_4|}{|h_0|} = |v_4|$$

Therefore, the method in this paper is equivalent to normalizing the shifted four vector so that it lies on the $S^3$ surface, not necessarily projecting to a quaternion point.

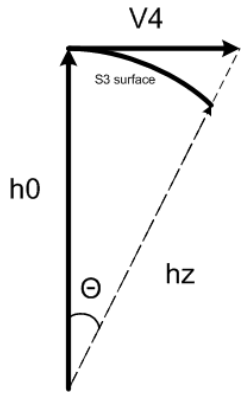


Figure 4.6: Shifting One Quaternion Point to Another Point on the Quaternion Surface

# CHAPTER V

# Analysis of Electrocardiograms from Ventricular Arrhythmias with Intramural Origins

## 5.1 Introduction

In the previous chapters analyzing electrocardiograms, the common goal was to identify the sites of origin of ventricular tachycardias. We started from classifying the sites of origin being inside or outside of a heart (endocardial versus epicardial) in Chapter II. In Chapter IV by using QLIM, we stratified the regional labels of origin. Ventricular arrhythmia can originate from the endocardium, the epicardium, or from within the myocardium (intramural). The distinction is important since the approach to ablation procedures depends on the origin of the VTs; for endocardial VTs an endocardial approach is required to eliminate VT, an epicardial approach is required for VTs originating in the epicardium and a combined epicardial-endocardial approach is often required for intramural VTs. In this chapter, we analyze the morphology of intramural VA ECG signals to differentiate them from non-intramural VA ECGs.

Intramural VAs are poorly understood and foremost there are no ECG criteria that distinguish intramural from epicardial or endocardial VAs. Although the existence of intramural VA has been has been suspected for some time [78], mapping and ablation of these arrhythmias have been described recently [79, 80]. Mapping and

ablation of intramural VAs is challenging and often results in procedural failure. For successful ablation of intramural VAs, often radiofrequency energy needs to be delivered from both aspects of the wall containing the intramural source. ECG recognition is important to adequately plan these procedures.

By pace-mapping, the origin of a VA is localized to the endocardium provided there is a matching pace-map in the endocardium. If there is a matching pace-map in the epicardium, the origin is epicardial. In case of an intramural VA, since the origin cannot be reached with the mapping catheter, a matching pace-map would not be expected from any location of the endocardium or epicardium. Since electrical activation spreads to both surfaces containing the intramural VA source, pacing from both surfaces where activation occurs first, is expected to result in a "combination of pace-maps" that is closer to the pace-maps obtained from either surface alone. Indeed, when combining pace-maps from the opposing walls and averaging them to a combined signal, the correlation between the combined signal and the intramural VA ECG increased significantly, and the mean square error decreased as compared to any pace-maps obtained from either surface alone. For the non-intramural VA cases, the correlation did not increase when the target pace-maps ECG were averaged with the pace-maps from either side of the cardiac surface.

Yet, distinguishing characteristics differentiating intramural from epicardial and endocardial VA origins remain to be described. One would expect though, that ECG characteristics would be different if endocardial surfaces would be activated simulatenously from an intramural focus compared to activation that originates from the endocardial vs the epicardial surface where the initial activation is prefereentially from one surface that is closest to the origin of the VA. The slope feature that results in a dramatically different QRS morphology of endocardial vs epicardial ECG morphologies would be expected to be intermediary for intramural VAs. However, this intramural versus non-intramural classification is a part of future work and not

presented in this chapter.

This chapter is organized as follows: A brief summary on the previous related work is presented in Section 5.2. Section 5.3 explains analytically how the intramural and non-intramural VA ECGs are different by comparing each signals to the intramural-like ECG signals averaged from the two nearest pace-map signals on each side of the heart wall. The numerical results to show the difference between the intramural and non-intramural ECGs are presented in Section 5.4. In Section 5.5, we conclude the chapter and list possible future work.

## 5.2 Related Work

Although it was not widely researched throughout the years, cardiologists have had interest in the intramural heart. The interest to map and eliminate intramural VTs was limited initially to patients undergoing surgical therapy of VT. The publications outline limitations of the surgical procedure in eliminating these VTs [78].

The focus to arrhythmias originating from intramural heart was brought up from the paper by Yokokawa et al. [79] in 2012. From 93 idiopathic patients having no structural heart diseases, 7 patients wer found to have arrhythmias with intramural sites of origins. Knowing that they have intramural VAs, the paper explains how the ECG mapping is different and how the ablation was proceeded. To characterize intramural ECG signals, they used the amplitude and time length of R and S waves in lead V1 and V2. These ECG characteristics were not universal, only being able to differentiate intramural VA ECGs occurring in certain regions of the heart.

A consecutive paper was published in the following year by Desjardins and Yokokawa et al. [80]. This paper presented detection of intramural VAs from non-ischemic cardiomyopathic patients using delay-enhanced magnetic resonance imaging (DE-MRI) and voltage mapping. DE-MRI, being an imaging method, can precisely detect the extent and location of the scar. Desjardins et al. also shows that voltage mapping can

characterize intramural VAs, but not as accurately as the performance of DE-MRI.

Radiofrequency ablation is limited in reaching intramural foci if the depth is ¿3-5 mm within the myocardium. Ablation from both aspects of the intramural focus by the use of a bipolar [81] or unipolar mode [82] has been described to result in deeper lesion generation compared to sequential unipolar ablation which is the current standard of care.

## 5.3 Distinction between ECGs of Non-intramural and Intramural Ventricular Arrhythmias

If two classes of signals are separable, there should be characteristics of signals, latent information, that are interpretable by the classifier. We know that non-intramural VAs and intramural VAs are ECGs originating from different heart locations, and distinctions between the two should exist. In this section, these distinctions are visualized by embedding the ECG signals into low dimensional space using the dimensionality reduction methods from Chapter IV. Also, the combination of pace-map signals with the origins nearby the target VAs are compared to the target VA ECGs for both non-intramural and intramural cases. This comparison is based on the signal morphology and the measures of similarity, Pearson correlation coefficient (CC) and root mean square error (RMSE). The comprehensive numerical results will be presented in Results and Discussion, Section 5.4.

### 5.3.1 The Dataset of Non-intramural and Intramural VAs

In order to analyze intramural VA ECGs, a new dataset of ECGs is required. Unlike the ECG dataset in the previous chapters, controlled sets of non-intramural and intramural VA ECGs are needed for a fair comparison between the two ECG sets. To fulfill this requirement, only the patients without structural heart diseases

(idiopathic patients) were collected in this analysis in order to control the variances caused by inclusion of patients with different cardiac disease conditions. Eighteen patients out of 228 idiopathic VA patients, who were referred to the University of Michigan Cardiovascular Center for ablation, were found to have intramural VAs. A total of 18 idiopathic patients with non-intramural VAs were selected as the control group.

Electrophysiologists can identify a site of origin as intramural by directly reaching the site of origin via a perforator vein. Alternatively, if there is no adequate perforator vein, the discrepancy of the site of earliest activation from two aspects of the wall with a non-matching pace-map (<10/12 leads) strongly argues for an intramural origin.

### 5.3.2 Visualization of Non-intramural and Intramural VAs Using Dimensionality Reduction

The aim of the analyses in this section is to present that non-intramural and intramural VA ECG signals are different from their nature. In order to achieve this goal, the differences between the non-intramural and the intramural PVCs and pace-maps were visualized by projecting ECGs to two or three dimensional space. As a first step, the signal differences between the PVC ECGs and the closest pace-map ECGs were calculated. The difference between a non-intramural PVC and its closest pace-map was a near-zero signal because their morphologies should be overlapping. The difference between a intramural PVC and its closest pace-map resulted in a signal with non-zero values. These difference signals were reduced their dimensionality to two dimensional space using multidimensional scale (MDS) and Laplacian Eigenmaps (LEM), and the embeddings were shown in Figure 5.1.

Differences in the distributions among the blue points (non-intramural PVCs) and the red points (intramural PVCs) were apparent in both embeddings. The blue points were forming a smaller spread near the origin while the red points were tending to

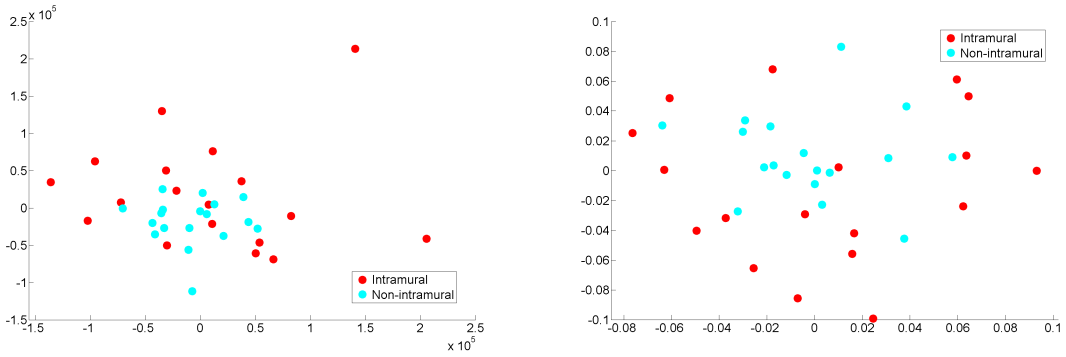


(a) MDS (b) LEM

Figure 5.1: The Differences between the PVCs and Their Closest Pace-maps Embedded to Two-dimensional Euclidean Space Using MDS and LEM. Each blue point indicates a difference signal between a non-intramural PVC and its closest pace-map. Each red point indicates a difference signal between an intramural PVC and its closest pace-map.

spread out. The differences between intramural PVCs and their closest pace-maps were large and uneven, having a wide spread in the embedding.

Now, the 36 actual ECG signals of PVCs and the 36 corresponding closest pace-map signals were embedded to a visualizable Euclidean space using various dimensionality reduction methods. The embeddings presented in Figure 5.2 and Figure 5.3 have three subfigures each; the first figure is the embedding of 18 non-intramural PVCs and their closest pace-maps. The second is the embedding of 18 intramural PVCs and their closest pace-maps. The last figure, more comprehensive than others, is the embedding of all PVCs and pace-maps from both cases of PVCs. In each subfigure, dark red points represent the PVCs, and dark blue points are referring to the pace-maps. Each patient's pair of a PVC and its closest pace-map is connected with a line: the blue lines indicate non-intramural PVC pairs, and the red lines indicate intramural PVC pairs.

In the embeddings of the non-intramural PVCs (Figure 5.2a), pairs of dark red (PVCs) and dark blue (pace-maps) points were close to each other, resulting in short blue lines. Some of the paired points were almost overlapping to each other that indicate a close similarity between the PVC ECG and the pace-map ECG. The em-

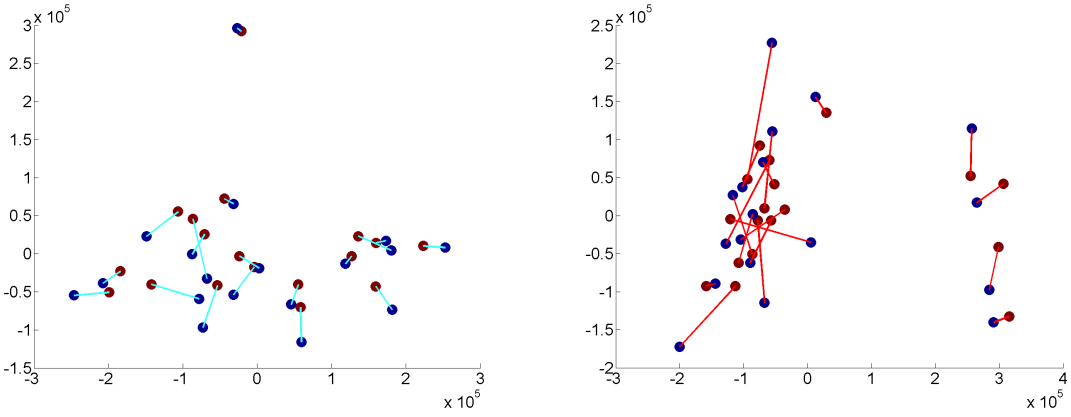

(a) MDS with the PVCs and the Closest Pace-maps from the Non-intramural Patients

(b) MDS with the PVCs and the Closest Pace-maps from the Intramural Patients

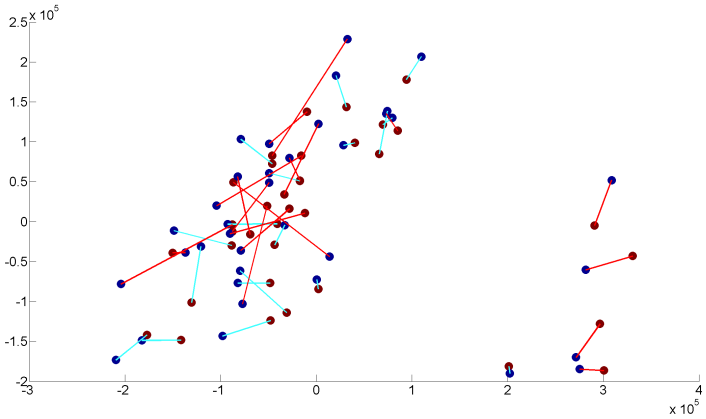

(c) MDS with the PVCs and the Closest Pace-maps from Both Patients

Figure 5.2: Multidimensional Scaling Embedding of the PVCs and the Closest Pace-maps. In each figures, dark red points represent the PVCs, and dark blue points are for the pace-maps. Each patient's pair of a PVC and its closest pace-map is connected with a line: the blue lines are indicating non-intramural PVC pairs, and the red lines are indicating intramural PVC pairs.

beddings with the intramural PVCs (Figure 5.2b) had larger separations between the PVCs and the paired pace-maps. There were pairs close to each other, but the general length of the line was longer than that of non-intramural PVC embeddings. For the intramural PVCs, even the pace-maps that were claimed to be the closest to the PVCs had large separations.

Finally, all 36 PVCs and 36 corresponding pace-maps were embedded together in Figure 5.2c. In this embedding, a direct comparison between the non-intramural PVC and pace-map pairs (blue lines) and the intramural pairs (red lines) was possible. The

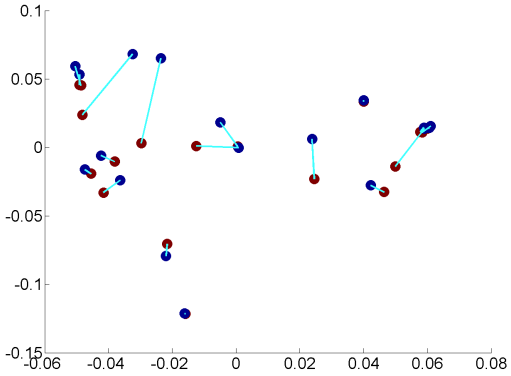


(a) LEM with the PVCs and the Closest Pace-maps from the Non-intramural Patients

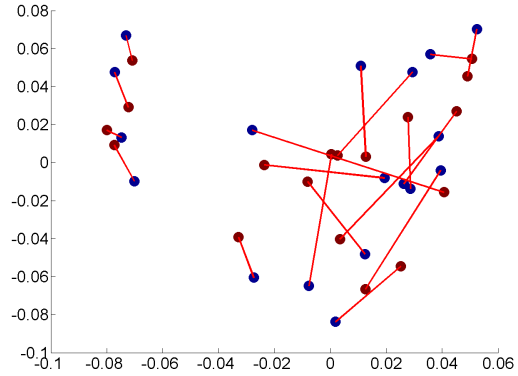


(b) LEM with the PVCs and the Closest Pace-maps from the Intramural Patients

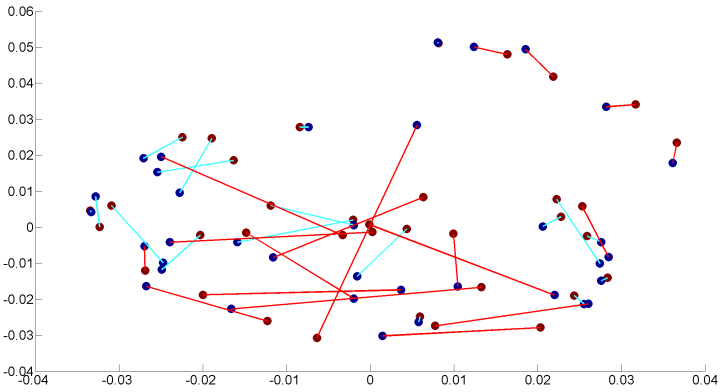


(c) LEM with the PVCs and the Closest Pace-maps from Both Patients

Figure 5.3: Laplacian Eigenmaps Embedding of the PVCs and the Closest Pace-maps. The format and color coding of the figure are identical to those of Figure 5.2.

lines between the intramural PVCs and pace-maps were longer than the lines between the non-intramural PVCs and pace-maps. Although many interpretations about each pair were reasonable, the analysis about the relationships among the pairs based on the embedding was not reliable because all the PVCs were from different patients. The patient variances were limited by collecting ECGs from idiopathic patients only; however, the physical differences of each heart could not be controlled for the ECG analyses.

The embedding outputs of LEM (Figure 5.3) presented more explicit differences between the non-intramural and the intramural PVCs. Especially, the embedding of all patients together was a good presentation of the PVC and pace-map pairs.

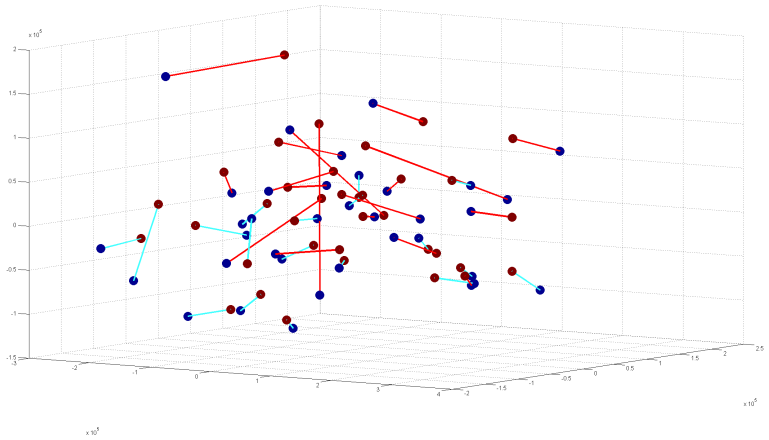

(a) MDS

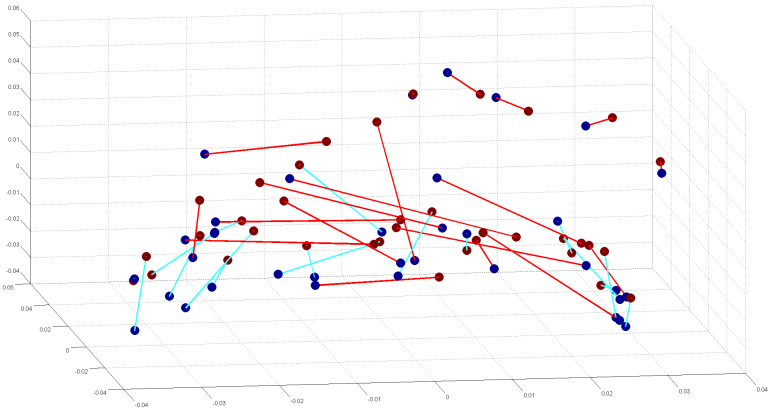

(b) LEM

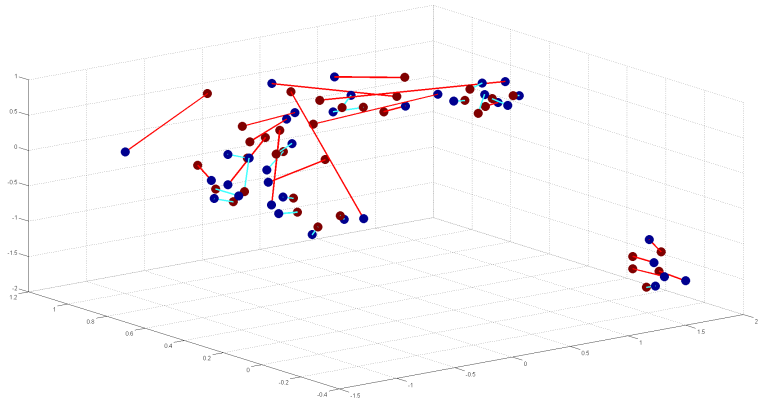

(c) QLIM with the PVCs and the Closest Pace-maps from Both Patients

Figure 5.4: Dimensionality Reduction Embeddings to Three Dimensional Spaces of the PVCs and the Closest Pace-maps from Both Patients Using Multidimensional Scaling, Laplacian Eigenmaps, and Quaternion Laplacian Information Maps. The format and color coding of the figure are identical to those of Figure 5.2.

Lastly, representations from the dimensional reduction to three dimensional spaces were analyzed. For the three dimensional representations, Quaternion Laplacian Information Maps (QLIM) was used along with MDS and LEM. All three embeddings were shown in Figure 5.4.

Unlike MDS and LEM, QLIM has an underlying assumption in its lower dimensional embedding space. If all the inputs have a reference to a single, closed manifold, QLIM has an advantage in displaying the latent information. The QLIM experiments in Chapter IV used the datasets with this closed manifold constraint, such as pace-map ECGs with the origins from a closed heart surface and the images of a single object from a fix distance. Although the non-intramural and the intramural PVCs could not be assumed to have the closed manifold property, QLIM was successful in clustering the non-intramural PVCs and the corresponding pace-maps close to each other and the intramural PVCs and their closest pace-maps far apart. Therefore, the distinction between the non-intramural PVCs and the intramural PVCs was visually obvious through the embeddings using the dimensionality reduction methods.

For a quantitative interpretation of the three dimensional embeddings presented in Figure 5.4, we measured the length of the lines between the pairs. The mean and standard deviation of the length of the lines from 18 intramural PVC pairs and 18 non-intramural PVC pairs were presented in Table 5.1.

| Method | Origin of VAs | Length of the Pair | p value |
|---|---|---|---|
| MDS | Intramural | $8.82 \pm 5.69$ | 0.004 |
| | Non-intramural | $4.63 \pm 2.41$ | |
| LEM | Intramural | $0.027 \pm 0.021$ | 0.032 |
| | Non-intramural | $0.017 \pm 0.010$ | |
| QLIM | Intramural | $0.54 \pm 0.42$ | 0.001 |
| | Non-intramural | $0.17 \pm 0.09$ | |

Table 5.1: Average and Standard Deviation of the Length of the Lines Between the PVC and the Closest Pace-map Pairs

The average length of the lines for the intramural PVC pairs were much longer than

that of the non-intramural PVC pairs. The standard deviations for the intramural PVC pairs were comparatively large. This indicated that the length of the line for intramural PVC pairs could be either short or long. This broad distribution of line length for intramural PVC pairs made an overlap with the distribution with the non-intramural PVC pairs. However, with the p value being smaller than 0.05, the difference in the two distributions were statistically significant for all three embeddings from different dimensionality reduction methods.

### 5.3.3 Comparison with Combination Signals of Two Nearby Pace-map ECGs

From the physicians' experience on procedures and the work presented in the previous chapters, we know that pace-mapping at the arrhythmia origin produces an ECG that matches the VA ECG. However if the arrhythmia has an intramural origin, pace-map ECGs do not match with the intramural VA ECG. Our hypothesis is that a signal that matches the intramural VA ECG signal can be constructed by the combination of pace-maps that are nearby the origin of the intramural VA.

In this section, two similarity measures are used: the Pearson correlation coefficient (CC) and the root mean square error (RMSE). First, the two pace-maps from opposite sites of the myocardium with the highest CC to the VA are combined and averaged (examples shown in Figure 5.5). The CC and the RMSE between the PVC signals and all the pace-map signals from one aspect of the wall are calculated, and those values are compared to the CC and the RMSE between the PVC and the combination signals.

#### 5.3.3.1 Intramural Arrhythmia Patients

Figure 5.6 shows an example of the 12 lead ECG morphology of an intramural VA and the best matching pace-maps superimposed to each other. A 12-lead ECG

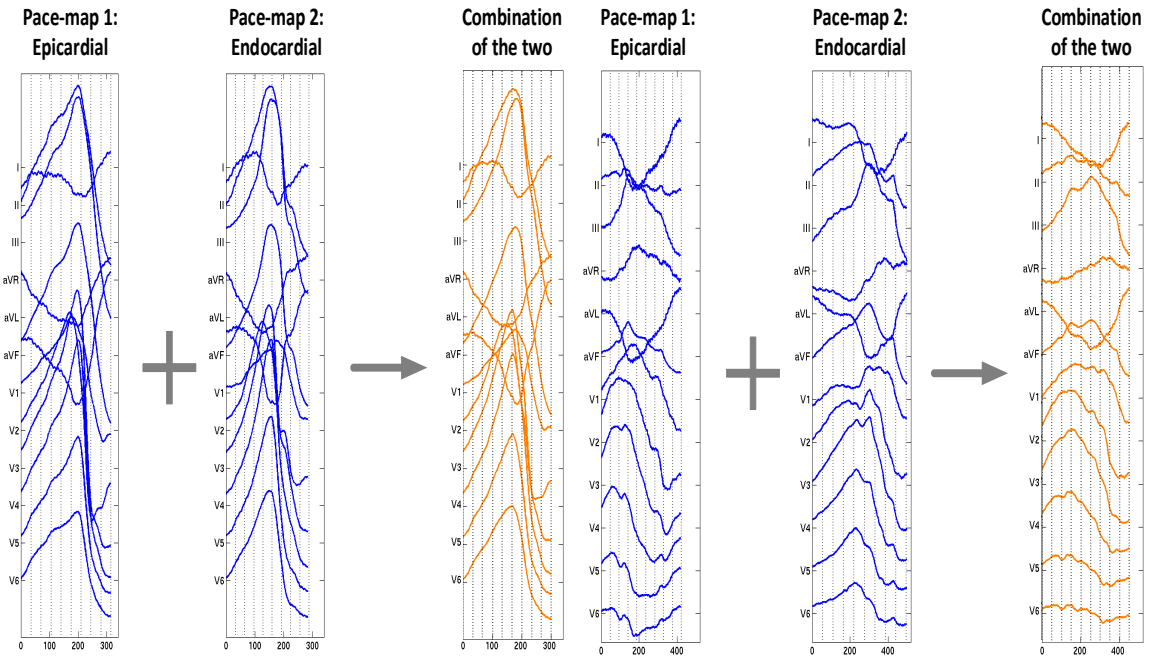


Figure 5.5: Combination of Two Pace-map ECGs by Average.
The two exemplary pace-maps (blue) from a patient is averaged to construct the combination signals (orange).

of the targeted PVC was plotted in black contours in all three subfigures. In Figure 5.6a, the signal of a pace-map (blue) obtained from the great cardiac vein (GCV) is shown. The correlation coefficient between the targeted PVC and the pace-map from GCV was 0.82, averaged over all 12 leads, and the root mean square error was 246.

The middle figure presents the signal of a pace-map (pink) obtained from the right ventricular outflow tract (RVOT). The CC between the pace-map and the PVC was 0.76, and the RMSE was 227. The pace-maps showed the highest correlation coefficient with the VA at the epicardium (GCV) and the endocardium (RVOT).

The rightmost figure shows the constructed ECG (green), which is the combination of the pace-maps from the great cardiac vein and the right ventricular outflow tract (GCV+RVOT). The correlation coefficient between the combination pace-map and the PVC was 0.91 and the RMSE was 190. The combination pace-map had a higher CC and lower RMSE value. The higher CC of a combination of pace-maps compared to single pace-maps from either side of the myocardium argues in favor of

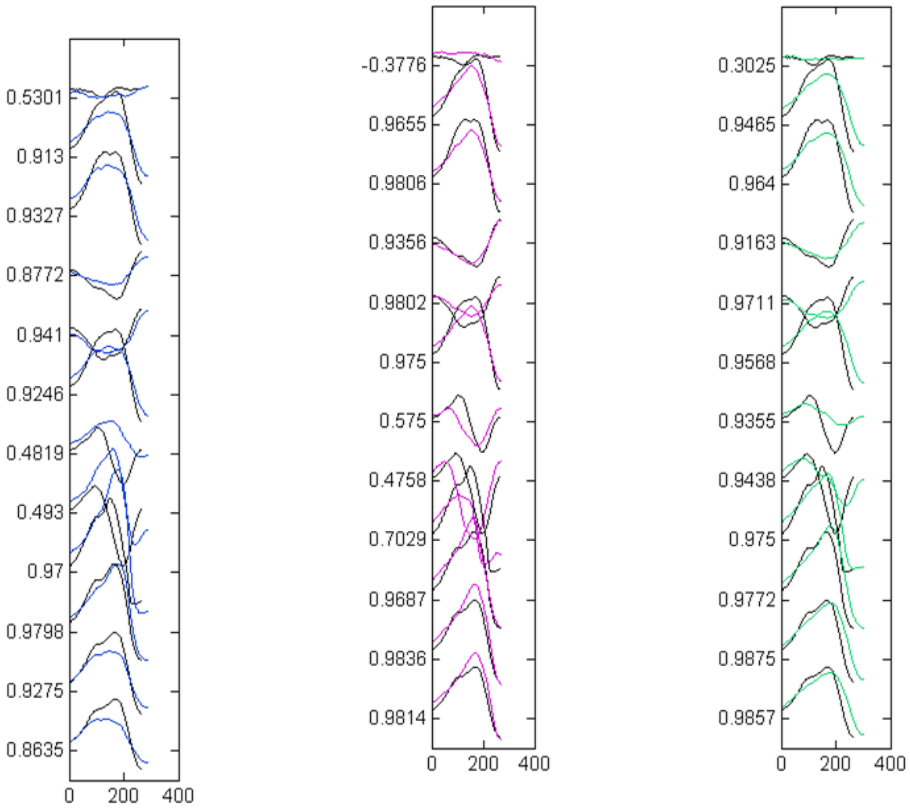


(a) GCV Pace-map and PVC

(b) RVOT Pace-map and PVC

(c) GCV and RVOT Pace-maps Combined and PVC

Figure 5.6: Pace-maps from a Patient with an Intramural Ventricular Arrhythmia. PVC is in black, and all other overlapped pace-maps are in colors. The numbers in y-axis are the CC values between the two signals for each lead.

an intramural origin of the VA.

#### 5.3.3.2 Non-intramural Arrhythmia Patients

A non-intramural VA patient's ECG is presented in Figure 5.7. As in Figure 5.6, a 12-lead ECG of the targeted PVC was plotted in black. The left figure shows an overlapped pace-map (blue) obtained from the GCV. The CC averaged over all 12 leads was 0.97, the RMSE, averaged as well, was 154. In fact, this patient had the site of origin of PVC in GCV, and this pace-map ECG shown was the best matching pace-map to PVC. For this patient, the radiofrequency ablation procedure at this site eliminated the PVC. The ECG of a combination of the pace-maps (green), one

pace-map from the GCV and the other pace-map from the left aortic cusp, is shown in the right figure. The CC of the combination pace-maps was 0.94 with an RMSE of 198. The combination pace-map for this non-intramural patient did have lower CC and higher RMSE.

Therefore, identification of a pace-map with a high correlation coefficient when pacing is performed from one side only compared to the targeted VA argues against an intramural origin of the VA.

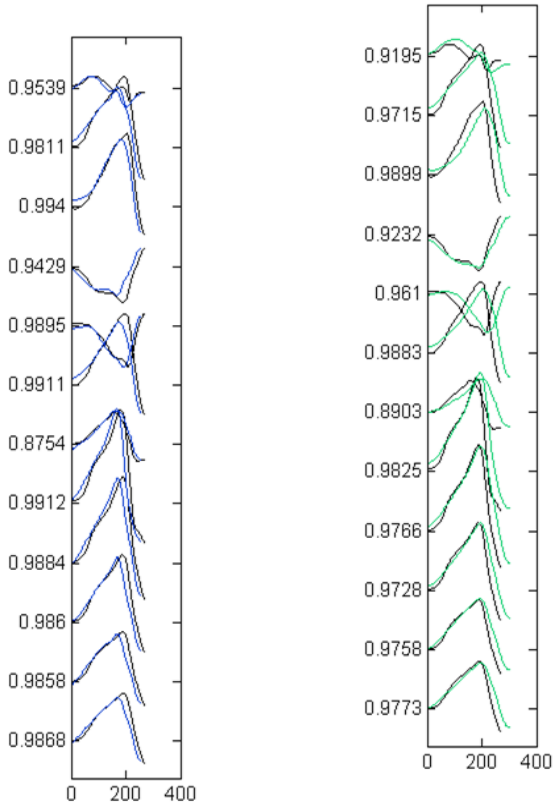


(a) GCV Pace-map and PVC

(b) GCV and Cusp Combined and PVC

Figure 5.7: Pace-maps from a Patient with a Non-Intramural Ventricular Arrhythmia. PVC is in black, and all other overlapped pace-maps are in colors. The numbers in y-axis are the CC values between the two signals for each lead

## 5.4 Results and Discussion

All relevant PVC and pace-map ECGs are collected from 36 patients, 18 intramural PVC patients and 18 non-intramural patients. Each patient has ECGs from a PVC, the best matching pace-map to that targeted PVC, and other pace-maps from nearby locations of the targeted PVC. These pace-maps are combined and averaged in pairs to find the best matching combination. The CC and RMSE are measured for the best matching pace-map and the best matching combination of pace-maps with respect to the targeted PVC. The comprehensive results are presented at the end of this section in Table 5.3.

Table 5.2 is the summary of the results. In patients with intramural PVCs, the combination ECGs of pace-maps had a significantly higher CC and lower RMSE values compared to the single matching pace-maps. In contrast, in patients with non-intramural VAs, single pace-maps from the sites of origin of the PVCs showed significantly higher CC than the combination signals obtained from pace-maps originated at the nearby anatomic locations to the sites of origins. For these non-intramural patients, RMSE increased when the pace-maps are combined. However, the p value, being greater than 0.05, indicated that the change in RMSE is not statistically significant.

| Origin of VAs | Type of measure | Matching pace-map | Combination of pace-maps | p value |
|---|---|---|---|---|
| Intramural | CC with PVC | $0.84 \pm 0.10$ | $0.87 \pm 0.10$ | $\ll 0.0001$ |
| | RMSE with PVC | $255 \pm 58$ | $239 \pm 63$ | 0.003 |
| Non-intramural | CC with PVC | $0.93 \pm 0.04$ | $0.89 \pm 0.05$ | 0.005 |
| | RMSE with PVC | $214 \pm 58$ | $221 \pm 50$ | 0.070 |

Table 5.2: Average Values of Correlation Coefficient and Root Mean Square Error for 18 Intramural and 18 Non-intramural PVC Patients

Graphical presentations of the CC and RMSE results in Table 5.3 are shown in

Figure 5.8. For each graph, X-axes are the values between the targeted PVC and the best matching pace-map, and Y-axes are the values between the targeted PVC and the combination of pace-maps. Thus, the upper triangular region is where the combination signals of pace-maps have higher values, and the lower triangular region is where single matching pace-map signals have higher values. Although there were some outlying patient points, the separations between the intramural and non-intramural PVC patients were apparent for both CC and RMSE plots.

## 5.5 Conclusion and Future Research

This chapter presents an under-researched area of VAs with intramural origins. Cardiologists found that arrhythmias can be originating from the intramural heart, and the diagnosis of intramural VAs through ECG signals was needed. This chapter successfully demonstrated that intramural VA ECG signals are different from non-intramural VA ECGs. First, the dimension reduced representations of ECGs from intramural and non-intramural patients presented different clusters between the two groups. Second, Intramural VA ECG signals had higher affinity measures (higher CC and lower RMSE) to the combination of two pace-map signals rather than to single pace-maps. Non-intramural patient ECGs were also compared in the same way as intramural patient ECGs to confirm that their ECG signals behave differently.

As the intramural VA is a relatively new field of research, there are different aspects to extend the research for the intramural VA ECG analysis. First, the type of patients in the intramural VA dataset can be diversified. The current intramural patients are all idiopathic patients. The intramural VA ECGs from patients with heart disease will have interesting variances as they did with the dataset used in Chapter II, III, and IV. Second, features that can describe the difference of intramural VA ECGs can be searched. As the fact that the intramural VA ECGs are different from non-intramurals is demonstrated in this chapter, selecting the feature, by signal space

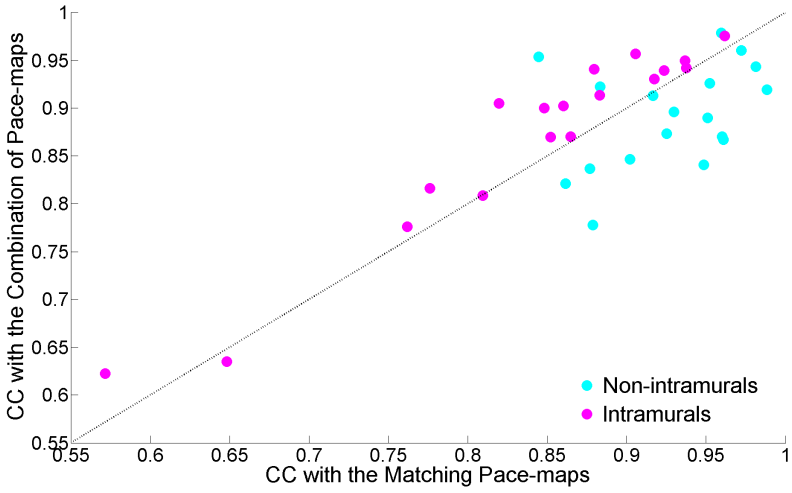


(a) Correlation Coefficient

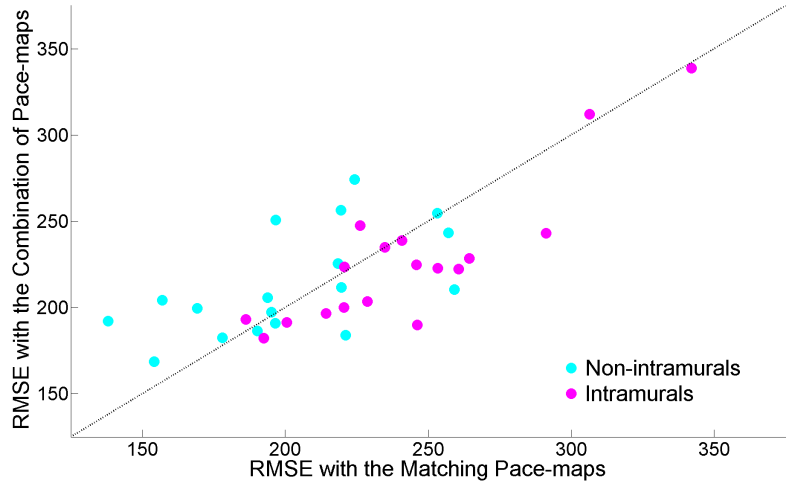


(b) Root Mean Square Error

Figure 5.8: Distribution of 36 Patients According to Correlation Coefficient and Root Mean Square Value. X-axis is the value between the targeted PVC and matching pace-map. Y-axis is the value between the targeted PVC and the combination ECG of pace-map.

analysis and/or unsupervised feature learning, that can indicate this difference, will be the next step. Lastly, an intramural VA classifier can be designed. This was mentioned in the introduction of the chapter as the ultimate goal of this intramural VA project. Learning a three-way classifier among epicardial, endocardial, and intramural VA ECGs, by combining all the work in this thesis, will be ideal future work.

| Control patients | CC with matching pace-map | CC with Combination of pace-maps | RMS with matching pace-map | RMS with Combination of pace-maps | Combination CC larger? | Combination RMS smaller? |
|---|---|---|---|---|---|---|
| 1 | 0.9021 | 0.8467 | 253.26 | 254.62 | no | no |
| 2 | 0.9722 | 0.9607 | 154.15 | 168.65 | no | no |
| 3 | 0.9298 | 0.8964 | 195.21 | 197.44 | no | no |
| 4 | 0.9165 | 0.9131 | 257.09 | 243.24 | no | yes |
| 5 | 0.9486 | 0.8410 | 193.82 | 205.75 | no | no |
| 6 | 0.8786 | 0.7779 | 219.49 | 256.46 | no | no |
| 7 | 0.8445 | 0.9539 | 259.22 | 210.38 | yes | yes |
| 8 | 0.8832 | 0.9226 | 221.12 | 183.94 | yes | yes |
| 9 | 0.9597 | 0.9788 | 218.46 | 225.46 | yes | no |
| 10 | 0.9522 | 0.9259 | 190.30 | 186.46 | no | yes |
| 11 | 0.9812 | 0.9436 | 178.06 | 182.49 | no | no |
| 12 | 0.8616 | 0.8211 | 219.63 | 211.65 | no | yes |
| 13 | 0.8769 | 0.8369 | 224.32 | 274.24 | no | no |
| 14 | 0.9510 | 0.8900 | 196.56 | 191.02 | no | yes |
| 15 | 0.9883 | 0.9193 | 138.01 | 192.08 | no | no |
| 16 | 0.9608 | 0.8674 | 196.60 | 250.70 | no | no |
| 17 | 0.9252 | 0.8735 | 169.29 | 199.59 | no | no |
| 18 | 0.9601 | 0.8703 | 156.95 | 204.25 | no | no |
| average | 0.9274 | 0.8911 | 214.05 | 221.11 | | |
| std. dev. | 0.0424 | 0.0523 | 58.14 | 50.17 | | |

| Intramural patients | CC with matching pace-map | CC with Combination of pace-maps | RMS with matching pace-map | RMS with Combination of pace-maps | Combination CC larger? | Combination RMS smaller? |
|---|---|---|---|---|---|---|
| 1 | 0.8482 | 0.9001 | 253.29 | 222.86 | yes | yes |
| 2 | 0.9366 | 0.9498 | 200.50 | 191.50 | yes | yes |
| 3 | 0.9375 | 0.9423 | 228.73 | 203.63 | yes | yes |
| 4 | 0.9237 | 0.9395 | 291.25 | 243.17 | yes | yes |
| 5 | 0.8095 | 0.8089 | 226.17 | 247.64 | no | no |
| 6 | 0.7618 | 0.7760 | 260.70 | 222.25 | yes | yes |
| 7 | 0.8648 | 0.8703 | 234.85 | 234.86 | yes | no |
| 8 | 0.9173 | 0.9308 | 240.83 | 238.76 | yes | yes |
| 9 | 0.8830 | 0.9137 | 214.22 | 196.51 | yes | yes |
| 10 | 0.8795 | 0.9407 | 186.26 | 193.04 | yes | no |
| 11 | 0.7760 | 0.8164 | 245.89 | 224.70 | yes | yes |
| 12 | 0.9057 | 0.9569 | 220.47 | 200.11 | yes | yes |
| 13 | 0.8601 | 0.9026 | 220.76 | 223.45 | yes | no |
| 14 | 0.9617 | 0.9755 | 192.56 | 182.21 | yes | yes |
| 15 | 0.8522 | 0.8698 | 264.38 | 228.45 | yes | yes |
| 16 | 0.6482 | 0.6351 | 306.47 | 312.14 | no | no |
| 17 | 0.8195 | 0.9052 | 246.25 | 189.85 | yes | yes |
| 18 | 0.5716 | 0.6224 | 342.06 | 338.72 | yes | yes |
| average | 0.8421 | 0.8698 | 255.09 | 239.35 | | |
| std. dev. | 0.0989 | 0.1002 | 58.42 | 62.54 | | |

Table 5.3: All 36 Patients' Results of Correlation Coefficient and Root Mean Square Error with Their Target PVC ECGs 

# CHAPTER VI

# Conclusion

## 6.1 Summary of the Thesis

This thesis is motivated by a problem from electrocardiology, identifying locations and classifying regional information of ventricular tachycardia and pace-map origins, which provides assistance to radiofrequency ablation treatments of ventricular arrhythmias. Feature selection and dimensionality reduction are applied to ECG signals to achieve an advancement in classification and estimation of VT origins. Processing and extracting the input ECG features and designing a model with the insight about the space where the desired information lie resulted in a good representation and an effective classification of ECG signals.

In Chapter II, two models, (1) an estimation function of three-dimensional coordinates from pace-map ECGs and (2) a classification of one-dimensional region categories from multi-dimensional ECG signals, are presented. By analyzing the signals with their known origins, we designed a new set of ECG features to use. We proved by the experiments that the binary classification of epicardial and endocardial ECGs can reach up to 80%.

Chapter III continues ECG analyses by applying neural networks, specifically restricted Boltzmann machine. The equivalence between GMM and Gaussian-softmax RBM is mathematically proven, and based on this proof, the distribution function

learned with GMM in Chapter II will be modeled with discriminative RBM. Although the epicardial and endocardial classification accruacy was not over 80%, we examined the learned weight matrices of discriminative RBMs and analyzed the characteristics of the pace-map ECGs.

Chapter IV presented Quaternion Laplacian Information Maps, a dimensionality reduction methodology with a specified, quaternion embedding space. By constraining the embedding space to a unit quaternion space, the embedding function and its optimization process had to be modified from the precedent method named Spherical Laplacian Information Maps. The quaternion embedding from QLIM provided better clusters and more information compared to that of spherical embedding from SLIM and open Euclidean embedding from other dimensionality reduction methods. The experiments with pace-map ECG signals clustered the data into their corresponding regional sites of the origins. Also, with the turntable image data, QLIM parameters were analyzed, and the rotational information that is contained in the images was observed.

Lastly in Chapter V, ventricular arrhythmias with intramural origins is introduced. In the previous chapters, VAs from epicardial and endocardial sites are presumed to have their origins on the surface of the heart. However, ventricular arrhythmias also can originate from the intramural myocardium. This chapter aims to demonstrated that intramural VA ECGs are different from non-intramural VA ECGs. First, the dimension reduced representations of ECGs from non-intramural and intramural patients presented different distributions and clusters between the two groups. Second, intramural VA ECGs had better affinity measures (higher CC and lower RMS) to the combination signals of two pace-maps nearby the PVC origins rather than to single pace-maps.

## 6.2 Summary of Future Research

The research in each chapter has future work to be continued, and it is presented at the end of each chapter. An organized summary of the future work is listed below.

**Expanding the scope of the thesis**

1. ECG classification of VA and pace-map origins including intramurals

    - The site of origin classification can be extended to a three-class problem including epicardial, endocardial, and intramural.

2. ECG classification of VT origins within different heart region categories

    - Left ventricle and right ventricle are categorized to 10 and 4 regions, respectively. A detailed classification problem can be designed, better with collecting more VT and pace-map ECGs.

3. Coordinate Estimation of VT origins

    - Knowing the location coordinate of the origins will answer all the classification problems. If the coordinate data can be provided, coordinate estimation is the ultimate objective to research. This will be approached in the universal heart model.

**Improving the work in this thesis**

1. Using the extensions of discriminative RBM for classification (Chapter III)

    - Hybrid discriminative RBM and Sparse RBM can be used for effective learning of the ECG dataset and efficient training of RBM.

2. Analyzing the convexity of QLIM optimization (Chapter IV)

    - The current QLIM optimization cannot be proved to be convex: only local extrema are guaranteed. A convexity analysis in the quaternion space will help analyze and design a robust QLIM optimization.

3. Characterize intramural VA ECGs for classification (Chapter V)

    - As Chapter V demonstrated that intramural VAs are different from non-intramurals, how they are different has to be studied.

- Larger number of intramural VAs from various groups of patient should be collected and researched.

4. Unsupervised learning of ECG feature with generative models

   - ECG feature learning is a generative training of low frequency time series data.
   - Deep learning using deep belief network or convolutional DBN is effective in feature learning if applicable.

# BIBLIOGRAPHY

# BIBLIOGRAPHY


[1] C. Murray and L. A.D., "Mortality by cause for eight regions of the world: Global burden of disease study," *The Lancet*, vol. 349, pp. 1269–1276, 1997.

[2] A. Jemal, E. Ward, Y. Hao, and M. Thun, "Trends in the leading causes of death in the united states, 1970-2002," *JAMA*, vol. 294, no. 10, pp. 1255–1259, 2005.

[3] C. Murray and L. A.D., "Alternative projections of mortality and disability by cause 19902020: Global burden of disease study," *The Lancet*, vol. 349, pp. 1498–1504, 1997.

[4] H. Wellens, F. Bar, and K. Lie, "The value of the electrocardiogram in the differential diagnosis of a tachycardia with a widened qrs complex," *The American Journal of Medicine*, vol. 64, pp. 27–33, 1977.

[5] E. B. Sgarbossa, S. L. Pinski, A. Barbagelata, D. A. Underwood, K. B. Gates, E. J. Topol, R. M. Califf, and G. S. Wagner, "Electrocardiographic diagnosis of evolving acute myocardial infarction in the presence of left bundle-branch block," *New England Journal of Medicine*, vol. 334, no. 8, pp. 481–487, 1996.

[6] C.-C. Chia and Z. Syed, "Scalable noise mining in long-term electrocardiographic time-series to predict death following heart attacks," in *Proceedings of the 20th ACM SIGKDD International Conference on Knowledge Discovery and Data Mining*, KDD '14, (New York, NY, USA), pp. 125–134, ACM, 2014.

[7] D. L. Kuchar, C. W. Thorburn, and N. L. Sammel, "Prediction of serious arrhythmic events after myocardial infarction: Signal-averaged electrocardiogram, holter monitoring and radionuclide ventriculography," *Journal of the American College of Cardiology*, vol. 9, pp. 531–538, 1987.

[8] J. S. Steinberg, A. Regan, R. R. Sciacca, J. B. Jr., and J. L. Fleiss, "Predicting arrhythmic events after acute myocardial infarction using the signal-averaged electrocardiogram," *The American Journal of Cardiology*, vol. 69, no. 1, pp. 13 – 21, 1992.

[9] C.-C. Chia, J. Blum, Z. Karam, S. Singh, and Z. Syed, "Predicting postoperative atrial fibrillation from independent ecg components," in *AAAI Conference on Artificial Intelligence*, 2014.

[10] M. Rivera-Ruiz, C. C., and V. J., "Einthoven's string galvanometer: The first electrocardiograph," *Texas Heart Institute Journal*, vol. 35, pp. 174–178, 2008.

[11] L. Biel, O. Pettersson, L. Philipson, and P. Wide, "Ecg analysis: a new approach in human identification," *Instrumentation and Measurement, IEEE Transactions on*, vol. 50, pp. 808–812, Jun 2001.

[12] R. M. John, U. B. Tedrow, B. A. Koplan, C. M. Albert, L. M. Epstein, M. O. Sweeney, A. L. Miller, G. F. Michaud, and W. G. Stevenson, "Ventricular arrhythmias and sudden cardiac death," *The Lancet*, vol. 380, no. 9852, pp. 1520 – 1529, 2012.

[13] H. L. Kennedy, J. A. Whitlock, M. K. Sprague, L. J. Kennedy, T. A. Buckingham, and R. J. Goldberg, "Long-term follow-up of asymptomatic healthy subjects with frequent and complex ventricular ectopy," *New England Journal of Medicine*, vol. 312, no. 4, pp. 193–197, 1985. PMID: 2578212.

[14] J. E. Poole, G. W. Johnson, A. S. Hellkamp, J. Anderson, D. J. Callans, M. H. Raitt, R. K. Reddy, F. E. Marchlinski, R. Yee, T. Guarnieri, M. Talajic, D. J. Wilber, D. P. Fishbein, D. L. Packer, D. B. Mark, K. L. Lee, and G. H. Bardy, "Prognostic importance of defibrillator shocks in patients with heart failure," *New England Journal of Medicine*, vol. 359, no. 10, pp. 1009–1017, 2008. PMID: 18768944.

[15] V. Y. Reddy, M. R. Reynolds, P. Neuzil, A. W. Richardson, M. Taborsky, K. Jongnarangsin, S. Kralovec, L. Sediva, J. N. Ruskin, and M. E. Josephson, "Prophylactic catheter ablation for the prevention of defibrillator therapy," *New England Journal of Medicine*, vol. 357, no. 26, pp. 2657–2665, 2007. PMID: 18160685.

[16] K.-H. Kuck, A. Schaumann, L. Eckardt, S. Willems, R. Ventura, E. Delacrtaz, H.-F. Pitschner, J. Kautzner, B. Schumacher, and P. S. Hansen, "Catheter ablation of stable ventricular tachycardia before defibrillator implantation in patients with coronary heart disease (vtach): a multicentre randomised controlled trial," *The Lancet*, vol. 375, no. 9708, pp. 31 – 40, 2010.

[17] M. Yokokawa, H. M. Kim, K. Baser, W. Stevenson, K. Nagashima, P. Della Bella, P. Vergara, G. Hindricks, A. Arya, K. Zeppenfeld, M. de Riva Silva, E. G. Daoud, S. Kumar, K.-H. Kuck, R. Tilz, S. Mathew, H. Ghanbari, R. Latchamsetty, F. Morady, and F. M. Bogun, "Predictive value of programmed ventricular stimulation after catheter ablation of post-infarction ventricular tachycardia," *Journal of the American College of Cardiology*, vol. 65, no. 18, pp. 1954–1959, 2015.

[18] F. Morady, M. Harvey, S. Kalbfleisch, R. el Atassi, H. Calkins, and J. Langberg, "Radiofrequency catheter ablation of ventricular tachycardia in patients with coronary artery disease," *Circulation*, vol. 87, no. 2, pp. 363–372, 1993.

[19] F. Bogun, R. El-Atassi, E. Daoud, K. C. Man, S. A. Strickberger, and F. Morady, "Radiofrequency ablation of idiopathic left anterior fascicular tachycardia," *Journal of Cardiovascular Electrophysiology*, vol. 6, no. 12, pp. 1113–1116, 1995.

[20] W. G. Stevenson and E. Delacretaz., "Radiofrequency catheter ablation of ventricular tachycardia," *Heart Rhythm*, vol. 84, no. 5, pp. 553–559, 2000.

[21] W. G. Stevenson and K. Soejima, "Catheter ablation of ventricular tachycardia," *Circulation*, vol. 115, pp. 2750–2760, 2007.

[22] T. Suzuki, Y. Nakamura, S. Yoshida, Y. Yoshida, K. Nakamura, T. Sasaki, M. Fujino, Y. Kawasaki, E. Ehara, Y. Murakami, and H. Shintaku, "Radiofrequency catheter ablation of idiopathic left anterior fascicular ventricular tachycardia in children," *Heart Rhythm*, vol. 11, no. 11, pp. 1948–1956, 2014.

[23] H. Blackburn, A. Keys, E. Simonson, P. Rautaharju, and S. Punsar, "The electrocardiogram in population studies: A classification system," *Circulation*, vol. 21, no. 6, pp. 1160–1175, 1960.

[24] H. Blackburn, "Electrocardiographic classification for population comparisons: The minnesota code," *Journal of Electrocardiology*, vol. 2, no. 1, pp. 5 – 9, 1969.

[25] J. R. Cox, F. M. Nolle, H. A. Fozzard, and G. C. Oliver, "Aztec, a preprocessing program for real-time ecg rhythm analysis," *Biomedical Engineering, IEEE Transactions on*, vol. BME-15, pp. 128–129, April 1968.

[26] K. Birman, "Rule-based learning for more accurate ecg analysis," *Pattern Analysis and Machine Intelligence, IEEE Transactions on*, vol. PAMI-4, pp. 369–380, July 1982.

[27] F. Gritzali, "Towards a generalized scheme for qrs detection in ecg waveforms," *Signal processing*, vol. 15, no. 2, pp. 183–192, 1988.

[28] Q. Zhao and L. Zhang, "Ecg feature extraction and classification using wavelet transform and support vector machines," in *Neural Networks and Brain, 2005. ICNN B '05. International Conference on*, vol. 2, pp. 1089–1092, Oct 2005.

[29] M. H. Song, J. Lee, S. P. Cho, K. J. Lee, and S. K. Yoo, "Support vector machine based arrhythmia classification using reduced features," *International Journal of Control Automation and Systems*, vol. 3, no. 4, p. 571, 2005.

[30] E. D. Übeyli, "Ecg beats classification using multiclass support vector machines with error correcting output codes," *Digital Signal Processing*, vol. 17, no. 3, pp. 675 – 684, 2007.

[31] R. Martis, C. Chakraborty, and A. Ray, "Wavelet-based machine learning techniques for ecg signal analysis," in *Machine Learning in Healthcare Informatics* (S. Dua, U. R. Acharya, and P. Dua, eds.), vol. 56 of *Intelligent Systems Reference Library*, pp. 25–45, Springer Berlin Heidelberg, 2014.

[32] L. Clemmensen, T. Hastie, D. Witten, and B. Ersbll, "Sparse discriminant analysis," *Technometrics*, vol. 53, no. 4, pp. 406–413, 2011.

[33] A. Banerjee, I. S. Dhillon, J. Ghosh, and S. Sra, "Clustering on the unit hypersphere using von mises-fisher distributions," *J. Mach. Learn. Res.*, vol. 6, pp. 1345–1382, Dec. 2005.

[34] S.-N. Yu and Y.-H. Chen, "Electrocardiogram beat classification based on wavelet transformation and probabilistic neural network," *Pattern Recognition Letters*, vol. 28, no. 10, pp. 1142 – 1150, 2007.

[35] P. Addison, J. Watson, G. Clegg, M. Holzer, F. Sterz, and C. Robertson, "Evaluating arrhythmias in ecg signal using wavelet transforms: Real-time analysis of the ventricular fibrillation wavefrom can reveal hidden structures," *IEEE Engineering in Medicine and Biology Magazine*, vol. 19, no. 5, pp. 104–109, 2000.

[36] E. Valles, V. Bazan, and F. Marchlinski, "Ecg criteria to identify epicardial ventricular tachycardia in nonischemic cardiomyopathy," in *Circulation: Arrhythmia Electrophysiology*, vol. 3, pp. 63–71, 2010.

[37] A. Berruezo, L. Mont, S. Nava, E. Chueca, E. Bartholomay, and J. Brugada, "Electrocardiographic recognition of the epicardial origin of ventricular tachycardias," in *Circulation*, vol. 109, pp. 1842–1847, 2004.

[38] C. Li, C. Zheng, and C. Tai, "Detection of ecg characteristic points using wavelet transforms," *Biomedical Engineering, IEEE Transactions on*, vol. 42, pp. 21–28, Jan 1995.

[39] J. Wiens and J. V. Guttag, "Active learning applied to patient-adaptive heartbeat classification," in *NIPS*, pp. 2442–2450, 2010.

[40] A. Al-Fahoum and I. Howitt, "Combined wavelet transformation and radial basis neural networks for classifying life-threatening cardiac arrhythmias," *Medical & Biological Engineering & Computing*, vol. 37, no. 5, pp. 566–573, 1999.

[41] M. Yokokawa, T.-Y. Liu, K. Yoshida, C. Scott, A. O. Hero, E. Good, F. Morady, and F. Bogun, "Automated analysis of the 12-lead electrocardiogram to identify the exit site of post-infarction ventricular tachycardia," *Heart Rhythm*, 2012.

[42] V. Bazan, E. P. Gerstenfeld, F. C. Garcia, R. Bala, N. Rivas, S. Dixit, E. Zado, D. J. Callans, and F. E. Marchlinski, "Site-specific twelve-lead ecg features to identify an epicardial origin for left ventricular tachycardia in the absence of myocardial infarction," *Heart Rhythm*, vol. 7, no. 4, pp. 1403–1410, 2007.

[43] D. Hummel, S. Strickberger, E. Daoud, M. Niebauer, O. Bakr, K. Man, B. Williamson, and F. Morady, "Results and efficency of programmed ventricular stimulation with four extrastimuli compared with one, two, and three extrastimuli," *Circulation*, vol. 90, pp. 2823–2827, 1994.

[44] F. Marchlinski, D. Callans, C. Gottlieb, and E. Zado, "Linear ablation lesions for control of unmappable ventricular tachycardia in patients with ischemic and nonischemic cardiomyopathy," *Circulation*, vol. 101, pp. 1288–1296, 2000.

[45] E. Sosa, M. Scanavacca, A. d'Avila, and F. Pilleggi, "A new technique to perform epicardial mapping in the electrophysiology laboratory," *Journal of Cardiovascular Electrophysiology*, vol. 7, no. 6, pp. 531–536, 1996.

[46] T. Hastie, A. Buja, and R. Tibshirani, "Penalized discriminant analysis," *Annals of Statistics*, vol. 23, pp. 73–102, 1995.

[47] E. Lehmann, *Testing Statistical Hypotheses*. Probability and Statistics Series, Wiley, 1986.

[48] J. Neyman and E. S. Pearson, "On the problem of the most efficient tests of statistical hypotheses," *Philosophical Transactions of the Royal Society of London. Series A, Containing Papers of a Mathematical or Physical Character*, vol. 231, pp. pp. 289–337, 1933.

[49] C. Cortes and V. Vapnik, "Support-vector networks," *Machine Learning*, vol. 20, no. 3, pp. 273–297, 1995.

[50] H. Byun and S.-W. Lee, "Applications of support vector machines for pattern recognition: A survey," in *Proceedings of the First International Workshop on Pattern Recognition with Support Vector Machines*, SVM '02, (London, UK, UK), pp. 213–236, Springer-Verlag, 2002.

[51] C.-C. Chang and C.-J. Lin, "LIBSVM: A library for support vector machines," *ACM Transactions on Intelligent Systems and Technology*, vol. 2, pp. 27:1–27:27, 2011. Software available at http://www.csie.ntu.edu.tw/ cjlin/libsvm.

[52] C. Bishop, *Neural Networks for Pattern Recognition*. Oxford University Press, USA, 1995.

[53] Y. Bengio, "Learning deep architectures for AI," *Foundations and Trends in Machine Learning*, vol. 2, no. 1, pp. 1–127, 2009. Also published as a book. Now Publishers, 2009.

[54] Y. Bengio, A. Courville, and P. Vincent, "Representation learning: A review and new perspectives," *IEEE Transactions on Pattern Analysis and Machine Intelligence*, vol. 35, no. 8, pp. 1798–1828, 2013.

[55] K. Kavukcuoglu, P. Sermanet, Y. Boureau, K. Gregor, M. Mathieu, and Y. LeCun, "Learning convolutional feature hierachies for visual recognition," in *NIPS*, 2010.

[56] K. Sohn, D. Y. Jung, and H. Lee, "Sparse, distributed, and convolutional training of image features for object recognition," in *unpublished manuscript*, 2011.

[57] G. E. Hinton, L. Deng, D. Yu, G. E. Dahl, A. rahman Mohamed, N. Jaitly, A. Senior, V. Vanhoucke, P. Nguyen, T. N. Sainath, and B. Kingsbury, "Deep neural networks for acoustic modeling in speech recognition: The shared views of four research groups," *IEEE Signal Process. Mag.*, vol. 29, no. 6, pp. 82–97, 2012.

[58] H. Lee, Y. Largman, P. Pham, and A. Y. Ng, "Unsupervised feature learning for audio classification using convolutional deep belief networks," in *Advances in Neural Information Processing Systems 22*, pp. 1096–1104, 2009.

[59] A. Mohamed, G. Dahl, and G. Hinton, "Acoustic modeling using deep belief networks," *Audio, Speech, and Language Processing, IEEE Transactions on*, vol. 20, no. 1, pp. 14 –22, 2012.

[60] A. Mohamed, G. E. Hinton, and G. Penn, "Understanding how deep belief networks perform acoustic modelling," in *ICASSP*, pp. 4273–4276, IEEE, 2012.

[61] H. Larochelle and Y. Bengio, "Classification using discriminative restricted boltzmann machines," in *Proceedings of the 25th International Conference on Machine Learning*, ICML '08, (New York, NY, USA), pp. 536–543, ACM, 2008.

[62] M. Ranzato, A. Krizhevsky, and G. E. Hinton, "Factored 3-way restricted Boltzmann machines for modeling natural images," in *International Conference on Artificial Intelligence and Statistics (AISTATS)*, 2010.

[63] C. Bishop, *Pattern recognition and machine learning*, vol. 4. Springer New York, 2006.

[64] N. Le Roux and Y. Bengio, "Representational power of restricted boltzmann machines and deep belief networks," *Neural Comput.*, vol. 20, pp. 1631–1649, June 2008.

[65] G. E. Hinton, *A Practical Guide to Training Restricted Boltzmann Machines*. 2012.

[66] J. B. Tenenbaum, V. de Silva, and J. C. Langford, "A global geometric framework for nonlinear dimensionality reduction," *Science*, vol. 290, pp. 2319–2323, 2000.

[67] M. Ranzato, Y. Boureau, and Y. LeCun, "Sparse feature learning for deep belief networks," *Advances in Neural Information Processing Systems*, 2007.

[68] A. Coates, H. Lee, and A. Y. Ng, "An analysis of single-layer networks in unsupervised feature learning," in *NIPS Workshop on Deep Learning and Unsupervised Feature Learning*, 2010.

[69] L. Cayton, "Algorithms for manifold learning," *Univ. of California at San Diego Tech. Rep*, pp. 1–17, 2005.

[70] L. van der Maaten, E. Postma, and H. van den Herik, "Dimensionality reduction: A comparative review," tech. rep., Tilburg University Technical Report, 2009.

[71] K. Carter, R. Raich, and A. O. Hero, "Spherical laplacian information maps (slim) for dimensionality reduction," in *IEEE Workshop on Statistical Signal Processing (SSAP)*, 2009.

[72] S. T. Roweis and L. K. Saul, "Nonlinear dimensionality reductin by locally linear embedding," *Science*, vol. 290, pp. 2323–2326, 2000.

[73] V. de Silva and J. Tenenbaum, "Global versus local methods for nonlinear dimensionality reduction," in *NIPS*, 2003.

[74] M. Belkin and P. Niyogi, "Laplacian eigenmaps and spectral techniques for embedding and clusturing," in *NIPS*, 2002.

[75] K. Carter, R. Raich, W. Finn, and A. O. Hero, "Fine: Fisher information nonparametric embedding," in *IEEE Transactions on Pattern Analysis and Machine Intelligence*, vol. 31, pp. 2093–2098, 2009.

[76] K. Carter, K.-M. Kim, R. Raich, and A. Hero, "Information preserving embeddings for discrimination," in *Proc. of IEEE Workshop on Digital Signal Processing*, 2009.

[77] J. Schmidt and H. Niemann, "Using quaternions for parametrizing 3-d rotations in unconstrained nonlinear optimization," in *Vision, Modeling, and Visualization*, 2001.

[78] W. Kaltenbrunner, R. Cardinal, M. Dubuc, M. Shenasa, R. Nadeau, G. Tremblay, M. Vermeulen, P. Savard, and P. L. Pag, "Epicardial and endocardial mapping of ventricular tachycardia in patients with myocardial infarction. is the origin of the tachycardia always subendocardially localized?," *Circulation*, vol. 84, no. 3, pp. 1058–71, 1991.

[79] M. Yokokawa, E. Good, A. Chugh, F. Pelosi, T. Crawford, K. Jongnarangsin, R. Latchamsetty, H. Oral, F. Morady, and F. Bogun, "Intramural idiopathic ventricular arrhythmias originating in the intraventricular septum: Mapping and ablation," *Circulation: Arrhythmia and Electrophysiology*, vol. 5, no. 2, pp. 258–263, 2012.

[80] B. Desjardins, M. Yokokawa, E. Good, T. Crawford, R. Latchamsetty, K. Jongnarangsin, H. Ghanbari, H. Oral, F. Pelosi, A. Chugh, F. Morady, and F. Bogun, "Characteristics of intramural scar in patients with nonischemic cardiomyopathy and relation to intramural ventricular arrhythmias," *Circulation: Arrhythmia and Electrophysiology*, vol. 6, no. 5, pp. 891–897, 2013.

[81] J. S. Koruth, S. Dukkipati, M. A. Miller, P. Neuzil, A. d'Avila, and V. Y. Reddy, "Bipolar irrigated radiofrequency ablation: A therapeutic option for refractory intramural atrial and ventricular tachycardia circuits," *Heart Rhythm*, vol. 9, no. 12, pp. 1932 – 1941, 2012.

[82] T. Yamada, W. R. Maddox, H. T. McElderry, H. Doppalapudi, V. J. Plumb, and G. N. Kay, "Radiofrequency catheter ablation of idiopathic ventricular arrhythmias originating from intramural foci in the left ventricular outflow tract: Efficacy of sequential versus simultaneous unipolar catheter ablation," *Circulation: Arrhythmia and Electrophysiology*, vol. 8, no. 2, pp. 344–352, 2015.